

**SYNTHESIS OF $(1-x)\text{BiFe}_{0.9}\text{La}_{0.1}\text{O}_3+x(\text{Ni}_{0.6}\text{Zn}_{0.4}\text{Fe}_{0.94}\text{V}_{0.06}\text{O}_4)$
NANOSTRUCTURED MULTIFERROIC COMPOSITES AND
STUDY OF ITS STRUCTURAL, MAGNETIC AND
ELECTRICAL PROPERTIES**

M.Sc. Thesis

BY

MD. RABIUL HASSAN



**DEPARTMENT OF PHYSICS
KHULNA UNIVERSITY OF ENGINEERING & TECHNOLOGY
KHULNA - 9203, BANGLADESH**

FEBRUARY- 2017

**SYNTHESIS OF $(1-x)\text{BiFe}_{0.9}\text{La}_{0.1}\text{O}_3+x(\text{Ni}_{0.6}\text{Zn}_{0.4}\text{Fe}_{0.94}\text{V}_{0.06}\text{O}_4)$
NANOSTRUCTURED MULTIFERROIC COMPOSITES AND
STUDY OF ITS STRUCTURAL, MAGNETIC AND
ELECTRICAL PROPERTIES**

BY

**MD. RABIUL HASSAN
ROLL NO: 155551
SESSION: JULY-2015**

A THESIS SUBMITTED TO THE DEPARTMENT OF PHYSICS,
KHULNA UNIVERSITY OF ENGINEERING & TECHNOLOGY,
KHULNA - 9203 IN PARTIAL FULFILMENT OF THE
REQUIRMENT FOR THE DEGREE OF MASTER OF SCIENCE



DEPARTMENT OF PHYSICS
KHULNA UNIVERSITY OF ENGINEERING & TECHNOLOGY
KHULNA - 9203, BANGLADESH

FEBRUARY- 2017

TO
MY PARENTS

DECLARATION

This is to certify that the thesis work entitled as “**Synthesis of (1-x) BiFe_{0.9}La_{0.1}O₃+ x(Ni_{0.6}Zn_{0.4}Fe_{0.94}V_{0.06}O₄) Nanostructured Multiferroic Composites and Study of its Structural, Magnetic and Electrical Properties**” has been carried out in partial fulfillment of the requirement for M.Sc. degree in the Department of Physics, Khulna University of Engineering & Technology, Khulna-9203, Bangladesh. The above research work or any part of this work has not been submitted to anywhere for the award of any degree or diploma. No other person’s work has been used without due acknowledgement.


1. Supervisor

Candidate

.....
Prof. Dr. Shibendra Shekher Sikder

.....
Md. Rabiul Hassan

2. Co-supervisor


.....
Dr. Mohammed Nazrul Islam Khan

Acknowledgements

I would like to express my deep sense of gratitude and high gratefulness with due respect to my Supervisor Professor Dr. Shibendra Shekher Sikder, Department of Physics, Khulna University of Engineering & Technology (KUET), Khulna for considering me as a thesis student. His guidance, enthusiastic concern, positive and regular inspiration and constructive supervision made the work easy and successful.

I am very much thankful to my Co-supervisor Dr. Mohammed Nazrul Islam Khan, Principal Scientific Officer (CSO), Materials Science Division, Atomic Energy Centre, Dhaka (AECD), who gave me the update and unique idea about this research. His valuable direction, suggestions and continuous assessment on work made me conscious and sincere to obtain better results in all experiments. Without his help and support it was quite difficult to do the research in laboratory.

I want to give my warm and deep gratitude to Dr. A. K. M. Abdul Hakim, Individual Consultant & Guest Faculty, Department of Glass & Ceramic Engineering (GCE), Bangladesh University of Engineering & Technology (BUET), who always think about research, new ideas and try to guide young researchers which made them passionate about research. This is my fortune to have the guidance from him which made my work more precise and prosperous. I understood the facts and mechanism behind multiferroics from him. He gave me the chance to use his laboratory to carry out several experiments and send my samples to Bose Institute-Kolkata for some measurements.

I gratefully acknowledge Professor Dr. Md. Mahbub Alam, Department of Physics, KUET, for his co-operation and inspiration during this work. I also grateful to Professor Dr. Md. Abdullah Elias Akhter, Department of Physics, KUET, who gave me financial support that helps me to when I was in Dhaka for laboratory work. He always liked to give me mental support that was so essential for me during the time of research.

I would also indebted to Mr. Abu Raihan Tarek, Chemistry Division, AECD, for supporting me to use his lab and guidance on synthesizing materials.

I gratefully acknowledge Professor Dr. Joly Sultana, Department of Physics, Khulna University of Engineering & Technology, for his co-operation and inspiration during this work. My thanks are also for Md. Kamrul Hasan Reza (Associate Professor), Mr. Sujit Kumar Shil, and Mr. Alamgir Hossain (Assistant Professor), Suman

Kumar Halder and Sumon Debnath (Lecturer), Department of Physics, KUET, for their moral support.

My thanks due to Dr. Dilip Kumar Saha, Director, AECD, for his kind permission to use the laboratory of Materials Science Division, AECD. My sincere thanks give to Dr. Sheikh Manjura Hoque, Head and CSO, Material Science Division, AECD, who provided valuable guidelines for my work and gave me permission to work in her division. I wish to thanks all the scientist of Materials Science Division, Dr. Md. Mahbulul Haque, Mr. Fazul Kamal, Mrs. Samia Islam Liba for their support and scientific discussion to do this research work.

I heartily express my gratitude to Mr. Saroar Hossain, PhD student, Bose Institute, Kolkata, India for his help in measuring XRD, rietveld refinement and Magnetization data. I also give my thanks to Mr. Abdullah Al Momin, PhD student, Department of Physics, BUET, for his help in measuring permeability and dielectric data. I acknowledge to Mr. Mehedi Hasan Rizvi, Assistant Professor, GCE-BUET for helping me to collect FESEM micrographs.

My special thanks to all the staff members of Materials Science Division and Chemistry Division, AECD, particularly Mrs. Alhamra Parveen, Mrs. Anjuman Ara Begum, Mr. Kamrul Islam, Mr. Anowar Hossain, Mr. Nurul Islam, Mrs. Nazmunnahar Begum, Mrs. Zarna Begum and Mr. Kaiyoum, Mr. Jahid, Mr. Ayub and Mr. Zahid for their sincere help during the preparation of the sample and experimental measurements.

I also thank all the office stuffs and laboratory assistants of the Department of Physics, AECD, who helped me at every respect to proceed the course work.

I would like to give thanks from deep of my heart to my parents and all others family members for their comprehensive mental support and love. I have not much word to express my gratefulness to them.

I also wish to thank to the authority of Khulna University of Engineering & Technology for providing me the necessary permission for conducting the thesis work.

Md. Rabiul Hassan

Abstract

The multiferroic composites $(1-x) \text{BiFe}_{0.9}\text{La}_{0.1}\text{O}_3 + x (\text{Ni}_{0.6}\text{Zn}_{0.4}\text{Fe}_{0.94}\text{V}_{0.06}\text{O}_4)$ are made with the combination of perovskite and ferrite materials. The nanoparticles are synthesized by using solid state reaction method and some mechanical dispersion techniques like magnetic stirring, ultrasonification and centrifugation. X-ray diffraction method with Rietveld refinement was established to see multiphase formation that consists with perovskite and ferrite compositions. From Rietveld analysis, rhombohedral to orthorhombic phase transition was found up to $x = 0.7$ and the pure cubic ferrite structure was found for $x = 1$ content. At $x = 0$, the sample is in rhombohedral and orthorhombic mixed phases but with the increasing in x (as ferrite content) the cubic phase was visible. At fully ferrite contents where $x = 1$, there has no rhombohedral and orthorhombic phase has been visible but only cubic phase is formed. The goodness of fitting confirmed that the composites are made with well distribution of perovskite and ferrite materials. The results from Rietveld analysis show that the increasing $\text{Ni}_{0.6}\text{Zn}_{0.4}\text{Fe}_{0.94}\text{V}_{0.06}\text{O}_4$ (NZVFO) contents the ferrite phase fraction was increased whereas the perovskite phase fraction decreased. The Field emission scanning electron microscopy (FESEM) has been used to understand the surface morphology of composites. The proportion and contribution of particles inside the composites have been found by EDX analysis. Initially, all prepared samples were heated at 150°C and the nanostructure was confirmed by FESEM photograph where the size of particles were about $20 \sim 30$ nm and after increasing annealing temperature, increase in grain size is clearly observed. At 300°C , 450°C , 600°C and 850°C annealing temperatures the grain sizes are in between $30 \sim 40$ nm, $50 \sim 80$ nm, $160 \sim 260$ nm and $800 \sim 1700$ nm respectively. The magnetization, saturation magnetization and coercivity has calculated by using Vibration sample magnetometer (VSM), where magnetization is lowest for pure $\text{BiFe}_{0.9}\text{La}_{0.1}\text{O}_3$ (BLFO) perovskite phase and increased with increasing NZVFO ferrite contents. The magnetization is maximum for $x = 1$ which may be contributed by total of ferrimagnetic contents. The temperature dependent magnetization was taken at 50e constant field for both of heating and cooling mechanism where the Curie temperatures have Curie temperatures are 364°C and 350°C for pure perovskite mixed phases ($x = 0$) and cubic ferrite phase ($x = 1$) respectively. The frequency dependent dielectric constant is maximum for Bismuth perovskite content but it was lower as ferrite contents increased. On the other hand resistivity increased with increasing ferrite content. Frequency dependent permeability was maximum for pure NZVFO content but in BLFO content, permeability became low.

CONTENTS

	Page No.
Title Page	
Declaration Page	i
Acknowledgement	ii
Abstract	iv
Contents	v
List of Figures	ix
List of Tables	xiii
List of Symbols	xiv

CHAPTER-I

INTRODUCTION

1.1	Introduction	1
1.2	Motivations	4
1.3	The Aims and Objectives of the Present Work	5
1.4	Reason for Choosing this Research Work	6
1.5	Background of Material Selection: Literature Review	7
1.6	Outline of the Thesis	10

CHAPTER-II

THEROETICAL BACKGROUND

2.1	Overview of Multiferroic	12
2.1.1	Single Phase Multiferroic	14
2.1.2	Multiferroic in Composites	15
2.1.3	Bulk ME Composites	16
2.1.4	Composites in Ceramic	16
2.1.5	Nano Structured Multiferroics	17
2.2	Perovskite Structure	18
2.2.1	Phase Transition in Perovskite BiFeO_3 single crystals	21
2.2.2	The Phase Diagram of BiFeO_3	22

2.3	Ferroelectricity and Ferromagnetism inside Multiferroic Materials	23
2.3.1	Ferroics	23
2.3.2	Ferroelectricity	26
2.4	Spinel Structure of Ferrite	29
2.4.1	Tetrahedral Site	30
2.4.2	Octahedral Site	31
2.5	Magnetism	32
2.5.1	Ferromagnetism	32
2.5.2	Antiferromagnetism	34
2.6	Multiferroicity	35

CHAPTER-III

EXPERIMENTAL PROCEDURE

3.1	Methodology of Nanostructured Multiferroic Composites	38
	Preparation	
3.1.1	Aspects of Present Work	38
3.1.2	Problems with conventional Methods	39
3.1.3	Reason of using oxide materials	39
3.1.4	Selection of Raw Materials	39
3.1.5	Weighing the raw materials at precise ratio	40
3.2.	Mixed and milled the samples (Hand Milling)	40
3.2.1	Stirred the samples in magnetic stirring hot pot	41
3.2.2	Further dispersion was made by using Ultrasonification	43
3.2.3	Centrifugation	43
3.2.4	Heat Treatment	45
3.3	Converting the ferrites into powder and pressing the powder	46
3.3.1	Grinding	46
3.3.2	Pressing or Extrusion	46
3.4	Annealing	47
3.5	Sintering	48
3.6	X-ray Diffraction (XRD)	50
3.6.1	Derivation of Bragg's Law	51
3.6.2	Different Parts of the PHILIPS X' Pert PRO XRD System	52

3.6.3	Interpretation of the XRD data	52
3.6.4	X-ray Density and Bulk Density	53
3.6.5	Porosity	54
3.6.6	Crystalline Size	54
3.6.7	Rietveld Refinement	55
3.7	Field Emission Scanning electron microscopy (FESEM)	56
3.8	Vibrating Sample Magnetometer (VSM)	56
3.9	Electrical and Dielectric Measuring Systems	57
3.9.1	DC and AC Resistivity Measurement	58
3.9.2	Dielectric Properties Measuring System	60
3.9.3	Impedance Analyzer	62
3.10	Theories of Permeability	63

CHAPTER-IV

RESULTS AND DISCUSSION

4.1	X-ray Diffraction Analysis	65
4.1.1	The Pure $R3c$ Phase	65
4.1.2	The Distorted Orthorhombic Phase	66
4.1.3	The Pure Cubic Phase	66
4.1.4	Domination of NZVF on BLFO Phase	67
4.1.5	Rietveld Refinement of $(1-x) \text{BiFe}_{0.9}\text{La}_{0.1}\text{O}_3 + x\text{Ni}_{0.6}\text{Zn}_{0.4}\text{Fe}_{0.94}\text{V}_{0.06}\text{O}_4$	68
4.2	Microstructure and morphology studies	74
4.2.1	Confirmation of Nano Structure	74
4.2.2	Study of Microstructure and Morphology with the variation of Annealing Temperature	76
4.3	Measurement of Magnetization	83
4.3.1	Measurement of Ferromagnetic Effect on Multiferroic Magnetization $(1-x) \text{BiFe}_{0.9}\text{La}_{0.1}\text{O}_3 + x\text{Ni}_{0.6}\text{Zn}_{0.4}\text{Fe}_{0.94}\text{V}_{0.06}\text{O}_4$ Composites	83
4.3.2	Temperature Dependence Magnetization	88
4.4	Study the frequency dependent of Permeability, Complex	89

	permeability and loss tangent	
4.5	Measurement of Ferroelectric Properties of Multiferroic Composites	92
	CHAPTER-V	
	CONCLUSIONS	
5.1	Conclusions	101
5.2	Scope of future work	
	References	

List of Figures		Page No.
Figure 2.1	Hysteresis loops of (a) ferromagnetic, (b) ferroelectric and (c) ferroelastic materials.	14
Figure 2.2	(a) Cubic perovskite unit cell, (b) Pnma-orthorhombic perovskite unit cell, (c) R3c-rhombohedral perovskite unit cell and (d) P6 ₃ cm hexagonal perovskite unit cell. Blue spheres represent the A cations, yellow spheres represent the B cations, and red spheres represent oxygen anions forming an octahedra.	19
Figure 2.3	Perovskite distortion from (a) cubic to (b) orthorhombic	21
Figure 2.4	Crystallographic (a) and magnetic (b) structure of BiFeO ₃	21
Figure 2.5	Phase diagram of BiFeO ₃ where the relevant composition is illustrated.	22
Figure 2.6	(a) Gibbs free energy and (b) resulting hysteresis of the order parameter $\eta \in \{M, P, \varepsilon\}$ depending on the external field $\xi \in \{H, E, \sigma\}$	25
Figure 2.7	Schematic view of ferroelectricity where non volatile & reversible polar state is illustrated	26
Figure 2.8	Schematic view of the perovskite oxide structure	27
Figure 2.9	In BiFeO ₃ the ordering of lone pairs (yellow "lobes") of Bi ³⁺ ions (orange), contributes to the polarization (green arrow)	27
Figure 2.10	Schematic drawing of the crystal structure of perovskite BiFeO ₃ (space group: R3c). Two crystals along [111] direction are shown in the figure.	28
Figure 2.11	Characteristic double-well potential energy as a function of the position of the B cation between the oxygen anions in perovskite ferroelectrics	28
Figure 2.12	Schematic of partial unit cell	30
Figure 2.13	Magnetic hysteresis loop	33
Figure 2.14	Variation of magnetic object due to different temperature	34
Figure 2.15	The 'world of electrically and magnetically polarizable materials' including bare ferroics, multiferroics and linear magnetoelectrics, as well as dipole-, spin- and non-linear ME multiglasses	35

Figure 3.1	Magnetic stirring with hot pot and beaker and magnetic bars in different size	42
Figure 3.2	Ultrasonic cleaner showing the removable basket in place, and a close up of the light and timer	43
Figure 3.3	Centrifuge used in lab with four chambers	45
Figure 3.4	Hydraulic press used to make different shaped samples.	47
Figure 3.5	Toroid and disk shape sample.	47
Figure 3.6	Flow chart of the sample preparation	49
Figure 3.7	Incident rays (1 and 2) at angle θ on the planes of atoms in a crystal. Rays reinforce if their difference in path length ($AB + BC$) is an integer times the wavelength of the X ray.	50
Figure 3.8	Crystal plane orientation	51
Figure 3.9	Internal arrangement of a PHILIPS X' Pert PRO X-ray diffractometer	52
Figure 3.10	Field Emission Scanning Electron Microscope (FESEM)	56
Figure 3.11	Vibrating Sample Magnetometer	57
Figure 3.12	Flow sheet diagram of the two-probe resistivity apparatus	58
Figure 3.12	Schematic diagram of an LCR meter [3.23].	61
Figure 3.13	The real and imaginary part of impedance with resistance variance	63
Figure 4.1	BLFO XRD pattern where enlarged scale shows the merging of two indexed peaks in a single peak.	66
Figure 4.2	X-ray diffraction pattern of $(1-x) \text{BiFe}_{0.9}\text{La}_{0.1}\text{O}_3 + x\text{Ni}_{0.6}\text{Zn}_{0.4}\text{Fe}_{0.94}\text{V}_{0.06}\text{O}_4$ multiferroic composites with x variation at 850°C annealing temperature	67
Figure 4.3	Broadening of peaks of XRD pattern of $(1-x) \text{BiFe}_{0.9}\text{La}_{0.1}\text{O}_3 + x\text{Ni}_{0.6}\text{Zn}_{0.4}\text{Fe}_{0.94}\text{V}_{0.06}\text{O}_4$	68
Figure 4.4	Representation of XRD data with Rietvelt Refinement. The red circle, black line, blue and light sky blue line represents the value for observed, calculated data and peaks respectively of $(1-x) \text{BiFe}_{0.9}\text{La}_{0.1}\text{O}_3 + x\text{Ni}_{0.6}\text{Zn}_{0.4}\text{Fe}_{0.94}\text{V}_{0.06}\text{O}_4$	69

Figure 4.5	Phase fraction for $x=0, 0.1, 0.2, 0.3, 0.5, 0.7, 1$ of $(1-x) \text{BiFe}_{0.9} \text{La}_{0.1} \text{O}_3 + x \text{Ni}_{0.6} \text{Zn}_{0.4} \text{Fe}_{0.94} \text{V}_{0.06} \text{O}_4$	70
Figure 4.6	FESEM micrographs and EDX spectra of $(1-x)(\text{BiFe}_{0.9} \text{La}_{0.1} \text{O}_3) + x(\text{Ni}_{0.6} \text{Zn}_{0.4} \text{Fe}_{0.94} \text{V}_{0.06} \text{O}_4)$	75
Figure 4.7	FESEM micrographs of $(1-x) \text{BiFe}_{0.9} \text{La}_{0.1} \text{O}_3 + x \text{Ni}_{0.6} \text{Zn}_{0.4} \text{Fe}_{0.94} \text{V}_{0.06} \text{O}_4$ for $x = 0, 0.2, 0.5, 0.7$ and at 300°C annealing temperature	78
Figure 4.8	FESEM micrographs of $(1-x) \text{BiFe}_{0.9} \text{La}_{0.1} \text{O}_3 + x \text{Ni}_{0.6} \text{Zn}_{0.4} \text{Fe}_{0.94} \text{V}_{0.06} \text{O}_4$ for $x = 0, 0.2, 0.5, 0.7$ and at 450°C annealing temperature	79
Figure 4.9	FESEM micrographs of $(1-x) \text{BiFe}_{0.9} \text{La}_{0.1} \text{O}_3 + x \text{Ni}_{0.6} \text{Zn}_{0.4} \text{Fe}_{0.94} \text{V}_{0.06} \text{O}_4$ for $x = 0, 0.2, 0.5, 0.7$ and at 600°C annealing temperature	80
Figure 4.10	FESEM micrographs of $(1-x) \text{BiFe}_{0.9} \text{La}_{0.1} \text{O}_3 + x \text{Ni}_{0.6} \text{Zn}_{0.4} \text{Fe}_{0.94} \text{V}_{0.06} \text{O}_4$ for $x = 0, 0.2, 0.5, 0.7$ and at 850°C annealing temperature	81
Figure 4.11	:Magnetization M-H curve of $(1-x) \text{BiFe}_{0.9} \text{La}_{0.1} \text{O}_3 + x \text{Ni}_{0.6} \text{Zn}_{0.4} \text{Fe}_{0.94} \text{V}_{0.06} \text{O}_4$ at 850°C sintering temperature	84
Figure 4.12	Broadening of Magnetization M-H curve of $(1-x) \text{BiFe}_{0.9} \text{La}_{0.1} \text{O}_3 + x \text{Ni}_{0.6} \text{Zn}_{0.4} \text{Fe}_{0.94} \text{V}_{0.06} \text{O}_4$ for $x = 0, 0.2, 0.3, 0.5, 0.7, 1$ at 850°C sintering temperature	85
Figure 4.13	Relation between saturation magnetization and coercivity of $(1-x) \text{BiFe}_{0.9} \text{La}_{0.1} \text{O}_3 + x \text{Ni}_{0.6} \text{Zn}_{0.4} \text{Fe}_{0.94} \text{V}_{0.06} \text{O}_4$ for $x = 0, 0.1, 0.2, 0.3, 0.5, 0.7, 1$ at 850°C sintering temperature	87
Figure 4.14	Anisotropy constant of $(1-x) \text{BiFe}_{0.9} \text{La}_{0.1} \text{O}_3 + x \text{Ni}_{0.6} \text{Zn}_{0.4} \text{Fe}_{0.94} \text{V}_{0.06} \text{O}_4$ for $x = 0, 0.1, 0.2, 0.3, 0.5, 0.7, 1$ at 850°C sintering temperature	87
Figure 4.15	Temperature dependent magnetization of $(1-x) \text{BiFe}_{0.9} \text{La}_{0.1} \text{O}_3 + x \text{Ni}_{0.6} \text{Zn}_{0.4} \text{Fe}_{0.94} \text{V}_{0.06} \text{O}_4$ for $x = 0$, and 1	88
Figure 4.16	:Frequency dependent real part of permeability of $(1-x) \text{BiFe}_{0.9} \text{La}_{0.1} \text{O}_3 + x \text{Ni}_{0.6} \text{Zn}_{0.4} \text{Fe}_{0.94} \text{V}_{0.06} \text{O}_4$, where $x = 0, 0.1, 0.2, 0.3, 0.5, 0.7, 1$ at 850°C sintering temperature	89

Figure 4.17	Frequency dependent Imaginary Part of Permeability of (1-x) $\text{BiFe}_{0.9}\text{La}_{0.1}\text{O}_3 + x\text{Ni}_{0.6}\text{Zn}_{0.4}\text{Fe}_{0.94}\text{V}_{0.06}\text{O}_4$, where x = 0, 0.1 0.2, 0.3, 0.5, 0.7, 1 at 850°C sintering temperature	90
Figure 4.18	Frequency dependent Loss tangent of (1-x) $\text{BiFe}_{0.9}\text{La}_{0.1}\text{O}_3 + x\text{Ni}_{0.6}\text{Zn}_{0.4}\text{Fe}_{0.94}\text{V}_{0.06}\text{O}_4$, where x = 0, 0.1 0.2, 0.3, 0.5, 0.7, 1 at 850°C sintering temperature	91
Figure 4.19	Frequency dependent Loss tangent of (1-x) $\text{BiFe}_{0.9}\text{La}_{0.1}\text{O}_3 + x\text{Ni}_{0.6}\text{Zn}_{0.4}\text{Fe}_{0.94}\text{V}_{0.06}\text{O}_4$, where x = 0, 0.1 0.2, 0.3, 0.5, 0.7, 1 at 850°C sintering temperature	92
Figure 4.20	Frequency dependent Dielectric Constant of (1-x) $\text{BiFe}_{0.9}\text{La}_{0.1}\text{O}_3 + x\text{Ni}_{0.6}\text{Zn}_{0.4}\text{Fe}_{0.94}\text{V}_{0.06}\text{O}_4$, where x = 0, 0.1 0.2, 0.3, 0.5, 0.7, 1 at 850°C sintering temperature	95
Figure 4.21	Frequency dependent Imaginary Part of Dielectric Constant of (1-x) $\text{BiFe}_{0.9}\text{La}_{0.1}\text{O}_3 + x\text{Ni}_{0.6}\text{Zn}_{0.4}\text{Fe}_{0.94}\text{V}_{0.06}\text{O}_4$, where x = 0, 0.1 0.2, 0.3, 0.5, 0.7, 1 at 850°C sintering temperature	96
Figure 4.22	Frequency dependent Di-electric Loss tangent of (1-x) $\text{BiFe}_{0.9}\text{La}_{0.1}\text{O}_3 + x\text{Ni}_{0.6}\text{Zn}_{0.4}\text{Fe}_{0.94}\text{V}_{0.06}\text{O}_4$, where x = 0, 0.1 0.2, 0.3, 0.5, 0.7, 1 at 850°C sintering temperature	97
Figure 4.23	Frequency dependent specific resistivity of (1-x) $\text{BiFe}_{0.9}\text{La}_{0.1}\text{O}_3 + x\text{Ni}_{0.6}\text{Zn}_{0.4}\text{Fe}_{0.94}\text{V}_{0.06}\text{O}_4$, where x = 0, 0.1 0.2, 0.3, 0.5, 0.7, 1 at 850°C sintering temperature	98
Figure 4.24	Comparison between Dielectric constant and Permeability of (1-x) $\text{BiFe}_{0.9}\text{La}_{0.1}\text{O}_3 + x\text{Ni}_{0.6}\text{Zn}_{0.4}\text{Fe}_{0.94}\text{V}_{0.06}\text{O}_4$, where x = 0, 0.1 0.2, 0.3, 0.5, 0.7, 1 at 850°C sintering temperature	99
Figure 4.25	Comparison between Dielectric loss tangent and Magnetic loss tangent of (1-x) $\text{BiFe}_{0.9}\text{La}_{0.1}\text{O}_3 + x\text{Ni}_{0.6}\text{Zn}_{0.4}\text{Fe}_{0.94}\text{V}_{0.06}\text{O}_4$, where x = 0, 0.1 0.2, 0.3, 0.5, 0.7, 1 at 850°C sintering temperature	100

List of Tables		Page No
Table 2.1	Site preference of perovskite structured materials	18
Table 2.2	Atomistic positions in cubic, orthorhombic (Pnma) and rhombohedral (R3c) perovskites	20
Table 2.3	Analogies between different ferroic materials	25
Table 2.4	Metal ion arrangements in spinel ferrite unit cell with composition (MO.Fe ₂ O ₃)	31
Table: 2.5	Site preferences of metallic ions	32
Table-2.6	Similarities and dissimilarities between two types of Multiferroics	37
Table 3.1	Detail calculation of materials used in this research	41
Table 4.1 (a-b)	Rietveld refined structural parameters obtained from XRD with χ^2 (Goodness of fit), R_p (residuals for the unweighed pattern) and R_{wp} (residuals for the weighed pattern) of the compositions	71
Table 4.2	Rietveld refined structural parameters and phases fractions (wt%) obtained from XRD with R_{Bragg} (Bragg factor), χ^2 (Goodness of fit), R_f (structure factor), R_p (residuals for the unweighed pattern) and R_{wp} (residuals for the weighed pattern) of the compositions: (1-x)(BiFe _{0.9} La _{0.1} O ₃) + x(Ni _{0.6} Zn _{0.4} Fe _{0.94} V _{0.06} O ₄)	73
Table 4.3	Shannon ionic radius for the elements used in this research	77
Table 4.4	Grain size from FESEM micrographs with different annealing temperature of (1-x) BiFe _{0.9} La _{0.1} O ₃ + xNi _{0.6} Zn _{0.4} Fe _{0.94} V _{0.06} O ₄ for x=0, 0.2, 0.5, 0.7	82
Table 4.5	Saturation Magnetization and coercivity of (1-x) BiFe _{0.9} La _{0.1} O ₃ + xNi _{0.6} Zn _{0.4} Fe _{0.94} V _{0.06} O ₄ for x = 0, 0.2, 0.3, 0.5, 0.7, 1 at 850°C sintering temperature	86
Table 4.6	The comparison between Permeability, Magnetic Loss Tangent, Dielectric Constant, Dielectric Constant, Resistivity, Dielectric Loss Tangent of (1-x) BiFe _{0.9} La _{0.1} O ₃ + xNi _{0.6} Zn _{0.4} Fe _{0.94} V _{0.06} O ₄ , where x = 0, 0.1 0.2, 0.3, 0.5, 0.7, 1 at 850°C sintering temperature	99

List of Symbols

XRD	=	X-Ray Diffraction
VSM	=	Vibrating Sample Magnetometer
FESEM	=	Field Emission Scanning Electron Microscopy
BLFO	=	$\text{BiFe}_{0.9}\text{La}_{0.1}\text{O}_3$
NZVFO	=	$\text{Ni}_{0.6}\text{Zn}_{0.4}\text{Fe}_{0.94}\text{V}_{0.06}\text{O}_4$
T_m	=	Melting temperature
K_1	=	Anisotropy constant
H_c	=	Coercive force
μ	=	Permeability
μ_m	=	Maximum permeability
μ_i	=	Initial permeability
μ'	=	Real part of the complex permeability
μ''	=	imaginary part of the complex permeability
D_g	=	Grain size
B	=	Magnetic induction
H	=	Magnetic field
a_0	=	Lattice parameter
$\tan \delta$	=	loss factor or loss tangent.
M_s	=	Saturation magnetization
T_c	=	Curie temperature
λ	=	Wave length of the X-ray
[hkl]	=	Index of the peak
I	=	X-ray beam of intensity
M	=	Magnetization
R_{wp}	=	Discrepancy factor
R_{exp}	=	Expected value
χ^2	=	Goodness of fit index

CHAPTER I

INTRODUCTION

CHAPTER II

THEORETICAL BACKGROUND

CHAPTER III

EXPERIMENTAL PROCEDURE

CHAPTER IV

RESULTS AND DISCUSSION

CHAPTER V

CONCLUSIONS

REFERENCES

INTRODUCTION

1.1 Introduction

Human always liked to find and understand new materials from their huge interest on living sustainable life. To discover and generate new materials is one of great activity of human being from ancient era. Materials development is an art which contributes human development from the beginning of human settlement. Design of new material is not easy task for that reason every stage of civilization costs many times to jump another stage. But interestingly the revolution had begun from eighteen century when people were starting to understand materials from its atomic level. Semiconductor based transistor has played an important role in inventing many other electronics content which also made our life easy. From all electronics devices computer, laptop, mobile phone are most popular for its high accessibility and easy performance. Many complex calculations and tough functions which are not possible to solve by human, computer can do it. Internet based communication system made the planet more accessible and consumed time.

Other hand mobile phone is an incredible device that made fast and straightforward communications with user friendly operation mechanism. The data are represented by bits where '0' and '1' based binary number is one and only system to produce input signals readable to computer. The magnetization spin is required to produce '0' and '1' based binary system. So materials can dominate the production of '0' and '1' inside computer. This is important to know that how fast a material can convert '0' to '1' by altering the magnetization field with significant saturation magnetization (M_s). To enable spontaneous conversion from '0' to '1' and '1' to '0' it is required to frequent change in magnetization with changing electric field. For this reason electric field should be used to tune magnetic field or magnetic field may have the ability to dominate electric property. But fact is that, many materials have not the ability which can simultaneously generate electric and magnetic field. Multiferroic material is a term in solving such problems where we need both ferroelectric and ferromagnetic properties.

The most important advances were made in ferromagnetism in the field of magnetic oxide. They have wide range of technological application in transformer cores, inductors, high quality filters, radio frequency circuits, rod antenna, read/write heads for high-speed digital tape and operating devices [1.1 – 1.3]. Among the soft ferrites Ni-Cu-Zn, Mg-Cu-Zn, Ni-Zn and Mn-Zn ferrites with various additives have enormous technological applications and accordingly extensive research work have been carried out [1.4 - 1.8]. In the recent years, the multiferroic composite materials have attracted a significant interest all over the world from the technological as well as academics point of view [1.9]. These materials are useful as magnetic field sensors (ac and dc field measurement), actuators, transducers, phase shifter, filters and memory devices. Multiferroic material has ferroelectric, ferromagnetic and ferroelastic properties [1.10] which resulted high potential applications in novel devices design as well as attractive basic studies of Physics [1.11]. Multiferroic compounds are mostly used to demonstrate spintronics devices [1.12]. In nature few materials exit multiferroic properties at room temperature. At higher than Curie temperature most materials have lose their ferromagnetic properties. So temperature controlled device design is one of the major challenge in materials research. In spintronics devices multiferroic materials have wide range of applications in modern electronics for their successive phenomena both in electric and magnetic purposes.

In future mobile phone will take place instead of computer. In electronics devices memory is very important issue to store data where easy memory access and random data transfer are required. People want to store more data on memory devices and like to transfer it at a high rate in a short time thus the devise may not collapse. The requirement of storing many data increased day by day for that reason we are using large capacity memory devices. Both computer and mobile phone are required memory devices to store data. Moreover computer or mobile phones are now not only used for the purpose of calculation and communication but also many functions of entertainment have been done by these devices. As a result the memory devices like RAM, ROM and hard disc are heavier from the sense of storing data than previous days. So the question is that how fast the computer or mobile phone can store and access the data! The future improvement of computational based information technology had predicted by legendary Moore's law which states that the performance of computers will double every other years [1.13 - 1.14].

The conventional memory devices are not able to solve the facts we are facing now with memory devices like slow rate of transfer data, make slower the devices when store more data and make hot the devices on operations. In conventional devices the charge degrees of freedom is not handled whereas in spintronics devices electron spin can take the degree of freedom in association with coupling electronics and magnetic properties [1.15]. In the core of computer based information technology the materials is very important. Without selecting and synthesizing proper materials there has no value of improving software. The materials behind designing computer devices should be more high permeable, having giant resistivity and high di-electric properties, random access on saturating magnetization etc.

Multiferroic exhibits several kinds of long range magnetic ordering, spontaneous electric polarization, and ferroelasticity [1.16]. Bismuth Ferrite (BiFeO_3) is one of the popular materials in the sense of having significance multiferroic properties. Both its antiferromagnetic and ferroelectric transition temperatures (643 K and 1100 K, respectively) are well above room temperature [1.17]. The morphological investigation shows that the composite prefers hexagonal structure. The morphology of the formation of composite has seen through SEM technique. The magnetic behavior of the composites at room temperature display magnetic hysteresis loop indicates that the composite are ferromagnetic [1.18]. The dielectric and magnetic properties of ferroelectric - antiferroelectric $\text{BaTiO}_3 - \text{LaMnO}_3$ composite with sintering temperature, i.e. 1150°C , the Ba ion in BaTiO_3 seems to diffuse into LaMnO_3 ; resulting in $\text{BaTiO}_3 - (\text{La}, \text{Ba})\text{MnO}_3$ ferroelectric – ferromagnetic composite [1.19]. To develop functional multiferroics materials many scientists examined physical properties of BiFeO_3 with different concentration of Lanthanum substitution which shows consequence change in structural, magnetic and electrical properties. Study of the sample has been made with 10% substitution of Lanthanum ion on B site of Bismuth ferrite for its optimum properties in many earlier works [1.20 – 1.21] where the structural, magnetic and dielectric properties of BiFeO_3 have been vigorously changed after substituting 10% La [1.22].

In this Study the composite of multiferroic will be synthesized to examine physical, magnetic, electrical and structural properties. The designed materials will have the form of $(1-x)\text{BiFe}_{0.9}\text{La}_{0.1}\text{O}_3+x(\text{Ni}_{0.6}\text{Zn}_{0.4}\text{Fe}_{0.94}\text{V}_{0.06}\text{O}_4)$ to produce multiferroic composite. Ni-Zn ferrite is mostly used in technology as soft ferrites from audio frequencies to several hundred megahertz. In this study Ni-Zn-V ferrite will be

designed with 60%Ni, 40%Zn, 94%Fe and 6%V substitution on B-site as its convenient previous results in several works. Both of the samples are just taken into account with their optimum value in which they show particular change in basic properties. The samples will prepare separately by chemical co-precipitation method for the purpose of obtaining nanocrystalline powdered structure which will confirm by X-ray diffraction (XRD) analysis and Field Emission Scanning Electron Microscopy (FESEM) graph. Heat treatment above sintering temperature may cause to melt the sample which is responsible to change in individual properties of the samples attained in the composition. Finally structural, electrical transport and magnetic properties will be studied all the prepared samples.

1.2 Motivations

Due to the expensive of synthesis nanomaterials and higher cost of raw materials which are usually used in synthesizing nano particles, the research of multiferroics is not popular in Bangladesh. Bangladesh is now better in software development but the matter of sadness is that the research on improving electronics devices like memory devices, microprocessors, inductors, transducers etc are not appreciated from the point of research interest. As a result the creation of actual Digital Bangladesh will not possible due the lacing of contribution on hardware development and it will be quite tough to achieve the goal belongs Digital Bangladesh. To emphasize the research activities on multiferroics will be a matter of progress both in economy and sustainability if we able to improve the research quality as well as the industrial application. The research activities should be focused on developing low cost electronics devices which also results low energy consumption. In our country the energy is one of major problem and most of villagers are not living with electricity due to the lack of production. Solar panel will be a solution but before that low energy consumed electronic devices must be designed. Otherwise the blessings of electricity may not be effective for the people. Moreover, from global perspective energy is also a problem of today which decline the progress of future if research will fail to give proper solution. From this inspiration researchers and politicians are confident to fabricate low energy cost materials which will be applicable in different electronics content.

Multiferroic composites would be considered as a parameter to solve such problems in which we are trying to minimize the amount of required energy. As

discussed in earlier, multiferroic material with heterostructure has the ability to minimize energy consumption due to strong ME effect. Other hand the multiferroic materials also have spintronics application which may affect the spontaneous conversion from '0' to '1', by which computer and digital based electronics devices may read the input signals and give potential output. So how fast a device can convert the binary number from input to output signal is a question of getting the fastest computer. Past research activity show that the addition of rare earth metal like Lanthanum organized a well change in ferroelectric properties of BFO for 10% addition of La and the further increasing in La caused minimizing the ferroelectric properties. On the other hand, as ferromagnetic materials Ni-Zn has huge success but to produce multiferroic composite the addition of BFO and NZFO is not convenient for the difference between their melting temperatures. To reduce the melting point of Ni-Zn ferrite it is required to add such kind of refractory materials which would be dominating the reduction of melting point of Ni-Zn. Addition of V_2O_5 shows brilliant result to reduce the melting temperature of Ni-Zn and 0.5% addition of V_2O_5 is better to control the melting point. So as optimum properties 10% La on BFO and 0.5% V_2O_5 on NZF addition have been taken under consideration to make multiferroic composites. Finally this research suggested the composition in $(1-x) BiFe_{0.9}La_{0.1}O_3 + x (Ni_{0.6}Zn_{0.4}Fe_{0.94}V_{0.06}O_4)$. The changing particle size from nano level to bulk structure had also been generated great success. So to obtain nano particle is proposed in this research and the effect of increasing annealing temperature with grain growth which would change the fundamental ferroelectric and ferromagnetic properties will be studied.

1.3 The Aims and Objectives of the Present Work

The objectives of the research works are as follows:

- To synthesize nano particle of BLFO and NZVFO multiferroic composites via typical solid state reaction method and mechanical method.
- In mechanical method the sample will be stirred in magnetic stirrer with pure acetone, particle dispersed by ultrasonic bath and washed by acetone in centrifuge.

- To anneal the synthesized particle where 100°C would be used for removing other light ingredients and after then different annealing temperature would be applicable to observe the effect of temperature on particle growing.
- To combine the X-ray diffraction pattern with Rietveld Analysis for analyzing structure and phases
- To study the surface morphology and grain growth by using FESEM
- To obtain magnetic properties and saturation magnetization by VSM
- To study the dielectric properties and permeability by impedance analyzer.

1.4 Reason for Choosing this Research Work

The multiferroic compositions will be prepared with highly pure materials by using chemical co-precipitation method. High purity powders of NiO (99.9%), ZnO (99.9%), Fe₂O₃ (99.9%), V₂O₅ (99.9%), Bi₂O₃ (99.9%) and La₂O₃ (99.9%), has been mixed thoroughly in an importance in an appropriate amount. Mixing has been performed in both dry and acetone media. The mixed powders are calcined at high temperature. After calcinations toroid and disk shapes samples are prepared and will be sintered at various temperature. The experimental methods would be used in this research work as follows:

- To mix the samples by agate and mortar as well as using conventional ceramic technique.
- Nanostructure formation will be confirmed by XRD and FESEM.
- Isothermal based annealing temperature variation effect microstructure and morphology analysis by SEM
- Frequency dependent complex permeability has been obtained by Impedance analyzer.
- AC resistivity, dielectric constant has been obtained by Impedance analyzer.
- Measurement of ferroelectric effect on multiferroic magnetization has been measured by VSM
- Magnetization, M-H loop, coercivity, retentivity etc will be measured from VSM data.
- Temperature dependence magnetization has been measured by VSM.

It is expected that the explored composites have large electric polarization and magnetization with small loss at room temperature will be useful applications. Our work may suggest a new approach for the design of multiferroics, composed of two compounds with same crystal structure. These research in soft magnetic materials and in multiferroic composites will help develop a profitable ferrite industry and can thus strengthen its spintronics industry in Bangladesh.

1.5 Background of Material Selection: Literature Review

From the above discussion it is clear that, to obtain strong multiferroic materials with highly featured ME coupling effect, the combination both of strong ferroelectric and ferromagnetic material is required. Otherwise, it would be tough to gain powerful electric or magnetic property by individual material which has only ferroelectric or ferromagnetic property. In this research, the proposed sample has the formula of $(1-x) \text{BiFe}_{0.9}\text{La}_{0.1}\text{O}_3 + x\text{Ni}_{0.6}\text{Zn}_{0.4}\text{Fe}_{0.94}\text{V}_{0.06}\text{O}_4$ where $x = 0, 0.1, 0.2, 0.3, 0.5, 0.7$ and 1 . The reason of material selection has been attributed by studying common problems with multiferroics. The literatures are given here:

Lanthanum Doped Bismuth Ferrite (BLFO)

According to recent studies BFO, having a suitable band gap (~ 2.2 eV) and excellent chemical stability, is also an important UV responsive semiconductor photo catalyst used for degradation of organic pollutants [1.23 - 1.25]. However, potential applications of BFO are greatly limited due to the presence of impurity phases, small spontaneous structure, ferroelectric reliability and high defect density, low insulation resistance caused by the reduction of Fe^{3+} species to Fe^{2+} and oxygen vacancies for charge compensation [1.26]. To tackle the leakage current issue of BFO, several research groups have attempted to partially substitute the Bi in the tetrahedral or octahedral sites of BFO by lanthanide elements (La, Ce, Nd, Sm, Eu, Gd, Tb, Dy, etc), transition metal and alkaline earth metal. This doping by non volatile ions controls the volatile nature of Bi in BFO, reduces the generation of oxygen vacancies and breaks the long-range cycloidal spin arrangement responsible for cancelling the magnetization in the rhombohedrally distorted perovskite structure [1.27 - 1.28].

Lanthanum-doped bismuth ferrite ($\text{Bi}_{1-x}\text{La}_x\text{FeO}_3$, $x = 0, 0.15, 0.30,$ and 0.45) crystallites were successfully synthesized by an ultrafast microwave assisted

hydrothermal method. Pure $\text{Bi}_{1-x}\text{La}_x\text{FeO}_3$ crystallites could be obtained when $x = 0.45$ as suggested by XRD patterns, but $x = 0.15$ represents the doping threshold beyond which a perovskite degradation has taken place in terms of the thermal properties (TG/DTA) and morphology (FESEM images). Indeed the ferroelectric transition temperature decreased from 813.9 to 803 C with increasing La doping and size distribution. The morphologies changed from homogenous semicubic in spheroidal aggregates with a size around 20 nm for undoped particles and with 2 nm for $x = 0.15$ doped particles to an irregular shape with several 10 and/or hundred nm for higher doping levels. Moreover the Raman spectroscopy confirmed that the $\text{La}_{0.15}\text{Bi}_{0.85}\text{FeO}_3$ is characterized by bismuth and iron chemical environments similar to the undoped bismuth ferrite. Even though some differences between BFO and $x = 0.15$ doped samples were observed, any significant variation at room temperature in the magnetic moment was seen [1.29].

The dielectric loss in $\text{Bi}_{1-x}\text{La}_x\text{FeO}_3$ ceramics increases dramatically with a small amount of La substitution ($x = 0.0-0.10$) and reaches a maxima at $x = 0.10$. Further increasing in the La content ($x = 0.15-0.25$), reduces the value of the dielectric loss back to the level for pure BiFeO_3 and minimum dielectric loss is reached when $x = 0.20$ and 0.25 [1.30]

It was found that pure BLFO crystallites could be obtained when x was less than 0.3. The morphologies of the obtained particles were sphere-like when $x \leq 0.15$ and changed into octahedral as $x = 0.3$. The XRD results demonstrated that the appropriate KOH concentration was beneficial for the formation of pure BLFO, and the reaction temperature and time played an important role on the formation of BLFO crystallites. A dissolution crystallization process was also discussed to explain the formation of the BLFO crystallites. The ferroelectric measurement showed that La doping greatly enhanced the remnant polarizations [1.31].

100 nm thick La-doped (10%) BFO thin films on $\text{SrRuO}_3/\text{DyScO}_3$ [110]o substrates were grown by pulsed laser deposition as reported elsewhere [1.32]. After deposition the samples were cooled from the deposition temperature (650 C) down to room temperature at different oxygen pressures ranging from near atmospheric pressure (500 Torr) over 10 Torr to 100 mTorr. This treatment introduces increasing amounts of oxygen vacancies in the thin film with decreasing oxygen pressure. In all cases atomic force microscopy imaging confirmed the presence of well defined surfaces. X-ray diffraction indicated fully strained epitaxial films and x-ray

reflectometry was used to verify film thickness. For our investigation we chose ordered stripe arrays of 109 domain walls, which is one possible wall type in a rhombohedral ferroelectric [1.33].

Vanadium Doped Nickel Zinc Ferrite (NZVF)

The variation of resistivity of $\text{Ni}_{0.65}\text{Zn}_{0.35}\text{Fe}_2\text{O}_4$ were maximum for $\text{V}_2\text{O}_5 = 0.6\%$ and higher order of Vanadium content reducing the resistivity. DI-electric constant as a function of Vanadium concentration decreased in minimum for $\text{V}_2\text{O}_5 = 0.6\%$ [1.34].

BFO-NZF multiferroic Composites

Perovskite–spinel di-phase compounds of BFO–NZFO and Mn doped BMFO–NZFO composites have been successfully prepared using sol–gel autocombustion and solid state reaction routes have been studied in impedance spectroscopy and dielectric properties of multiferroic $\text{BiFeO}_3/\text{Bi}_{0.95}\text{Mn}_{0.05}\text{FeO}_3\text{--Ni}_{0.5}\text{Zn}_{0.5}\text{Fe}_2\text{O}_4$ composites. Fine grained microstructures with grain sizes of $0.55\ \mu\text{m}$ and $0.52\ \mu\text{m}$ for the BFO–NZFO and BMFO–NZFO composites respectively were produced. The composites have shown Debye type dielectric relaxation with diffuse dielectric anomalies due to electron hopping mechanisms and Bi/O vacancies at low frequencies and ferrimagnetic/antiferromagnetic phase transition apart from induced magnetoelectric coupling at high frequencies. The conductivity in these composites is largely frequency dependent with dominant small polaron mechanisms. The temperature dependent impedance studies of the BFO–NZFO and BMFO–NZFO composites exhibit semicircles related to resistive contributions made by the grains and grain boundaries and thus support the frequency dependent conduction processes observed in dielectric studies. Mn doping in the BMFO–NZFO composite is effective in reducing the conductivity, dielectric losses and also instrumental in improving the impedance properties. Detailed studies of ferroelectric and magnetic parameters on these materials are underway to further find out their viability for use in real application systems [1.35].

Multiferroic composites of $x.\text{Bi}_{0.95}\text{Mn}_{0.05}\text{FeO}_3\text{--}(1-x).\text{Ni}_{0.5}\text{Zn}_{0.5}\text{Fe}_2\text{O}_4$, where x takes the values of 0, 0.2, 0.4, 0.5, 0.6, 0.8 and 1, have been prepared by combining sol–gel autocombustion and solid state methods. Fine grained microstructures with grain sizes in the range from $0.28\ \mu\text{m}$ and $0.55\ \mu\text{m}$ were produced. All the

composites have shown dielectric dispersion with the increase in frequency. Also, the samples up to $x=0.5$ have shown temperature dependent nonlinear dielectric behavior with diffuse dielectric anomalies. The sample with $x = 0.2$ produced two anomalies at low and high temperatures and the same were attributed to electron hopping mechanisms/bismuth or oxygen vacancies, and to ferrimagnetic to paramagnetic phase transition apart from induced magnetoelectric coupling, respectively. The low temperature anomaly for the $x=0.4$ sample was almost suppressed due to near stoichiometric balance of charge carriers. And, the sample with $x = 0.5$ has shown only one broad diffuse dielectric anomaly moving towards higher temperature with the increase in frequency because of synchronization between the frequencies of the applied field and hopping carriers. The conductivity in these composites is largely frequency dependent with dominant small polaron mechanisms. Detailed studies of ferroelectric and magnetic parameters on these materials are underway to further find out their viability for use in real application systems [1.36].

Synthesis of multiferroic $\text{Bi}_{0.9}\text{La}_{0.1}\text{Fe}_{0.95}\text{Mn}_{0.05}\text{O}_3 - \text{Ba}_{0.7}\text{Sr}_{0.3}\text{TiO}_3 - \text{Ni}_{0.8}\text{Zn}_{0.2}\text{Fe}_2\text{O}_4$ nanotubes with one closed end using a template-assisted sol-gel process. The morphology of the closed ends could be observed directly from the SEM and TEM images. It was found that the thickness of the closed end was bigger than that of a tube wall. In addition, the surface of the BLFMO nanotube wall was quite smooth. In contrast, both the BSTO–NZFO and BLFMO–BSTO–NZFO composite nanotubes displayed a less even surface. Compared to BLFMO nanotubes, the BLFMO–BSTO–NZFO nanotubes presented a larger M_s value due to combining with the ferromagnetic phase of NZFO. Such 1D multiferroic nanotubes have a potential application for multifunctional nano-devices. Meanwhile, a further study of their high-frequency ferroelectric and ferromagnetic properties is also needed [1.37 - 1.38].

1.6 Outline of the Thesis

The thesis has been configured into five chapters which are as follows:

Chapter I: Introduction:

In this chapter, a brief introduction to multiferroic composite with composition $(1-x)\text{BiFe}_{0.9}\text{La}_{0.1}\text{O}_3+x(\text{Ni}_{0.6}\text{Zn}_{0.4}\text{Fe}_{0.94}\text{V}_{0.06}\text{O}_4)$ nanostructure ferrites and organization of thesis. This chapter incorporates background information to assist in understanding

the aims and objectives of this investigation, and also reviews recent reports by other investigators with which these results can be compared.

Chapter II: Theoretical Background

In this chapter, a brief description of theories necessary to understand the overview of multiferroic, single phase multiferroic, multiferroic composite as well as nanostructure multiferroics, perovskite structure, different phase diagrams, ferroelectricity and ferromagnetism in multiferroic materials, spinel structure of ferrite, ferromagnetism and multiferroicity etc. have been discussed in detail.

Chapter III: Experimental Background

In this chapter, the methodology of nanostructured multiferroic composite preparation, the experimental procedures are briefly explained along with the description of sample preparation, raw materials. This chapter deals mainly with the design and construction of experimental and preparation of multiferroic composite with composition $(1-x)\text{BiFe}_{0.9}\text{La}_{0.1}\text{O}_{3+x}(\text{Ni}_{0.6}\text{Zn}_{0.4}\text{Fe}_{0.94}\text{V}_{0.06}\text{O}_4)$ nanostructure ferrite samples. The fundamentals and working principles of the measurement set up are discussed.

Chapter IV: Result and Discussion

In this chapter, results and discussion are thoroughly explained. The XRD analysis, representation of XRD data with Rietveld Refinement, study of microstructure with various isothermal stages, magnetization of ferromagnetic effect on multiferroic with experimental samples and measurement of ferroelectric properties of multiferroic composite with composition $(1-x)\text{BiFe}_{0.9}\text{La}_{0.1}\text{O}_{3+x}(\text{Ni}_{0.6}\text{Zn}_{0.4}\text{Fe}_{0.94}\text{V}_{0.06}\text{O}_4)$ nanostructure ferrites are presented and discussed step by step.

Chapter V: Conclusion

In this chapter, the results obtained in this study are summarized. Suggestions for future work on these studies are included. References are added at the end of the thesis.

THEORETICAL BACKGROUND

2.1 Overview of Multiferroic

Ferroic order materials have attracted the attention of researchers for its formation of domains which enable to show hysteresis behavior in a field-response loop [2.1]. Ferroelectricity is the property of materials that developed a spontaneous electrical polarization even the deficiency of external electric field. Otherhand the ferromagnetism is most ferroic ordered phenomenon where a spontaneous non-zero magnetization develops even the external magnetic field may be absent. Similarly two other ferroic orders exist which are ferroelastic and ferrotorroidic materials. The ferroelastic materials shows impulsive stretching without providing an external strain and a ferrotorroidic material represents a spontaneous improvement of magnetic vortices [2.1]. If a material has two of ferroic order then it would be considered as multiferroics material.

From the application view in practical purposes, magnetic materials have shown multifunctional appliance including magnetic memory, sensors, inductors, transducers, actuators etc. Low power consumption is one of major criteria for choosing materials where the aptitude of controlling magnetism with an electric field has represented wide range of research activities. In general the electric fields do not act together with magnetic materials but some materials have the properties where both magnetic and electric field may be attributed with materials.

In recent years multiferroic materials have attracted the attention of researchers for both ferroelectric magnetic properties. The mutual contributions of electric and magnetic phenomenon of multiferroic materials provide the opportunities to develop new devices in storing data with spintronics mechanism [2.2 – 2.3]. Spintronics material comes from spin electronics where the electron can spin in up or down state by changing the signal. The multiferroic materials also exhibit spintronics properties where electron spin would be dominated by changing magnetic field. For ferroelectricity material requires B-site ions with d^0 electrons, whereas the ferromagnetism needs partially filled d^j electrons [2.4]. Among perovskite structured materials BiFeO_3 is rarely shown both of these properties. For the development of devices it is very urgent to optimize both of ferroelectric and ferromagnetic properties in between on content by coupling of these properties. So combination of such

materials having high ferromagnetic and high ferroelectric properties may be designed to optimize the multiferroic properties and enhancing a better treatment on treating electro-magnetic switching junction.

Rather than co-existence of two ferroic orders, it is more important and suitable from application interest to strong coupling interaction between two orders of multiferroic. The coupling between two ferroic factors is able to construct additional parameters like magnetoelectric (ME) effect, which is more convenient for electronics applications. The magnetoelectric reaction is the manifestation of an electric polarization P on applying a magnetic field H , i.e., so-called direct ME effect:

$$P = \alpha \Delta H \quad \text{or} \quad \Delta E = \alpha E \Delta H \quad (2.1)$$

where E represents electric field and α (αE) is the ME (ME voltage) coefficient. It is usual to modify the electric polarization by magnetic field or a voltage output which can be produced by applying a magnetic field on the materials via the ME coupling.

The direct ME effect has a simultaneous converse ME effect that occurs of a magnetization M upon applying an electric field E ,

$$\Delta M = \alpha \Delta E \quad (2.2)$$

which refers that the inflection of magnetism by an electric field. The simultaneous manifestation in between ferroelectric and ferromagnetic orders responsible to form strong enough ME coupling and such combination of polarization effect carried out hysteresis response as a function of applied magnetic field. These P–H or M–E hysteresis loops look to some extent analogous to the well-known ferroelectric or ferromagnetic hysteresis loops. The effects of ME on multiferroic materials lead to produce some extra ordinary appliances like sensors, transducer, filters, oscillators, phase shifters, memory devices, and so on.

In a multiferroic material with ferroelectric and ferromagnetic orders simultaneously habituated as well as strong enough ME coupling, ideally, the electric (magnetic) polarization would show a hysteresis response as a function of the applied magnetic (electric) field, as schematically demonstrated in Figure 2.1. These P–H or M–E hysteresis loops look to some extent analogous to the well-known ferroelectric or ferromagnetic hysteresis loops. The effects of ME on multiferroic materials lead to produce some extra ordinary appliances like sensors, transducer, filters, oscillators, phase shifters, memory devices, and so on.

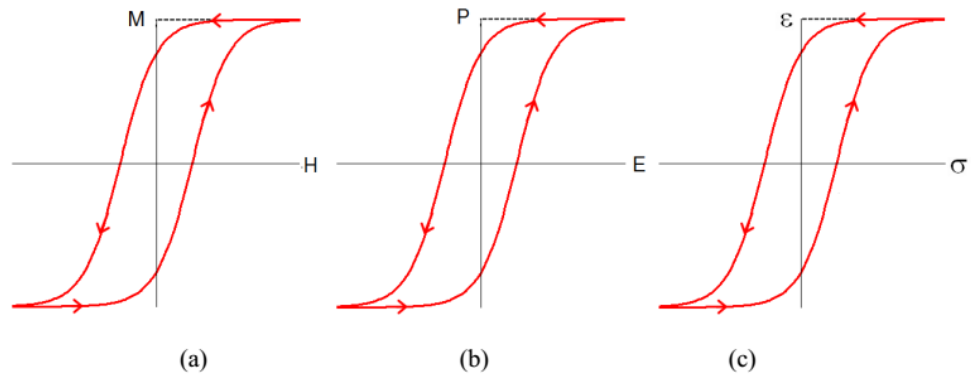


Figure 2.1: Hysteresis loops of (a) ferromagnetic, (b) ferroelectric and (c) ferroelastic materials.

A ferromagnetic material generally shows hysteresis in an $M - H$ loop whereas the ferroelectric material shows hysteresis in a $P - E$ loop. The overlap has been occurred in between two ferroic ordered materials to develop magnetoelectric multiferroic where magnetic polarization can be induced by applying external electric field or vice-versa. It should be noted that the electric field is much easier to apply than magnetic field which can switch at a fast rate and intrinsically contributed on energy consumption. So it is wise to use electric signals to produce magnetic field in device development. Multiferroic spintronics materials can afford the switchable magnetic properties by applying electric field and on the contrary magnetically switchable polarization is required in improving potential devices. The multiferroic materials, in general, split into two types: single phase [2.5 – 2.9] and composites [2.10 – 2.11].

2.1.1 Single Phase Multiferroic

Among known multiferroics, BiFeO_3 (BFO) shows high Magnetoelectric (ME) effect at room temperature and has proper ferroelectric parameters with first order paraelectric to ferroelectric transition at very high temperature ($T_C \sim 830^\circ\text{C}$). The electric polarization as a by-product of cooling near Neel point ($T_N \sim 370^\circ\text{C}$) has created helical-type magnetic ordering [2.12 – 2.15].

But in device application BFO may not so useful for its very low value of magnetization and electric polarization. To solve this problem several materials have been doped to see the effect of ME during changing the electrical and magnetic phase.

From structural point of view BFO belongs rhombohedrally indistinct perovskite structure with R3c space group [2.16]. High leakage current is one of major problem of BFO to use in device which may be minimized by obtaining nanostructures for reducing in transferable charges or achieved directional growth of thin film along the (111) direction but in bulk materials it is frequently observed [2.17 – 2.19].

The ME effect has been observed as an intrinsic effect in some natural material systems, which have been under intensive study recently, [2.20 – 2.23] motivated by potential applications in information storage, spintronics and multiple-state memories. So far, over ten different compound families have been widely investigated as multiferroic ME materials such as well-known BiFeO₃ (BFO) and rare earth manganates. As discussed before the intrinsic ME effect exists in the single-phase compounds, most multiferroic compounds exhibit low Curie temperatures (below room temperature), and a high inherent ME coupling (especially above room temperature) has not yet been found in the single-phase compounds. However, BiFeO₃ is G-type antiferromagnetic or only very weak ferromagnetic. The low critical temperatures and/or weak ME coupling of the single phase compounds hinder their practical applications. Several recent articles have summarized and reviewed research progress in single-phase multiferroic materials [2.24].

2.1.2 Multiferroic in Composites

Due to the limitations on enabling strong enough ME effect by single phase multiferroic contents, researches had aimed to improve the situation by tasting and combining different materials and found genius results not only from experimental observations but also the theoretical aspects are more convenient to understand the fact. In ME composites, there has no significant effect of constituent phases but the interaction effect of mix together the phases by sharing each property with other which leads outstanding ME effect.

In 1972, Ban Suchtelen, first introduced ME effect in multiferroic composites [2.25]. The ME effect of composites can be defined as the result of product of magnetostrictive effect (magnetic/mechanical effect) in the magnetic phase and the piezoelectric effect (mechanical/electrical effect) in the ferroelectric one, which also referred as, [2.26]

$$\text{Direct ME effect} = \frac{\text{Magnetic}}{\text{Mechanical}} \times \frac{\text{Mechanical}}{\text{Electric}}$$

$$\text{Converse ME effect} = \frac{\text{Electric}}{\text{Mechanical}} \times \frac{\text{Mechanical}}{\text{Magnetic}} \quad (2.3)$$

The elastic interaction is the reason of coupling between electrical and magnetic parameters among multiferroic composites. The ME effect of composites is extrinsic which depends on microstructure and coupling interaction across magnetic-piezoelectric interfaces. Above room temperature many bulk ME composites shows a strain modified ME effect [2.10]. The large ME response for multiferroic composite is greater than single phase multiferroic materials thus the composites are extrinsic. As a result the composite multiferroics are applicable for its ME effect utilization.

In recent times, Nan *et al.* [2.10] have obtained a inclusive assessment on the chronological perception, standing and future directions of multiferroic ME composites. They found that, bulk ME composites have special parameters to improve the quality of materials for ME applications.

2.1.3 Bulk ME Composites

From the inception of developing ME effect on multiferroic composite by van Suchtelen, the incredible success had been assumed. Before 21st century the well defined ceramic composites like BaTiO₃ (BTO) or Pb(ZrTi)O₃ (PZT) did not exert a pull on interest from the view of experimental studies and these kind of ceramic composites did not give hopeful result for further development of multiferroics. In the early of 21st century some experiments gave good result to consider the multiferroic composites for industrial applications according to the ME effect. The remarkable progress in ME bulk composites was obtained for adding giant magnetostrictive rare-earth-iron alloy Tb_{1-x}Dy_xFe₂ (Terfenol-D) in 2001 [2.27]. The Terfanol-D based bulk composites were provided giant ME (GME) response [2.27] in association with theoretical and experimental observations made significant technological applications as ME devices [2.28 - 2.29].

2.1.4 Composites in Ceramic

Mixing ceramic contents with multiferroic gives brilliant success in generating ME devices. The combination of ferroelectric oxides (Perovskites) and magnetic oxides (Ferrites) have been chosen in account to obtain bulk ME ceramic composites which is enough strong to provide GME along the multiferroics. The effect of sintering on composites has contributed to change the microstructure and formed bulk

content as an ingredient to larger ME. Ceramic contents like Bismuth, Barium, Titanium, Strontium etc show many applications in ferroelectric field which also make sense to apply in many devices. High temperature co-sintering have enabled the ferroelectric mechanism inside multiferroic composites which would be no more than the sintering temperature of each content having the composites thus the material may not melt. Recent research shows that the chemical solution processes and novel sintering techniques [e.g., spark-plasma sintering (SPS) [2.30] and microwave sintering [2.31] have been working to formulate the identical ceramic composites where some enhancement has already been gained.

From experimental evidence, the known fact is that the single phase materials constantly resulted weak magnetoelectric (ME) effect even the temperature being low. Research provides that the multiferroic composites can be commercially used in association with combination of ferroelectric/piezoelectric (FE) and ferromagnetic /magnetostrictive (FM) phases. According to the interest on multiferroic composites the nano synthesized heterostructures has extraordinary result on growing strong ME effect.

2.1.5 Nano Structured Multiferroics

Nano particles and nano materials are widely used not only for size effect but also some unique and identical improvement has been seen in electrical, magnetic, mechanical and optical properties which may be originated by low dimensionality and quantum scale confinement of particles [2.32]. One of the most studied and promising multiferroic materials to date is bismuth ferrite (BiFeO_3), which has a relatively simple structure and at the same time uncommon properties: bismuth ferrite possesses two coupled order parameters - ferroelectricity and antiferromagnetism at room temperature [2.33 – 2.34]. Moreover, bismuth ferrite sets a standard in the global search for new multiferroic materials. Nevertheless, even in bismuth ferrite the magnetoelectric coupling is weak. However, in 2003, Ramesh's group successfully created epitaxial BiFeO_3 multiferroic thin film heterostructures [2.35] that possess greatly enhanced multiferroic properties. These films display a roomtemperature spontaneous polarization that is almost an order of magnitude higher than that of the bulk. Therefore, the creation and development of artificial nanoscale structures is very promising. Thus, multiferroic materials hold the future for ultimate nanodevices and

are hence very interesting for theoretical and practical research, especially in nanoscience.

There is a fast-growing body of research devoted to the manufacture and characterization of complex nanoscopic shapes other than thin films. These 3D nanostructures generally have their own distinctive size effects, and multiferroic BiFeO₃ is no exception. For example, nanocrystals of BiFeO₃ show enhanced magnetization and superparamagnetism correlated with decreasing diameter [2.36] (Fig. 24). Similar size-induced magnetism has also been reported for BiFeO₃ nanowires [2.37] and nanopowders [2.38]. This is thought to be due to the large fraction of uncompensated spins from the surfaces of the nanocrystals, an effect that is well known from classic antiferromagnets such as NiO [2.39].

2.2 Perovskite Structure

Perovskites have the general formula ABX₃ where the coordination number is XII A^{2+VII} B⁴⁺ X₃²⁻ and they are named after the mineral Perovskite, the oxygen ion is in face centered. In its ideal form, the perovskite structure is a cubic closed pack structure. In this structure of BiFeO₃, the Bi cations are cuboctahedrally surrounded by 12 oxygen ions and the Fe cations are octahedrally surrounded by 6 oxygen ions. For the perovskite structure two different types of unit cells are used. In the first unit cell the bigger Bi cations are in the middle and the smaller Fe cations are in the corners of the cube. The oxygen-anions are on the edges. In the second unit cell the Fe cations are located in the middle, the oxygen-ions are on the faces and the Bi cations are in the corners of the cube. In some perovskite structures, as for example in BiFeO₃, the position of the Fe cations is not exactly located in the center of the octahedral hole. This leads to a polarisation and a high dielectric constant of the unit cell. This is the reason why these materials are used in capacitors, sensors and electronic components.

Table 2.1: Site preference of perovskite structured materials

ABO₃	
A Site	B Site
Bi ³⁺ , Ca ³⁺ , La ³⁺ , Ce ³⁺ , Nd ³⁺ , Sm ³⁺ , Eu ³⁺ , Gd ³⁺ , Tb ³⁺ , Dy ³⁺ , Ho ³⁺ , Er ³⁺ , Yb ³⁺ , Lu ³⁺	Al ³⁺ , Cr ³⁺ , Fe ³⁺ , Ga ³⁺ , In ³⁺ , Sc ³⁺ , Ti ³⁺

For the $A^{3+}B^{3+}O^3$ perovskites the most symmetric structure observed is rhombohedral R3c (e.g. $LaAlO^3$) which involves a rotation of the BO^6 octahedra with respect to the cubic structure in Figure 2.2(a). However, this distortion from the perfect cubic symmetry is slight [100]. Many early studies reported that the perovskites showed mainly cubic or pseudocubic structure, but as work on these systems continued, the number of proposed symmetries increased. Literature suggests that many of the materials exhibit the orthorhombic Pnma (or Pbnm) [2.40] distorted structure at room temperature.

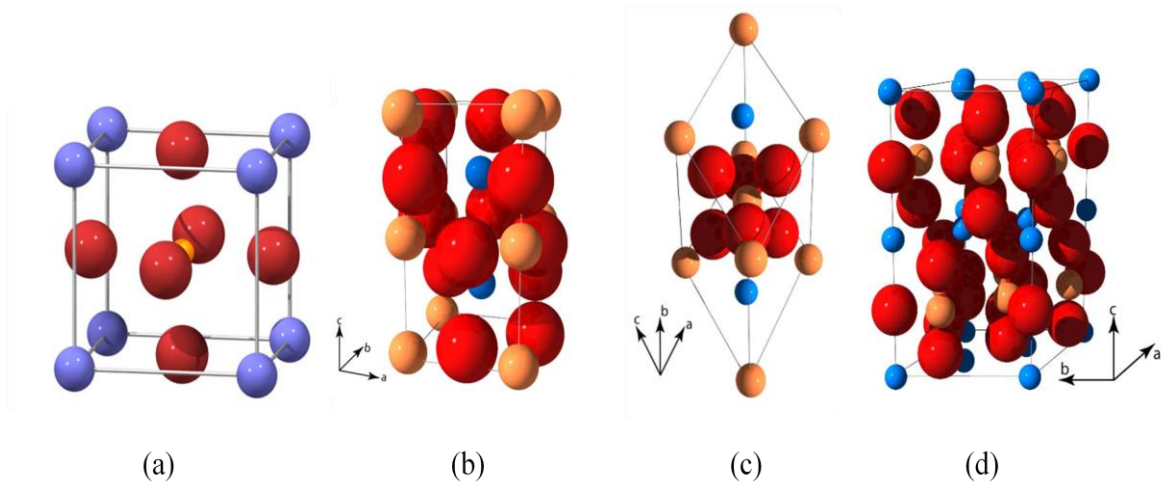


Figure 2.2: (a) Cubic perovskite unit cell, (b) Pnma-orthorhombic perovskite unit cell, (c) R3c-rhombohedral perovskite unit cell and (d) P63cm hexagonal perovskite unit cell. Blue spheres represent the A cations, yellow spheres represent the B cations, and red spheres represent oxygen anions forming an octahedra.

This distorted structure can be seen in Figure 2.2(b) (it is double the size of the cubic cell). Special positions for the Pnma distortion are given in Table 2.2. A further distortion is also possible resulting in a rhombohedral structure with the space group R3c [2.40]. The rhombohedral structure is shown in Figure 2.2(c); special positions are given in Table 2.2. A further distortion can be seen with the formation of a hexagonal P63cm structure, which can be seen in Figure 2.2(d), with special positions given in Table 2.2. In this variant, the lattice distortions are so great that the A cations are now VII coordinate and the B cations are V coordinate and the structure has lost its direct similarity with the perovskite symmetry.

Table 2.2: Atomistic positions in cubic, orthorhombic (Pnma) and rhombohedral (R3c) perovskites [2.40]

Structure	Site	Location	Co-ordinates
Cubic	A cation	(2a)	(0, 0, 0)
	B cation	(2a)	$\left(\frac{1}{2}, \frac{1}{2}, \frac{1}{2}\right)$
	O anion	(6b)	$\left(\frac{1}{2}, \frac{1}{2}, 0\right) \left(\frac{1}{2}, 0, \frac{1}{2}\right) \left(0, \frac{1}{2}, \frac{1}{2}\right)$
Orthorhombic (Pnma)	A cation	(4c)	$\pm \left[\left(u, v, \frac{1}{2}\right) \left(\frac{1}{2} - u, v + \frac{1}{2}, \frac{1}{2}\right) \right]$
	B cation	(4b)	$\left(\frac{1}{2}, 0, 0\right) \left(\frac{1}{2}, \frac{1}{2}, 0\right) \left(0, 0, \frac{1}{2}\right) \left(0, \frac{1}{2}, \frac{1}{2}\right)$
	O(1) anion	(4c)	$\pm \left[\left(m, n, \frac{1}{4}\right) \left(\frac{1}{2} - m, n + \frac{1}{2}, \frac{1}{4}\right) \right]$
	O(2) anion	(8d)	$\pm \left[\begin{array}{l} (x, y, z) \left(\frac{1}{2} - x, y + \frac{1}{2}, \frac{1}{2} - z\right) \left(-x, -y, z + \frac{1}{2}\right) \\ \left(x + \frac{1}{2}, \frac{1}{2} - y, -z\right) \end{array} \right]$
Rhombohedral (R3c)	A cation	(6a)	$\left(0, 0, \frac{1}{4}\right)$
	B cation	(6b)	(0, 0, 0)
	O anion	(18e)	$\left(x, 0, \frac{1}{4}\right)$

All perovskite distortions that maintain the A and B site oxygen coordinations involve the tilting of the BO₆ octahedra and an associated displacement of the A cation. For the orthorhombic structure, these octahedra tilt about the b and c axes, while in the rhombohedral structure the octahedra tilt about each axis [2.40]. This octahedral tilting is related to the sizes of the A and B cations (as described by the tolerance factor), for example AGaO₃ is more distorted than AAIO₃ [2.40]. The distortion from cubic to orthorhombic perovskite is shown in Figure 2.3.

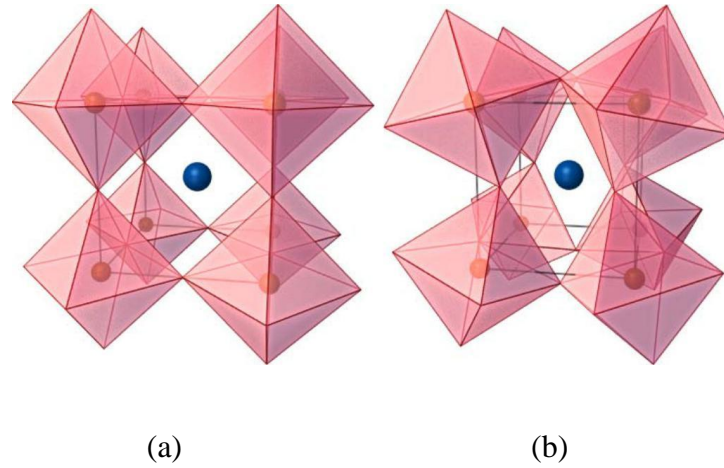


Figure 2.3: Perovskite distortion from (a) cubic to (b) orthorhombic

2.2.1 Phase Transition in Perovskite BiFeO_3 single crystals

The crystal structure of bismuth ferrite is a rhombohedrally-distorted perovskite that belongs to the space group $R3c$. In Figure 2.4 (a), the unit cell of BiFeO_3 is shown in its hexagonal representation ($[001]_{\text{hex}}$, $[100]_{\text{hex}}$, $[110]_{\text{hex}}$, $[010]_{\text{hex}}$ are hexagonal axis). Alternatively, in some cases, a pseudocubic representation has been used, where $[111]_c$ is equivalent to $[001]_{\text{hex}}$.

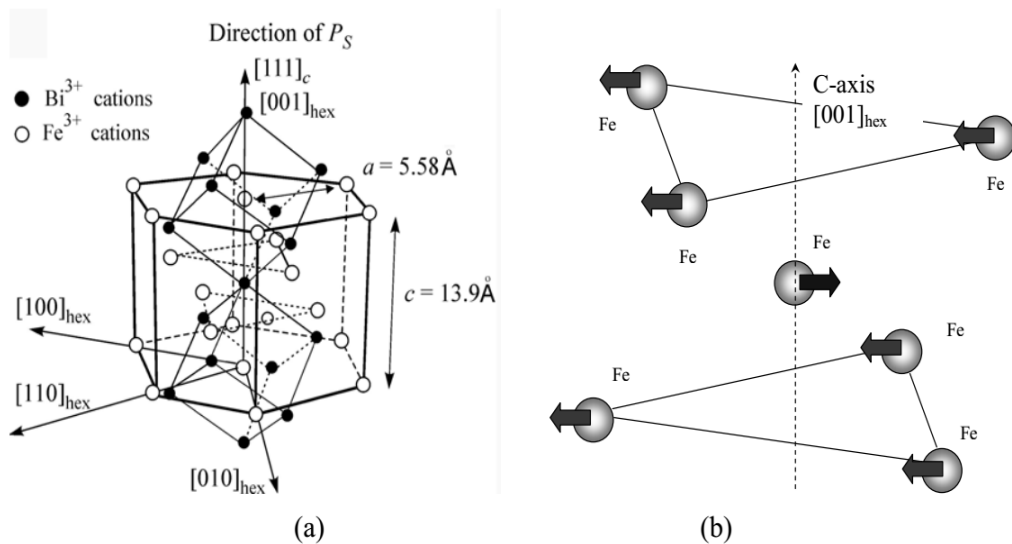


Figure 2.4: Crystallographic (a) and magnetic (b) structure of BiFeO_3

Oxygen atoms (not shown) occupy face-centered sites of the Bi cubic framework. BiFeO_3 has been shown to be ferroelectric with its polarization oriented along the rhombohedral c-axis (i.e., $[111]_c$) due to the displacement of Bi, and Fe, O relative to one another [2.41]; and shortly thereafter, neutron diffraction studies

revealed antiferromagnetic (AFM) ordering along [111]c [2.42]. Spins in neighboring positions are antiparallel with each other, resulting in an AFM ordering of the *G*-type, as illustrated in Figure 2.4(b).

2.2.2 The Phase Diagram of BiFeO₃

The phase diagram for the system Bi₂O₃/Fe₂O₃ has been mapped out [2.43 - 2.46] and is shown in Figure 2.5. Same amount of Bi₂O₃ and Fe₂O₃ involves forming BiFeO₃ and at higher temperature the reflection of decomposition can be obtained as follows:



Bismuth ferrite is very prone to show parasitic phases that tend to nucleate at grain boundaries and impurities [2.47]. It has been argued that BiFeO₃ is in fact metastable in air, with optically visible impurity spots appearing well below the melting temperature [2.46, 2.48 - 2.49]. Impurities and oxygen vacancies are also important for thin films, because they are known to artificially enhance the remnant magnetization [2.50 - 2.51] shown in Figure 2.5. Minimizing them requires very careful tuning of growth parameters, particularly oxygen pressure [2.51]. At room temperature under applied fields of ca. 200 kVcm⁻¹ (typical switching voltages across thin films), BiFeO₃ decomposes, yielding magnetite Fe₃O₄ as a by-product [2.52]. This was somewhat surprising and is thought to occur via the following reaction

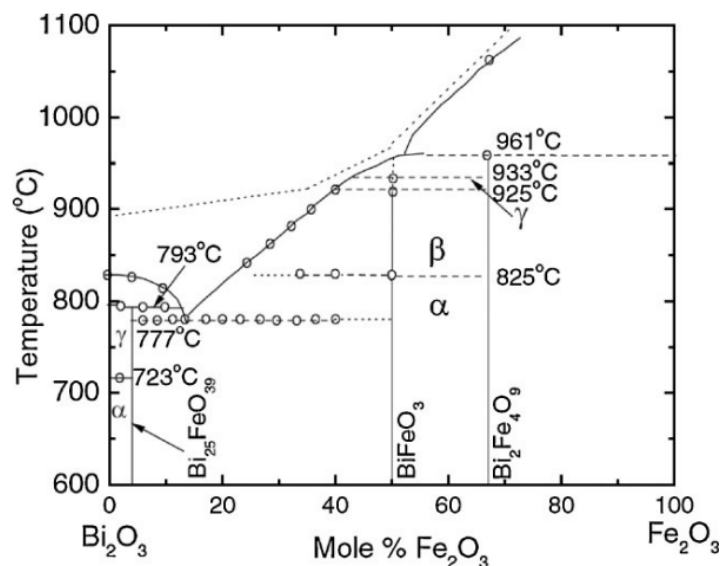
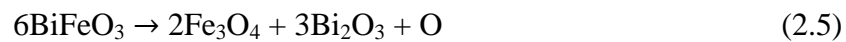


Figure 2.5: Phase diagram of BiFeO₃ where the relevant composition is illustrated [2.46].

The magnetite phase was unambiguously identified by means of micro-Raman studies; the Raman spectra of Fe_3O_4 is quite distinct and unlike those of Fe_2O_3 . However, the Bi_2O_3 was not detected, possibly because it is a well-known glass-forming compound, or perhaps because of its evaporation during thermal decomposition. Bi_2O_3 melts at a temperature slightly above 800°C [2.46].

2.3 Ferroelectricity and Ferromagnetism inside Multiferroic Materials

In previous chapter it was discussed that, the multiferroic properties are formed by the combination of minimum two ferroic ordered materials. Some time only ferroelectricity is not satisfactory to generate magnetism inside materials but few materials have both of property to form it. Other hand to obtain strong ME effect it is very important to know the phenomenon of multiferroics. In this research, the main intension has putted on understanding the multiferroics in association with ferroelectric and ferromagnetic properties. So this chapter will illustrate to understand the basic facts inside multiferroic materials.

2.3.1 Ferroics

Several crystals undergo phase transitions if external parameters such as pressure or temperature are changed. If, in a certain crystal, at least one of these phase transitions is accompanied by a spontaneous change of directional symmetry, one speaks of a ferroic crystal. Landau and Lifshitz [2.53] pointed out that, crystal symmetry may spontaneously be broken even if the atoms in the crystal itself are rearranged continuously, which is obvious if one for example imagines a cubic crystal becoming distorted to tetragonal shape by an arbitrary small displacement of lattice atoms.

A phase transition involving a spontaneous break of symmetry caused by a continuously evolving order parameter η is called a second-order phase transition. In our case, the order parameter is the magnetization M , polarization P or strain ϵ and the phase transition to the ferroic state occurs if the order parameter becomes different from zero. It is important to note that this ordering need to be *spontaneous* thus must occur even in the absence of an external field. The analogies between the different ferroic materials are shown in [Table 2.1](#). In the absence of applied fields, thermodynamic equilibrium is determined by minimizing the Helmholtz free energy F

(η , T) with respect to the order parameter η . Thus the necessary condition for equilibrium is given by [2.54]:

$$\frac{dF}{d\eta} = 0 \quad (2.6)$$

If an external field ξ is applied, which in our case is given by a magnetic field H , electric field E or a mechanical stress σ , the total free energy is quantified by the Gibbs relation:

$$G(\eta, \xi, T) = F(\eta, T) - \xi\eta \quad (2.7)$$

and thermodynamic equilibrium is reached if

$$\begin{aligned} \frac{\partial G}{\partial \eta} &= 0 \quad , \quad \frac{\partial^2 G}{\partial^2 \eta} > 0 \\ \frac{\partial F}{\partial \eta} &= \xi \quad , \quad \frac{\partial^2 F}{\partial^2 \eta} > 0 \end{aligned} \quad (2.8)$$

is fulfilled. Therefore equation (2.6) describes the adjustment of the order parameter to balance the internal energy with the work caused by the external field.

If consider $T < T_c$, the breaking of symmetry leads to a spontaneous ordering of magnetization, polarization or strain in the crystal even without an external field, and the material is now in its ferromagnetic, ferroelectric or martensite phase. If no external field is applied, all orientations of the order parameter are equally favorable and therefore domains enclosing regions of equally oriented order parameter emerge in such a way that the macroscopic ordering may remain zero. The dependence of the order parameter on an external field can be described by an appropriately chosen Helmholtz free energy F , which for ferromagnetic and ferroelectric materials can be derived from the Taylor expansion of the Helmholtz free energy shown in [2.55] as:

$$F(\eta) = \begin{cases} \frac{1}{2}\kappa(\eta + \eta_R)^2 & , \eta \leq -\eta_I \\ \frac{1}{2}\kappa(\eta - \eta_R)^2 & , \eta \geq \eta_I \\ \frac{1}{2}\kappa(\eta + \eta_R)^2 \left(\frac{\eta^2}{\eta_I} - \eta_R\right) & , |\eta| < -\eta_I \end{cases} \quad (2.9)$$

Table 2.3 shows the common parameters used in ferocity of materials where the similarity between different ferroic materials is given.

Table 2.3: Analogies between different ferroic materials [2.56].

Variables	Ferromagnetic	Ferroelectric	Ferroelastic
H	Magnetization M	Polarization P	Strain ε
Ξ	Magnetic Field H	Electric Field E	Stress σ
$T \geq T_C$	Paramagnetic Phase	Paraelectric Phase	Austenite Phase
$T < T_C$	Ferromagnetic Phase	Ferroelectric Phase	Martensite Phase
Domain Walls	Bloch or Neel Walls	Ferroelectric Domain Walls	Boundaries between variants

For $T < T_c$, $G(\eta, \xi)$ has the shape of a double well potential, unlike for $T = T_c$ where it shows a single well potential [2.55]. The order parameter can now be imagined as a ball resting in the potential in Figure 2.6(a) - it will stay in a local minimum unless the applied field is large enough to let it overcome the potential barrier to the global minimum of the potential.

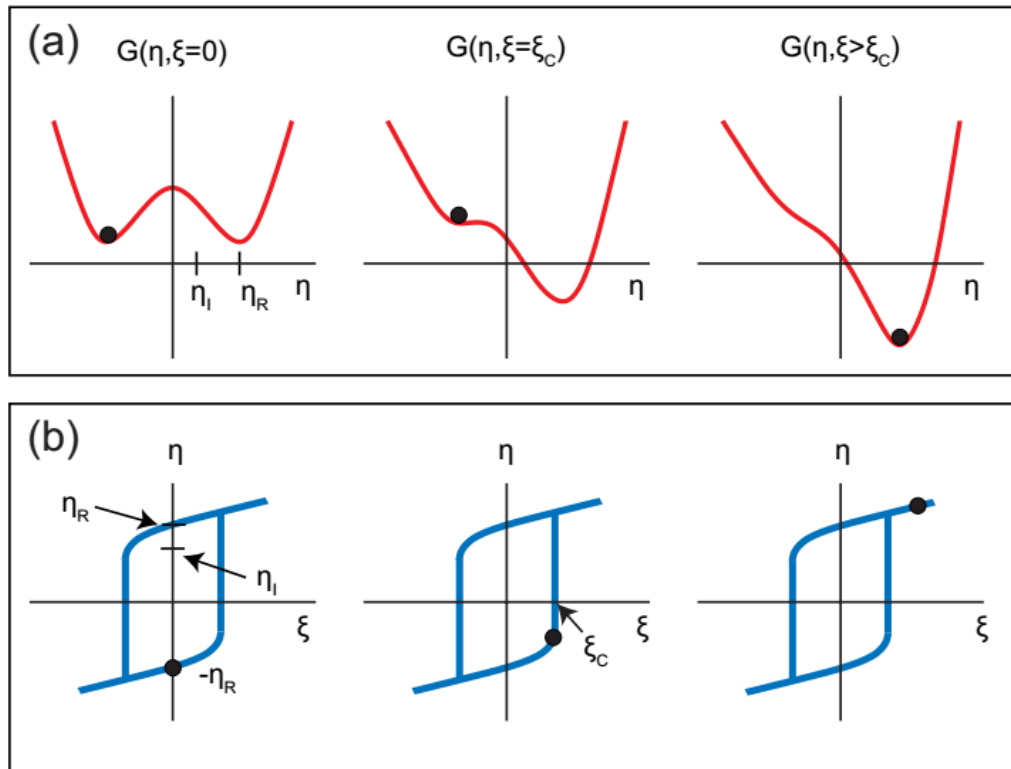


Figure 2.6: (a) Gibbs free energy and (b) resulting hysteresis of the order parameter $\eta \in \{M, P, \varepsilon\}$ depending on the external field $\xi \in \{H, E, \sigma\}$

Hence hysteresis can only occur if the potential shows more than one well, thus only in ferroic materials. For ferroelastic materials, the Helmholtz free energy can be derived in a similar way [2.57], but as the microscopic physical ordering is quite different for ferroelastic materials if compared to ferromagnetic and ferroelectric materials, other parameters need to be involved, although $G(\eta, \xi)$ qualitatively shows the same evolution as depicted in Figure 2.6(a).

2.3.2 Ferroelectricity

Ferroelectricity was discovered in 1921 by Valasek in the U.S. A ferroelectric is a material which undergoes a phase transition from a high-temperature, high-symmetry (paraelectric) structure that is an ordinary dielectric to a low-temperature, low-symmetry (ferroelectric) structure that has spontaneous macroscopic electric polarization. The polarization is reversible, non-volatile and its direction can be switched by applied field. In other words, ferroelectric crystals can be seen as an assembly of batteries with a particular orientation, which remains stable unless an external electric field is applied to change its direction shown in Figure 2.7. Polarization arises below a certain phase transition temperature called the Curie temperature - T_c .

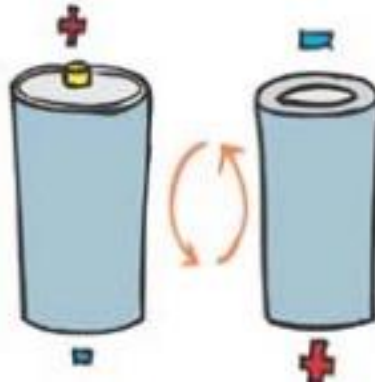


Figure 2.7: Schematic view of ferroelectricity where non volatile & reversible polar state is illustrated

The spontaneous polarization of ferroelectric materials implies a hysteresis effect. The concept of electric polarization is the key to understanding ferroelectricity. Ferroelectrics also behave as high dielectric-constant insulators useful in the development of capacitors and energy storage materials. The most widely studied and used ferroelectrics today are perovskite-structure oxides, ABO_3 shown in Figure 2.8, which possess a prototypical cubic structure at high temperature.

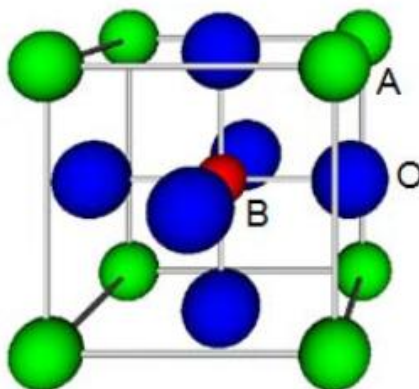


Figure 2.8: Schematic view of the perovskite oxide structure

The cubic perovskite structure is characterized by a small cation, B, at the center of an octahedron of oxygen anions, with large cations, A, at the unit cell corners. A structural distortion from a high symmetry type to a low symmetry type occurs below the Curie temperature. This distortion is accompanied by an off-center shift of the small cation, which is the major factor giving rise to the spontaneous polarization. There are a few different mechanisms that cause ferroelectricity:- ferroelectricity in multiferroic perovskites.

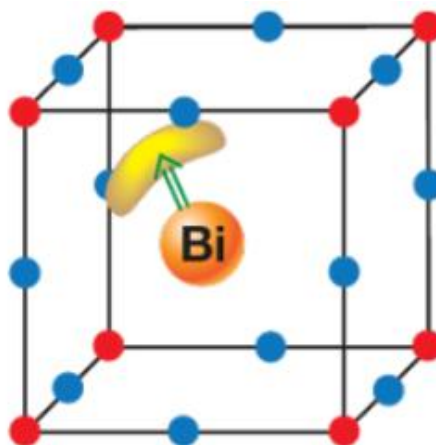


Figure 2.9: In BiFeO_3 the ordering of lone pairs (yellow "lobes") of Bi^{3+} ions (orange), contributes to the polarization (green arrow) [2.58].

The off-center shifts of the transition metal ion cause ferroelectricity in these systems. This ion is thought to form strong covalent bonds with one (or even three) oxygens, using its empty d states. However, the theory for this case has not yet been made clear. Ferroelectricity caused by stereochemically active lone pair cations, e.g. Bi^{3+} in BiFeO_3 shown in Figure 2.9.

These divalent ions have two 5s or 6s electrons that do not participate in chemical bonding. Cations containing a 5s (6s) lone pair of valence electrons usually break local inversion symmetry. The small B cation in ferroelectric perovskite oxides lowers its energy by shifting along one of the $[111]$ directions shown in Figure 2.10.

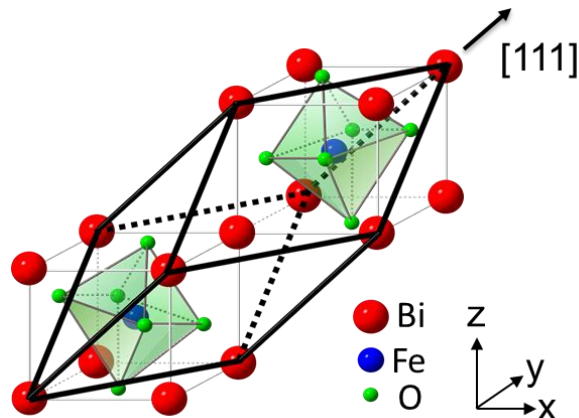


Figure 2.10: Schematic drawing of the crystal structure of perovskite BiFeO_3 (space group: $R3c$). Two crystals along $[111]$ direction are shown in the figure.

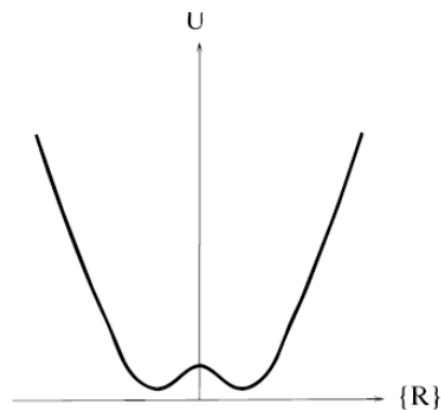


Figure 2.11: Characteristic double-well potential energy as a function of the position of the B cation between the oxygen anions in perovskite ferroelectrics [2.58].

This structural modification leads to a system with a “double-well” shaped potential energy shown in Figure 2.11, which describes the position of the small cation as a function of distance between the oxygen anions. - ferroelectricity due to charge ordering, often observed in transition metal compounds. Similar to the mechanism for

ferromagnetism, ferroelectricity is realized in a material when an external electric field creates a spontaneous polarization, which is an alignment of dipole moments across a particular volume of the material [2.59]. An example of the typical test for polarization switching is a hysteresis loop, shown in Figure 2.1. The most commonly utilized materials with the ability to switch polarization are metal oxides of the perovskite family such as barium titanate [2.60], lead zirconate titanate [2.61 - 2.62], and lithium niobate [2.63 - 2.67]. The most important applications for ferroelectric materials include data storage, sensing, energy harvesting and electro-optic devices.

The ferroelectric order parameter \mathbf{P} is defined as the dipole moment p per unit volume V :

$$P = \frac{dp}{dV} \quad (2.10)$$

which is related non-linearly to the electric field \mathbf{E} as depicted in Figure 2.1(b) by:

$$E = \frac{dF}{dP} \quad (2.11)$$

This again will only hold true for \mathbf{P} parallel to \mathbf{E} . In general, the electric field dependence of the polarization is defined as the electric susceptibility χ_E : [2.67]

$$\chi_E = \frac{\partial P}{\partial E} \quad (2.12)$$

Microscopically, the ferroelectric polarization in the materials investigated in this thesis (lead zirconium titanate and barium titanate) is caused by the displacement \mathbf{x}_i of lattice ions bearing the electric charge q_i . The total dipole moment for N displaced ions thus is given by

$$p = \sum_{i=1}^N X_i q_i \quad (2.13)$$

and one speaks of displacement polarization. In ferroelectric materials, polarization thus will always be accompanied by a deformation of the unit cells, which immediately leads to the conclusion that for a ferroelectric material the unit cell has a higher symmetry in its paraelectric state than in its ferroelectric state.

2.4 Spinel Structure of Ferrite

Ferrite material is so much popular as spinel compound. Spinel phase crystallizes into the cubic system with octahedral crystal formation. There are at least 30 oxides of minerals which included in the spinel super-group. The majority of spinel compounds has space group $Fd3m$. The primary member of the group has the general formula, $\mathbf{A}^{2+}\mathbf{B}^{+3}_2\mathbf{O}_4$ [2.69]; wherein:

- “**A**” stands for divalent transition metal ion such as Mn, Co, Ni, Cu and Zn, or Mg and Cd. The symbol A might be a combination of ions that has an average valency of +2 e.g. Li^{1+} and Fe^{3+} in lithium ferrite, $\text{Li}_{0.5}\text{Fe}_{2.5}\text{O}_4$. Ionic radius of approximately 0.6 - 1.0 Å.
- “**B**” stands for trivalent metal ions such as Al, Fe, Cr, etc. The trivalent iron ions (Fe^{3+}) can be completely or partially substituted by other trivalent metal ion like Al^{3+} or Cr^{3+} , resulting in a mixed crystals with aluminates or chromites.

Because of having the combination of two different types of ions, the structure refers to point out as spinel. Normal spinel structures are usually cubic close-packed oxides with one octahedral and two tetrahedral sites per formula unit. The tetrahedral spaces are smaller than the octahedral spaces. B^{3+} ions occupy half the octahedral holes, while A^{2+} ions occupy one-eighth of the tetrahedral holes.

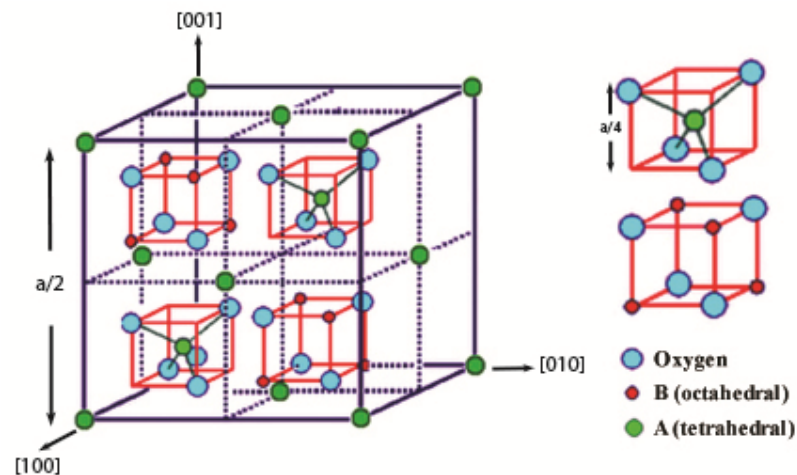


Figure 2.12: Schematic of partial unit cell [2.69]

2.4.1 Tetrahedral Site

- 8 A-sites metal ions in tetrahedral site coordination with oxygen,
- Tetrahedral site, the interstitial is at the center of a tetrahedron formed by the four lattice atoms.
- Three adjacent atoms are in a plane; the fourth atom is located at the top symmetrical position.
- The tetrahedral site defined geometry provides a space for an interstitial atom.

2.4.2 Octahedral Site

- 16 B-sites demonstrates octahedral site
- An interstitial atom at the space in the interstices between 6 atoms forming regular octahedron.
- Four regular atoms are positioned in a single plane; the remaining two are located at symmetrical positions just above or below.

For a total of 56 atoms, there are 96 interstices between the anions in the cubic lattice; but in spinel ferrites, only 24 are occupied by cations. Out of the 64 tetrahedral interstices between the anions, only 8 are occupied by the cations. The rest of 16 cations occupied half of the 32 octahedral interstices. Consequently, there are 8 formula units per cubic unit cell [2.71].

Table 2.4 Metal ion arrangements in spinel ferrite unit cell with composition (MO.Fe₂O₃) [2.70]

Types of interstitial site	Number available	Number occupied	Normal spinel	Inverse spinel
Octahedral	64	8	8M ²⁺	8Fe ³⁺
Tetrahedral	32	16	16Fe ³⁺	8Fe ³⁺ 8M ²⁺

In spinel oxide, normally the different cations do not have a big difference in size, because the spinel structure is stable only if the cations have rather medium size and in addition, the ionic radii of the different metal species in the same compound are comparable and do not differ too much. Similar cation combinations are presented in sulphides e.g. Zn²⁺Al₂³⁺S₄ and Cu₂²⁺Sn⁴⁺S₄.

However, in such spinels halide e.g. Li₂¹⁺Ni³⁺F₄ and Li¹⁺Mn₂^{3+/4+}O₄, cations are limited to valance state of +1 and +2, in order to exhibit an overall cation: anion ratio of 3: 4. The position of the “A” ions is almost identical to those occupied by the carbon atoms in the diamond structure. This could explain the relatively good hardness and high density of this typical group. More than one hundred compounds of spinel structure reported to date. Most of them are oxides, some are sulphides, selenides and telluride and few are halides. A large variety of cations might be introduced into the spinel structure and different charge combinations are possible; almost any combination that has eight positive charges to balance eight anionic

charges, for example, $\text{Mg}^{2+}\text{Fe}_2^{3+}\text{O}_4$, $\text{Mg}^{2+}\text{Al}_2^{3+}\text{O}_4$, $\text{Mg}_2^{2+}\text{Ti}^{4+}\text{O}_4$, $\text{Li}^{1+}\text{Al}^{3+}\text{Ti}^{4+}\text{O}_4$, $\text{Li}_{0.5}^{1+}\text{Al}_{2.5}^{3+}\text{O}_4$, and $\text{Na}_2^{1+}\text{W}^{6+}\text{O}_4$ etc.

The factors affecting the cation distribution over A- and B-sites are as follows [2.72 - 2.73]:

- Ionic size of cations
- Electromagnetic configuration of the cations
- Electronic energy

Smaller cations prefer to occupy the A-sites. The cations have special preference for A and B-sites and the preference depend upon the following factors:

- Ionic radius
- Size of interstices
- Temperature
- Orbital preference for the specific coordination

The preference of cations is according to Verwey-Heilmann scheme given in the Table 2.5 [2.74 - 2.75]:

Table: 2.5 Site preferences of metallic ions

Ions having a preference for A-sites	Ions having a preference for B-sites	Ions having no specific site preference
Zn^{2+}	Ni^{2+}	Mg^{2+}
Cd^{2+}	Cr^{3+}	Mn^{2+}
Ga^{2+}	Ti^{4+}	Cu^{2+}
In^{3+}	Sn^{4+}	Fe^{2+}
Ge^{4+}		Fe^{3+}
Li^{+}		Al^{3+}

2.5 Magnetism

2.5.1 Ferromagnetism

To understand the mechanism behind ferroelectricity and multiferroicity, it is prudent to revisit the primary ferroic order with which most are more familiar: ferromagnetism. A material is said to be ferromagnetic if:

- a spontaneous magnetic moment is created in the material by exposing it to an external magnetic field and

- this magnetic moment can be switched by reversing the external field [2.76].

In general, magnetism is caused by the quantum mechanical spin of electrons in the material. Materials which align these spins across large domains in response to external magnetic fields are said to be ferromagnetic. The most common examples of ferromagnetic materials are transition metals which have partially filled electron shells, such as iron, cobalt, and nickel—but there are also examples of organic compounds with these properties [2.77]. Current technologies which use ferromagnetic materials include electric motors, generators, and magnetic storage devices such as hard disks.

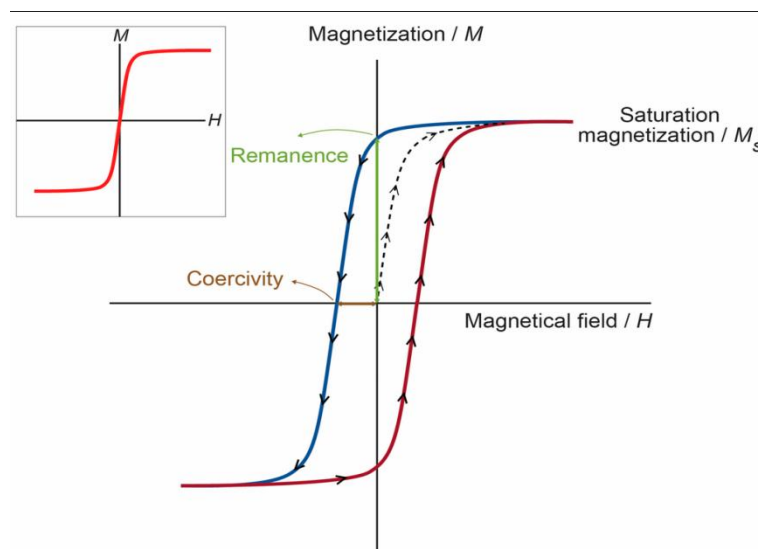


Figure 2.13: Magnetic hysteresis loop

In ferromagnets, the order parameter is the magnetization \mathbf{M} , which is defined as the magnetic moment μ per unit volume V .

$$\mathbf{M} = \frac{d\mu}{dV} \quad (2.14)$$

The magnetic moment μ , is microscopically caused by the classical orbital angular momentum \mathbf{L} of an electron in the atomic shell as well as its spin \mathbf{S} , resulting in

$$\mu = \mu_B (\mathbf{L} + g_e \mathbf{S}) \quad (2.15)$$

with the Bohr magneton μ_B and the Lande factor g_e of the electron. Quantum mechanical exchange interaction results in the parallel orientation of magnetic moments in ferromagnets, thus ferromagnetism is a quantum mechanical phenomenon. In this work, magnetic fields will be described by the magnetic induction $\mathbf{B} = \mu_0 \mathbf{H}$, \mathbf{M} is related to \mathbf{B} by

$$\mathbf{B} = \mu_0 (\mathbf{H} + \mathbf{M}) \quad (2.16)$$

In ferromagnetic materials, the relation between the magnetic field intensity \mathbf{H} and the magnetization \mathbf{M} is non-linear because of hysteresis as shown in Figure 2.1(b). In Equation (2.6) this relation was shown to be

$$\frac{\partial F}{\partial M} = B = \mu_0 H \quad (2.17)$$

which is obviously only valid if the vector properties of \mathbf{M} and \mathbf{H} are disregarded, which can only be done if \mathbf{M} and \mathbf{H} are parallel. The magnetic field dependence of the magnetization is referred to as the magnetic susceptibility χ_M :

$$\chi_M = \frac{\partial F}{\partial M} \quad (2.18)$$

If one now is interested in the equilibrium orientation of \mathbf{M} rather than just its magnitude and wants to consider the more general case of \mathbf{M} and \mathbf{H} not being necessarily parallel, \mathbf{M} as well as \mathbf{H} need to be parameterized in a suitable way by choosing an appropriate coordinate system and representation of \mathbf{M} and \mathbf{H} as a function of the chosen parameters. The most popular format of ferromagnetic materials is AB_2O_4 .

2.5.2 Antiferromagnetism

Antiferromagnetic material aligns the magnetic moments in a way that all moments are anti-parallel to each other, the net moment is zero. The inverse susceptibility as a function of temperature is shown in Figure 2.14. Common examples of materials with antiferromagnetic ordering include MnO, FeO, CoO and NiO [2.78].

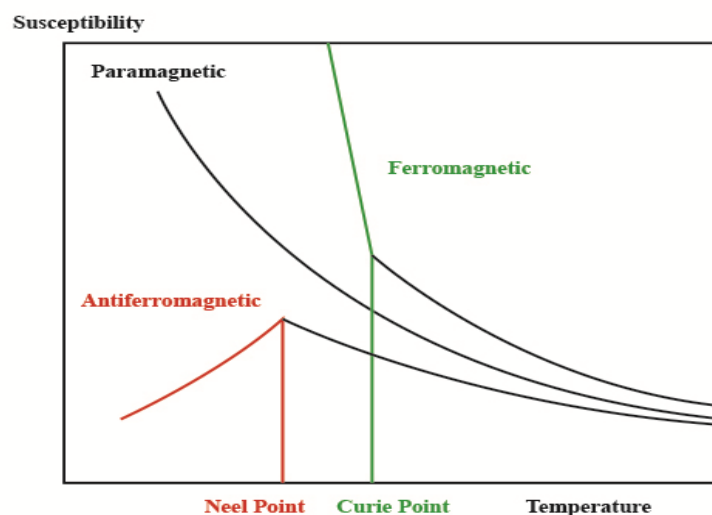


Figure 2.14: Variation of magnetic object due to different temperature

2.6 Multiferroicity

When any combination of the primary ferroic orders exists within the same material, it is said the material displays multiferroic properties. The relationship between ferroelectricity and ferromagnetism in terms of multiferroicity is shown in Figure 2.15. Along with the above mentioned primary ferroic orders, two others also exist [2.79], ferroelasticity and ferrotoroidicity, which are only included here for completeness and are not investigated in the scope of this thesis. Although multiferroic materials are known to exist, this property is not utilized in any current applications. It is predicted that multiferroicity could be utilized in high sensitivity magnetic field sensors [2.80], multiple state memory elements [2.81], and electrically tunable spin valves [2.80].

Unfortunately, materials combining ferromagnetic and ferroelectric properties {such as HoMnO_3 } are very rare and do not show robust multiferroic properties at room temperature [2.82]. However, materials showing magnetoelectric coupling are of great interest, as they would allow for an electric field control of magnetization that may be used in magnetoresistive random access memory or other devices utilizing magnetoresistive effects. Robust room temperature multiferroic properties are found in heterostructures consisting of separate ferromagnetic and ferroelectric phases, which allows for an electric field control of magnetization. In this thesis, multiferroic heterostructures consisting of a ferromagnetic thin film and a ferroelectric substrate are investigated. This allows us to determine the interaction between the different ferroic properties.

Single phase multiferroics are categorized in type I and type II. Type I single phase multiferroic (e.g. YMnO_3) is referred as independent properties of ferroelectric and magnetic orders which infrequently show the parameters above room temperature. The coupling between ferroelectric and ferromagnetic moments is inherently weak and the contribution of ME properties is not large in compared with requirement. The imbalance between electron spin states and electron orbit coupling are responsible for the magnetic order. BiFeO_3 is known as one of type I single phase multiferroic. In contrast type II multiferroic the ferroelectric polarization may be instigated from special types of magnetic spiral or collinear magnetic structure (e.g. TbMnO_3 , $\text{Ca}_3\text{CoMnO}_6$). It is true for both type of multiferroics that the sharing of magnetic parameters give rise to a net polarization at low temperatures, which

contributing on forward coupling of the ferroic order parameters [2.83 - 2.84]. Interaction of ferroic orders due to define coupling has been given few magnetic field control of ferroelectric polarization. So it is seen that, the Type-I multiferroic has high T_C and polarization are better in strong but the ME coupling is too small whereas in Type-II multiferroic the coupling is strong but T_C is low. So multiferroic composite could be considered as better solution to obtain strong ME coupling.

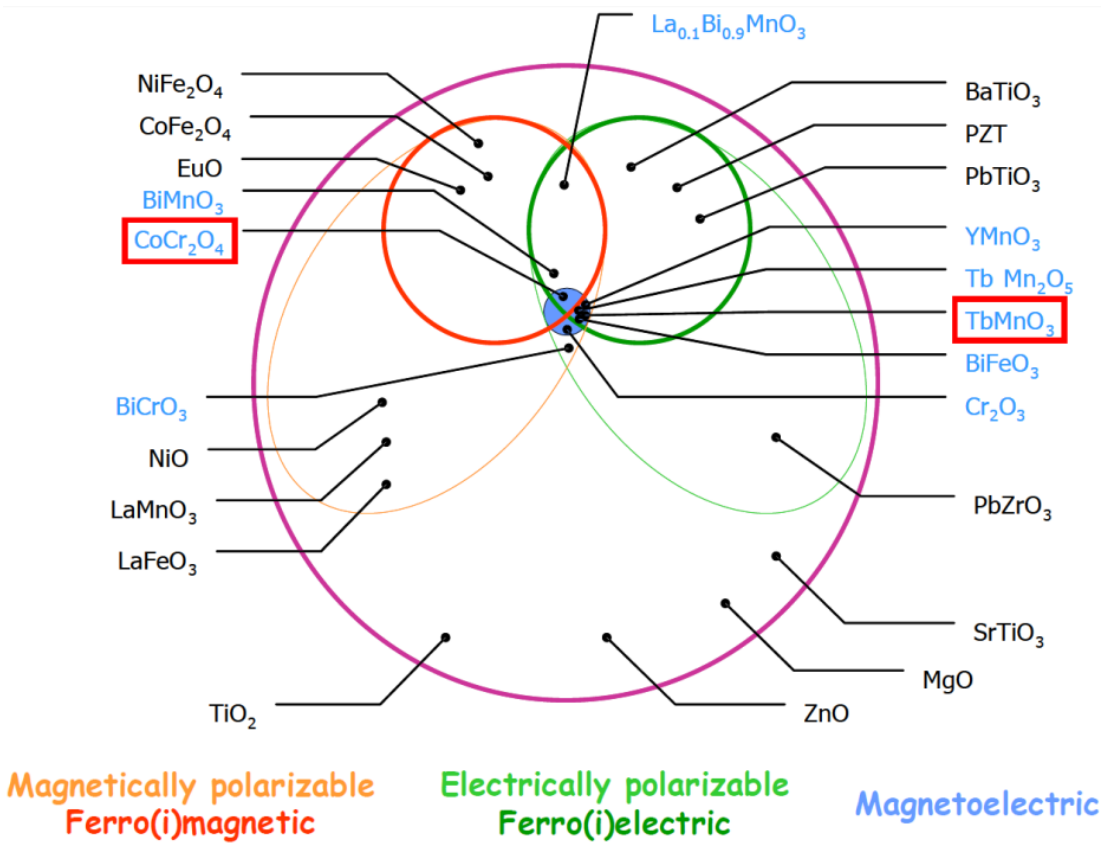
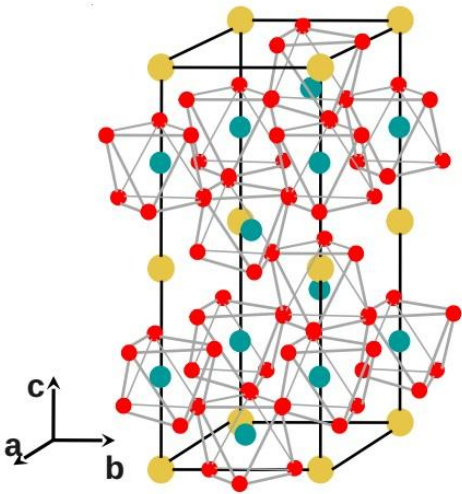
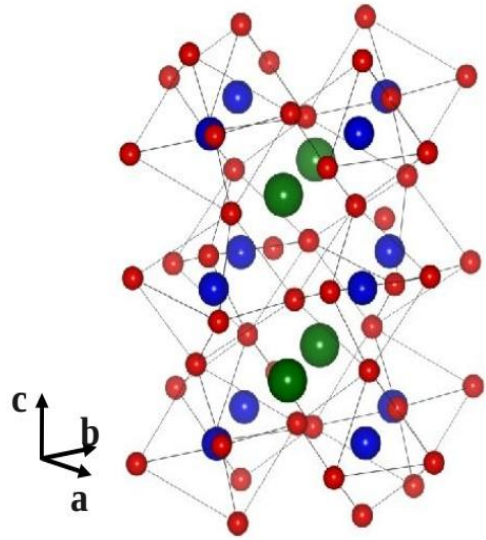


Figure 2.15 The ‘world of electrically and magnetically polarizable materials’ including bare ferroics, multiferroics and linear magnetoelectrics

Table 2.6 shows that, correlation and dissimilarities between different ferroic ordered parameters

Table-2.6: Similarities and dissimilarities between two types of Multiferroics

Type	Multiferroics type I	Multiferroics type II
Dependency	Ferroelectricity and magnetism have different sources and are independent	Magnetic order causes ferroelectricity and therefore giant magnetoelectric effect
Ferroelectricity	Strong ferroelectrics and ferroelectricity at higher T than magnetism	Weak ferroelectrics and ferroelectricity in low-temperature system
Temperature effect	Order temperatures close to room temperature.	Low order temperatures
Coupling	Weak and indirect coupling between orders at different transition temperatures	Ferroelectricity and magnetism are direct strongly coupled
Example	BiFeO_3	Perovskites RMnO_3 : Tb, Gd, Dy TbMnO_3
Structure		

EXPERIMENTAL PROCEDURE

3.1 Methodology of Nanostructured Multiferroic Composites Preparation

To synthesis nano particle is not easy task because of controlling particle size that is much complex and durable work. Less than 100nm is considered as nano particle [3.1]. Nanoparticles attract prodigious scientific attention for efficiently made a connection among bulk materials and atomic or molecular structures. A bulk material ought to have constant physical properties irrespective of its size, but at the nano-scale this is habitually not the event. Size-dependent properties are perceived such as quantum confinement in semiconductor particles, surface plasmon resonance in some metal particles and superparamagnetism in magnetic materials. Ferroelectric materials smaller than 10 nm can switch their magnetization direction using room temperature thermal energy, thus making them useless for memory storage [3.2]. Nanoparticles often have unexpected visible properties because they are small enough to confine their electrons and produce quantum effects. For example, gold nanoparticles appear deep red to black in solution [3.3]. Nanoparticles have a very high surface area to volume ratio [3.4]. The large surface area to volume ratio also reduces the incipient melting temperature of nanoparticles. This provides a tremendous driving force for diffusion, especially at elevated temperatures. Sintering can take place at lower temperatures, over shorter time scales than for larger particles.

3.1.1 Aspects of Present Work

In this research work, oxide materials in powdered form had considered to take in account to obtain multiferroic composites. In general, it is not familiar to synthesis nano particles by using oxide materials. Nano materials are size dependent so the changing on size of particles dominates the fundamental physical properties. The parameters of nano particles are realtive size distribution, density control, diffusion rate which could be designed by synthesis mechanism. The typical synthesis mechanisms are Laser ablation, Exploding wire, Arc, Flame pyrolysis, Combustion, Precipitation synthesis techniques. To use oxide materials there has no familiar and cost effective technique to synthesis nano particle. From this motivation conventional ceramic method and some mechanical approaches with advance tools which able to

disperse particle from its neighboring particle that helps to confine nano sized particle have been used. Conventional ceramic method is used to mix the powder where magnetic stirring, ultrasoification and centrifuge are used to disperse and wash it.

3.1.2 Problems with conventional Methods

The raw materials in generating chemical precipitation and sol gel methods are so expensive. In solid state reaction method, the milling is a good job to mix the raw materials but to minimize the size of particle, it not may better system. Solid state reaction method is ‘top to bottom’ mechanism but the mechanical approach which is need in reducing particle size that helps to confine nano particle does not much effective. But the ‘bottom to top’ approaches like sol-gel, conventional reaction methods etc are used in obtaining nano particle where the problem is that the raw materials should have been in acidic and alkali form which may react with each other during chemical reaction and provide nano sized particles.

3.1.3 Reason of using oxide materials

Metallic oxides are most cost effective and available material that has been using in many purposes of scientific work. Unfortunately, to obtain nano particle by using metallic oxide is not simplified from the view of synthesis mechanism. If it will possible to obtain nano particle by using oxide materials where no chemical reaction is needed, then it will be a great achievement in nanotechnology. This research has been illustrated with some mechanical approaches that will may helpful to reduce the particle size. Solid-state reaction method is used for homogeneous mixture and magnetic stirring, ultrasonification, centrifuge is used to disperse and wash the particle. It is expected that these mechanical approaches will affect in minimizing particle size.

3.1.4 Selection of Raw Materials

As discussed in previous chapters it already mentioned that, this research work is designed to synthesis multiferroic composites. So it is very important to select novel ferroelectric and ferromagnetic materials which will satisfy the target of this research. Bismuth ferrite (BFO) is highly popular as ferroelectric active material where small addition of Lanthanum improves the ferroelectricity. Likewise Nickel Zinc is well established ferromagnetic materials and the addition of small amount of

Vanadium improves its transparent properties by reducing melting temperature. It should be noted that the melting temperature of BFO is low so it is very important to minimize the melting temperature of NZFO by adding little bit refractory materials like Vanadium, Niobium, Chromium etc which is convenient in generating multiferroic composites. This BLFO and NZVFO materials are combined to form composites by following the steps described below.

3.1.5 Weighing the raw materials at precise ratio

All oxide samples had collected with 99.99% purity and samples used are from Merck Aldrich and Sigma Company. The raw materials were weighted in exact ratio in digital weight meter as calculated in Table 3.1. There had no chance to mix additional pollutants in raw samples from environment because high sensitivity and care was taken to measure the materials. To produce the desire nano composites it is very important to select the materials that have all the phenomenological characteristics. The choice of reactant chemicals depends on the reaction conditions and expected nature of the product. The reactants had dried thoroughly prior to weighing. As increase in surface area enhances the reaction rate, fine-grained materials should use if possible. The weight percentage of the oxide to mixed for various samples was calculated by using formula:

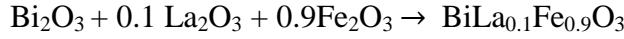
$$\text{Weight \% of oxide} = \frac{M.wt \cdot \text{of oxide} \times \text{required weight of the sample}}{\text{Sum of Mol.wt.of each oxide in a sample}}$$

The chosen materials are Bi_2O_3 , La_2O_3 , Fe_2O_3 , NiO , ZnO and V_2O_5 . Among of the materials except NiO and ZnO other were in two moles by default in chemical formula. However, according to the weight % of oxide materials it is very important to take one mole from these which would confirm the exact ratio.

3.2. Mixed and milled the samples (Hand Milling)

From ancient era, handmade tools are the art of synthesis materials because its whole system controlled and operated by human. Milling is one of great and novel technique to mix the raw materials. Dry powder materials have not sufficient moisture to mix so to make it wet the addition of acetone improves the mixing mechanism as high-quality wet ingredient. Milling time is very important to well mixing of the materials. Greater milling time gives high quality mixing. The calculation of sample preparation is given in below:

For BLFO



For NZVFO

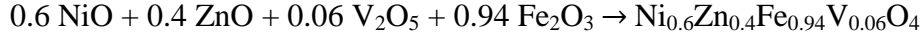


Table 3.1: Detail calculation of materials used in this research

For BiFe_{0.9}La_{0.1}O₃						
Content	Atomic Mass (gm)	In 1 Mole	Content	Atomic Mass (gm)	In 30 gm of the sample	Atomic Mass (gm)
Bi ₂ O ₃	465.95896	232.97948	Bi ₂ O ₃	232.97948	Bi ₂ O ₃	21.76499
Fe ₂ O ₃	159.6882	79.8441	0.90Fe ₂ O ₃	71.85969	0.90Fe ₂ O ₃	6.713148
La ₂ O ₃	325.8092	162.9046	0.10La ₂ O ₃	16.29046	0.10La ₂ O ₃	1.521858
Total	951.45636	475.72818	Total	321.12963	Total	30
For Ni_{0.6}Zn_{0.4}Fe_{0.94}V_{0.06}O₄						
NiO	74.6928	74.6928	0.60NiO	44.81568	0.60NiO	8.51592
ZnO	81.3794	81.3794	0.40ZnO	32.55176	0.40ZnO	6.185518
Fe ₂ O ₃	159.6882	79.8441	0.94Fe ₂ O ₃	75.053454	0.94Fe ₂ O ₃	14.26173
V ₂ O ₅	181.88	90.94	0.06V ₂ O ₅	5.4564	0.06V ₂ O ₅	1.036831
Total	497.6404	326.8563	Total	157.87729	Total	30

3.2.1 Stirred the samples in magnetic stirring hot pot

Magnetic stirrers (also known as magnetic stir plates) are very common in experimental chemistry and biology. It is used to mix components (solids and liquids) to get homogeneous liquid mixtures. To mix the composites powder sample, magnetic stirring is an incredible tool. Magnetic stirrers mix solutions using an external magnetic field that rotates a small magnetic bar that has been placed in the mixture of interest. Due to its small size, a stirring bar is more easily cleaned and sterilized than other stirring devices. Magnetic stirrers avoid two major problems with motorized stirrers. Firstly, motorized stirrers use lubricants, which can contaminate the reaction vessel and the product. Secondly, in motorized stirrers, the sealing of the connection between the rotating shaft of the stirrer and the vessel can be problematic, especially if a closed system is needed.

Magnetic stirrers minimize the risks of contamination since only an inert magnet bar, which can easily be cleaned, is putted inside the sample/fluid. In addition, using a magnetic stirrer rather than manual stirring is critical for consistent, reproducible mixing or mixing over long time scales. Protein dialysis, for example, requires multi-hour or overnight sample mixing and is sensitive to external contamination.



Figure 3.1: Magnetic stirring with hot pot and beaker and magnetic bars in different size

By dispersion, it refers here that the nanoparticles do not precipitate, even after a very long time, and that the liquid is completely clear, with a particle size between 5 and 40 nm. To make a homogeneous mixture, for example, of BLFO and NZVFO powders, it is not possible to see how further stirring can have an effect on mass transport on the size scale of the reactants. The portions of liquid that are moved about relative to each other are much larger than the particles, so that the individual particles will not "feel" the stirring.

In the laboratory of Atomic Energy Centre, Dhaka, the magnetic stirring was used. As mixing substance, highly purred acetone and di-ionized water were used. In the beginning, a series of composite was placed in a beaker and 30 ml acetone was added to it. Then the beaker was placed on the round hot plate of magnetic stirring though it was operated at room temperature because the raw materials had no need to make chemical reaction. 360 rpm was fixed for 3 hours to mix the raw materials. After ending this stage, the samples had washed in deionized water and again stirred for 5 minutes in deionized water. The dispersion of particle from its neighbored particle is very essential to obtain nano material, which was made by using magnetic

stirring. The rotation of magnetic bar had gave mechanical force which was enabled the dispersion of particles.

3.2.2 Further dispersion was made by using Ultrasonification

Ultrasonic cleaning is a process that uses ultrasound (usually from 20–400 kHz) and an appropriate cleaning solvent (sometimes-ordinary tap water) to clean items. The ultrasound can be used with just water, but use of a solvent appropriate for the item to be cleaned and the type of soiling present enhances the effect. Cleaning normally lasts between three and six minutes, but can exceed 20 minutes, depending on the object to be cleaned [3.5]. In powder metallurgy, ultrasonic dispersion is very effective instrument to separate particles from its neighbor particles that make sure to understand the behavior of individual particles.

The Decon FS Minor ultrasound signification bath had used for this research work in Atomic Energy Centre, Dhaka. It has a water chamber that must not be blanked or filled of water but certain level of water was used. A beaker with samples dissolved in deionized water had putted on the water bath for 10 minutes. After this session, the water was removed and it was expected that the samples was clean with better treatment of ultrasonic dispersion.



Figure 3.2: Ultrasonic cleaner showing the removable basket in place, and a close up of the light and timer

3.2.3 Centrifugation

A centrifuge is a device considered to take apart weighty material from light material. When the material is a very fine solid in a solution, separating parts of the mixture can be more difficult than a solid. This method is used to take apart two

mixed substances and also used to analyze hydrothermal properties of macromolecule [3.6]. Heavier contents of the solution drift away from the axis of the centrifuge, whereas less-dense contents of the solution wander towards the axis. Scientists may increase the successful gravitational force on a test tube to more rapidly and completely cause the precipitate (pellet) to gather on the bottom of the tube.

There is a relationship involving the size and density of a particle and the tempo that the particle disconnects from a heterogeneous mixture, when the only force applied is that of gravity. The larger the size and the larger the density of the particles, the faster they separate from the mixture. By applying a larger effective gravitational force to the mixture, as a centrifuge does, the separation of the particles is accelerated.

The rate of centrifugation is specified by the angular velocity usually expressed as revolutions per minute (RPM), or acceleration expressed as g . The conversion factor between RPM and g depends on the radius of the centrifuge rotor. Although RPM is commonly used for setting centrifuge speeds, a more accurate measurement is actually called RCF or relative centrifugal force [3.7]. RCF is independent of the radius between the center of the centrifuge and the holes for the samples. In this experiment the rpm was 3000. The general formula for calculating the revolutions per minute (RPM) of a centrifuge is

$$\text{RPM} = \sqrt{\frac{g}{r}} \quad (3.1)$$

where g represents the respective force of the centrifuge and r the radius from the center of the rotor to a point in the sample [3.8].

The centrifuge in Atomic Energy Centre, Dhaka, the centrifuge is from Abbota Centrifuge where 4 chambers are available to use tubes. To use this centrifuge, a test tube had putted on the slot. However, it is very important that the centrifuge should be balanced to put tubes at least in opposite two slots. If the centrifuge is not balanced the centrifuge will be unstable, and it will not spin at the right speed! When there had one tube in operation with sample then another tube also be inputted, which was filled by water and this made balance of the centrifuge before started to run. Small differences in mass of the load can result in a large force imbalance when the rotor is at high speed.



Figure 3.3: Centrifuge used in lab with four chambers

This force imbalance strains the spindle and may result in damage to the centrifuge or personal injury. Some centrifuges have an automatic rotor imbalance detection feature, which immediately discontinues the run when an imbalance is detected. So it was carefully looked up to balance the slots by inputting two tubes in opposite side.

After balancing the centrifuge, the rpm was selected at 3000 for 10 minutes and the centrifuge was operated under this condition. To prevent accidental contact with a moving rotor as the main lid was locked during the run. It was carefully considered that, the effect of high rpm caused precipitates the samples in the bottom of the tube and the water was carrying all other impurities at the upper portion of sediment with it. After 10 minutes passed the centrifuge was automatically stopped. Then the water was removed by manually and the sediment stirred by a thin spun. To clean the samples with accuracy, the whole procedure was repeated for four times.

3.2.4 Heat Treatment

The heat treatment such as sintering has a predominant effect upon the grain growth. The reduction in the overall surface energy is the true driving force for the grain boundary enlargement and consequently the particle size increases as a function

of the temperature. Sintering is the consolidation of a powder by means of prolonged use of elevated temperatures, which are, however, below the melting point of any major phase of the material. It facilitates the movement of atoms or molecules through the mechanism of mass transport that may be lattice diffusion, surface diffusion or evaporation-condensation and results in the grain growth which has detrimental effect on the properties of the material.

After washing in centrifuge, all samples were heated at 150°C in oven for 2 hours. This heat treatment was not able to change the particle size and did not affect on phase shift because of not having higher temperature that could be changed the fundamental properties.

- Washed by dionized water in centrifuge at 3000 rpm for 10 minutes and each step repeated for 4 times
- All samples heated in 150°C for 1 hour

3.3 Converting the ferrites into powder and pressing the powder

These undesirable features of the raw ferrites are eliminated in the following two steps [3.9]:

3.3.1 Grinding

The ferrite produced via pre-sintering is usually in the lump form. In this step, it is first ground into powder in a steel ball mill. Grinding eliminates intra particle pores, homogenizes the ferrite, reduces the particle size to $\ll 1\mu\text{m}$ and promote mixing of any un-reacted oxides.

3.3.2 Pressing or Extrusion

The dry powder is mixed with an organic binder and pressed in to compacts of desired shapes either by the conventional method in a die-punch assembly or by hydrostatic or isostatic compaction. Most shapes, such as toroidal cores, are pressed (at 1-10 ton/cm², 14-140MPa), but rods and tubes are extruded.



Figure 3.4: Hydraulic press used to make different shaped samples.

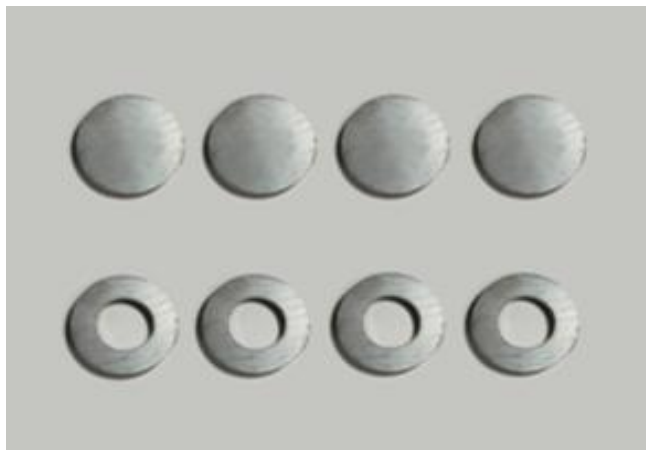


Figure 3.5: Toroid and disk shape sample.

3.4 Annealing

Thermal treatment of powder materials without pressing in different shapes is termed as annealing. Annealing is the process of holding a material at an elevated temperature to obtain (positive) changes in the micro-structure. It should refer to a treatment where neither the chemical nor the phase compositions significantly change. Chemical transformation is not involved as highlighted previously, as an example release of stress/strain in a sample type glass, ceramic. In the process of annealing a fast grain growth occurs, aggregate formation, agglomerate formation, particle

coalescence etc seems that mixture of phases will be formed. To understand the effect of temperature on particle size distribution and grain growth, the samples are annealed at 150°C, 300°C, 450°C, 600°C and 850°C. Field Emission Scanning Electron Microscope will use in determining the particle size distribution and grain growth of different annealing temperature.

3.5 Sintering

Sintering is the final and a very critical step of preparing a ferrite with optimized properties. The sintering time, temperature and the furnace atmosphere play very important role on the magnetic property of final materials. Sintering commonly refers to processes involved in the heat treatment by which a mass of compacted powder is transformed into a highly densified object by heating it in a furnace below its melting point [3.10-3.11]. Ceramic processing is based on the sintering of powder compacts rather than melting/ solidifications/cold working (characteristic for metal), because:

- (i) Ceramics melt at high temperatures
- (ii) As solidified microstructures cannot be modified through additional plastic deformation and re-crystallization due to brittleness of ceramics
- (iii) The resulting coarse grains would act as fracture initiation sites
- (iv) Low thermal conductivities of ceramics ($< 30 - 50 \text{ W/ mK}$) in contract to high thermal conductivity of metals (in the range $50 - 300 \text{ W / mK}$) cause large temperature gradients, and thus thermal stress and shock in melting-solidification of ceramics.

Sintering is the bonding together of a porous aggregate of particles at high temperature. The thermodynamic driving force is the reduction in the specific surface area of the particles. Sintering may result in densification, depending on the predominant diffusion pathway. It is used in the fabrication of metal and ceramic components, the agglomeration of ore fines for further metallurgical processing and occurs during the formation of sandstones and glaciers. Sintering must fulfill three requirements [3.12]:

- (i) to bond the particles together so as to impart sufficient strength to the product
- (ii) to densify the grain compacts by eliminating the pores and
- (iii) to complete the reactions left unfinished in the pre-sintering step

The theory of heat treatment is based on the principle that when a material has been heated above a certain temperature, it undergoes a structural adjustment or stabilization when cooled at room temperature. The cooling rate plays an important role on which the structural modification is mainly based. Figure 3.6 shows the flow chart of the sample preparation.

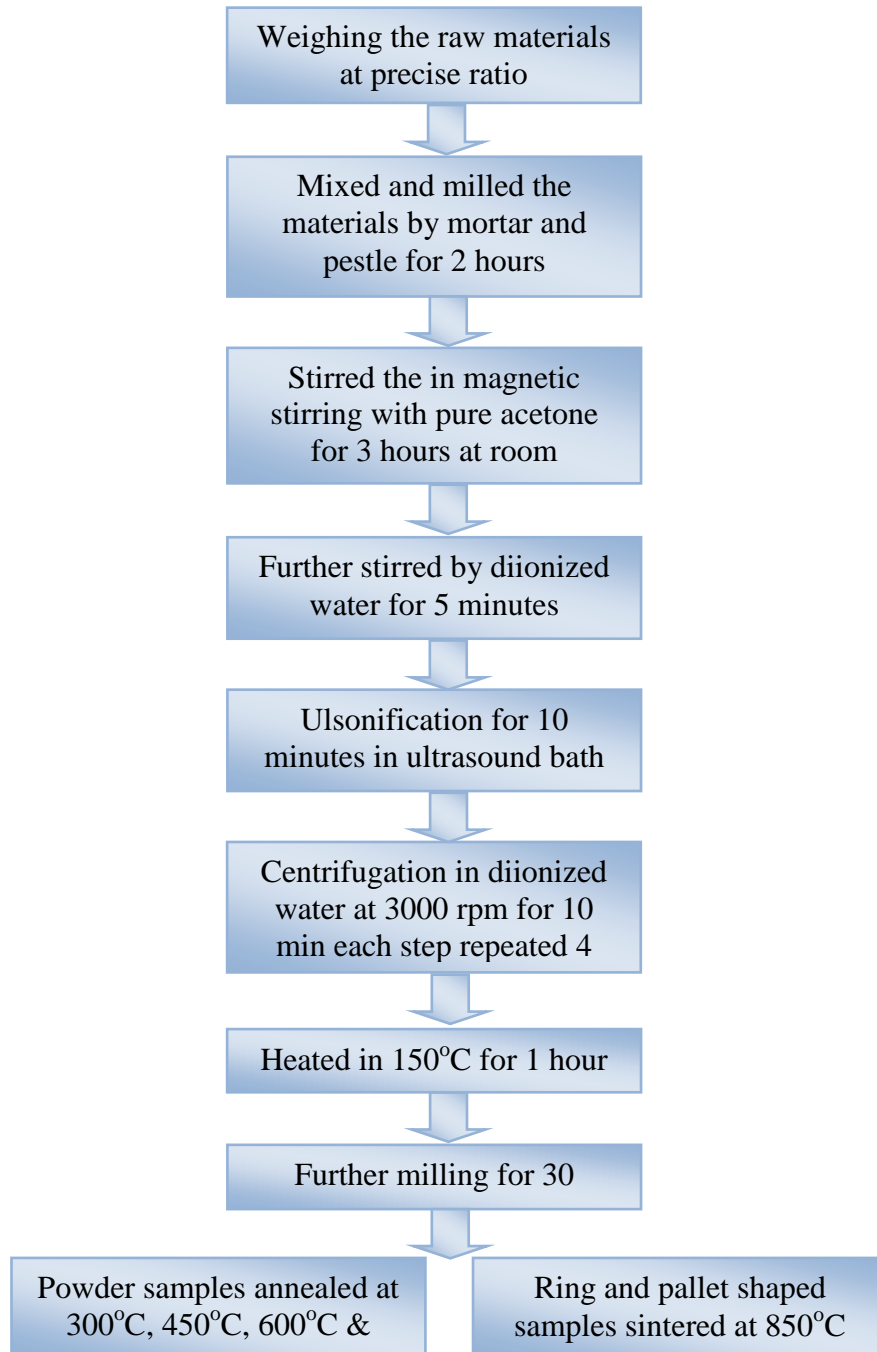


Figure 3.6: Flow chart of the sample preparation

3.6 X-ray Diffraction (XRD)

X-rays are the electromagnetic waves whose wavelength is in the neighborhood of 1\AA . The wavelength of an X-ray is that the same order of magnitude as the lattice constant of crystals and it is this which makes X-ray so useful in structural analysis of crystals. X-ray diffraction (XRD) provides precise knowledge of the lattice parameter as well as the substantial information on the crystal structure of the material under study.

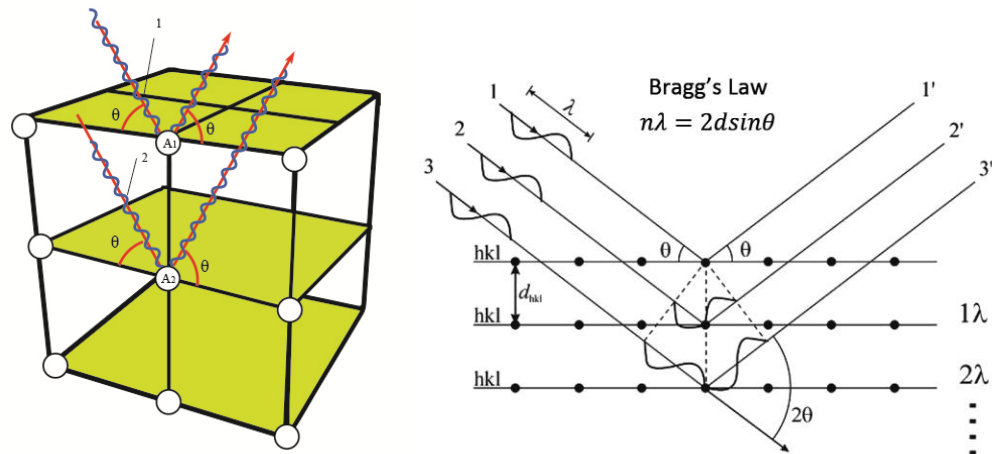


Figure 3.7: Incident rays (1 and 2) at angle θ on the planes of atoms in a crystal. Rays reinforce if their difference in path length ($AB + BC$) is an integer times the wavelength of the X ray.

X-ray diffraction is a versatile nondestructive analytical technique for identification and quantitative determination of various crystalline phases of powder or solid sample of any compound. When X-ray beam is incident on a material, the photons primarily interact with the electrons in atoms and get scattered. Diffracted waves from different atoms can interfere with each other and the resultant intensity distribution is strongly modulated by this interaction. If the atoms are arranged in a periodic fashion, as in crystals, the diffracted waves will consist of sharp interference maxima (peaks) with the same symmetry as in the distribution of atoms. Measuring the diffraction pattern therefore allows us to deduce the distribution of atoms in a material. It is to be noted here that, in diffraction experiments, only X-rays diffracted via elastic scattering are measured [3.13].

The peaks in an X-ray diffraction pattern are directly related to the atomic distance. Let us consider an incident X-ray beam interacting with the atoms arranged in a

periodic manner as shown in two dimensions in Fig. 3.7. The atoms, represented as spheres in the illustration, can be viewed as forming different sets of planes in the crystal [3.14].

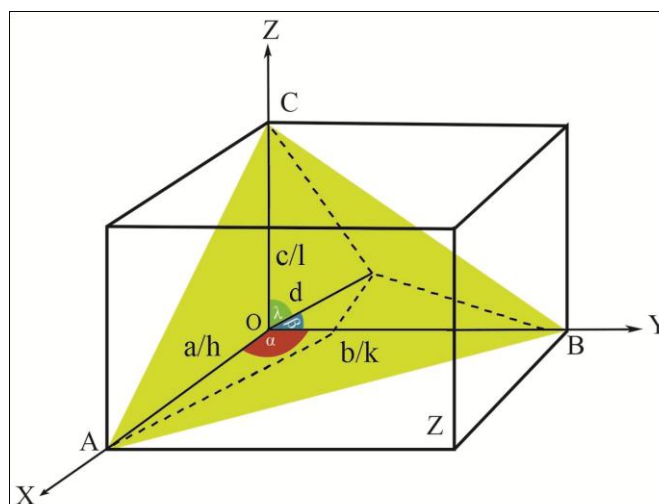


Figure 3.8: Crystal plane orientation

3.6.1 Derivation of Bragg's Law

Bragg's Law can be derived using simple geometry by considering the distances traveled by two parallel X-rays reflecting from adjacent planes. The X-ray hitting the lower plane must travel the extra distance AB and BC (fig.4.2). To remain in phase with the first X-ray, this distance must be a multiple of the wavelength thus:

$$n\lambda = AB+BC = 2AB \text{ (since the two triangles are identical)}$$

The distance AB can be expressed in terms of the interplanar spacing (d) and incident angle (θ) because d is the hypotenuse of right triangle zAB shown at right.

$$\sin(\theta) = AB/d$$

thus

$$AB = d \sin(\theta)$$

Therefore:

$$n\lambda = 2 d \sin(\theta) \tag{3.1}$$

which is known as Bragg's law. In the equation, λ is the wavelength of the X-ray, θ is the scattering angle, and n is an integer representing the order of the diffraction peak. The Bragg's Law is one of the most important laws used for interpreting X - ray diffraction data. From the law, we find that the diffraction is only possible when $\lambda < 2d$ [3.15]. In the present work, A PHILIPS PW 3040 X' pert PRO X-ray diffractometer was used for the lattice parameter to study the crystalline phases of the prepared samples in the Materials Science Division, Atomic Energy Centre, Dhaka. Fig. 3.6 shows the block diagram of X' pert XRD system.

3.6.2 Different Parts of the PHILIPS X' Pert PRO XRD System

Figure 3.9 shows the inside view of the X'-pert PRO XRD system. A complex of instruments of X-ray diffraction analysis has been established for both materials research and specimen characterization. These include facilities for studying single crystal defects, and a variety of other materials problems.

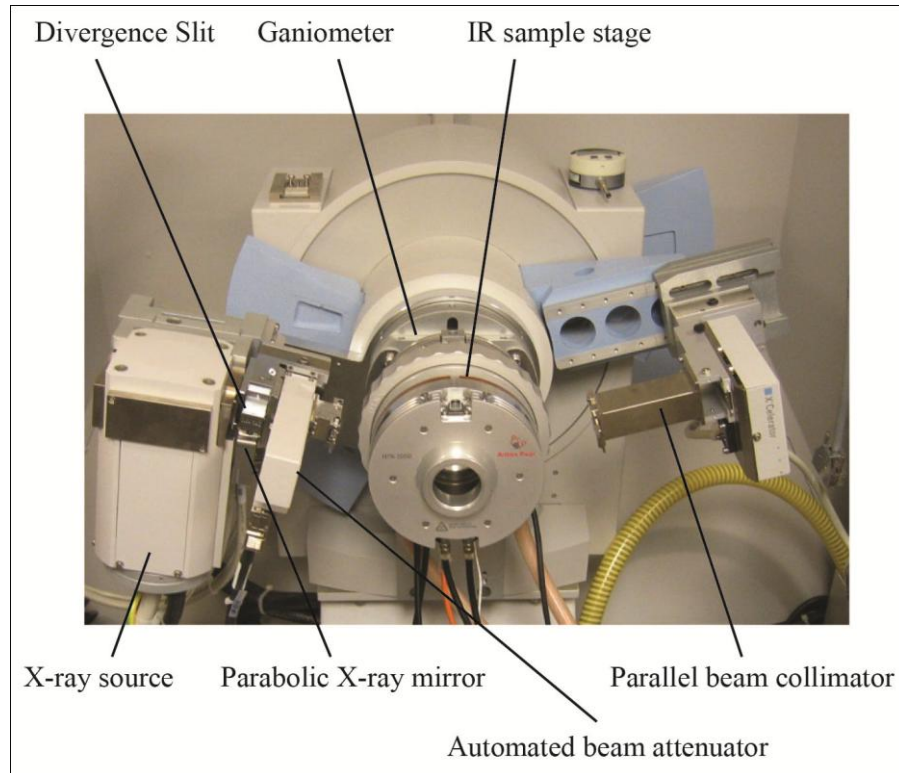


Figure 3.9: Internal arrangement of a PHILIPS X' Pert PRO X-ray diffractometer

3.6.3 Interpretation of the XRD data

The XRD data consisting of θ_{hkl} and d_{hkl} values corresponding to the different crystallographic planes are used to determine the structural information of the samples like lattice parameter and constituent phase. Lattice parameters of Co-ferrites samples were determined. Normally, lattice parameter of an alloy composition is determined by the Debye-Scherrer method after extrapolation of the curve. We determine the lattice spacing (interplaner distance), d using these reflections from the equation which is known as Bragg's Law.

$$2d_{hkl} \sin\theta = \lambda \quad \text{i.e. } d_{hkl} = \frac{\lambda}{2\sin\theta} \quad (3.2)$$

where λ is the wavelength of the X-ray, θ is the diffraction angle and n is an integer representing the order of the diffraction. Again from the figure 3.8 it is shown that

$$\cos^2\alpha + \cos^2\beta + \cos^2\gamma = 1 \quad (3.3)$$

Also $\angle ONA = \angle ONB = \angle ONC = 90^\circ$

Now $\triangle AON$ is a right angle triangle with $\angle AON = \alpha$ and $\angle ONA = 90^\circ$

$$\therefore \frac{ON}{Oa} = \cos\alpha \Rightarrow ON = Oa \cos\alpha$$

$$\text{or } d = \frac{a}{h} \cos\alpha \Rightarrow \cos\alpha = d \frac{h}{a}$$

$$\text{Similarly } \cos\beta = d \frac{k}{b} \text{ and } \cos\gamma = d \frac{l}{c}$$

Now substitute the values into equation i we get

$$d^2 \left[\frac{h^2}{a^2} + \frac{k^2}{b^2} + \frac{l^2}{c^2} \right] = 1 \quad \text{or} \quad d^2 = \frac{1}{\left[\frac{h^2}{a^2} + \frac{k^2}{b^2} + \frac{l^2}{c^2} \right]}$$

for cubic lattice $a = b = c$

$$\text{So we have } d = \frac{a}{\sqrt{h^2+k^2+l^2}} \quad (3.4)$$

where h, k, l are the indices of the crystal planes. We get d_{hkl} values from the computer using software “X’- Pert HJGHS CORE”. So we got ten ‘a’ values for ten reflection planes such as a_1, a_2, a_3, \dots etc. Determine the exact lattice parameter for each sample, through the Nelson-Riley extrapolation method. The values of the lattice parameter obtained from each reflected plane are plotted against Nelson-Riley function [3.16]. The Nelson-Riley function $F(\theta)$, can be written as

$$F(\theta) = \frac{1}{2} \left[\frac{\cos^2 \theta}{\sin \theta} + \frac{\cos^2 \theta}{\theta} \right] \quad (3.5)$$

where θ is the Bragg’s angle. Now drawing the graph of ‘a’ vs $F(\theta)$ and using linear fitting of those points will give us the lattice parameter ‘ a_0 ’. This value of ‘ a_0 ’ at $F(\theta) = 0$ or $\theta = 90^\circ$. These ‘ a_0 ’s are calculated with an error estimated to be $\pm 0.0001 \text{ \AA}$.

Rules for determining the diffracting $\{hkl\}$ planes in cubic crystals

	Reflection Present	Reflection Absent
BCC	$(h+k+l) = \text{even}$	$(h+k+l) = \text{even}$
FCC	$(h,k,l) \text{ all odd or all even}$	$(h,k,l) \text{ all odd or all even}$

3.6.4 X-ray Density and Bulk Density

X-ray density, ρ_x was also calculated usual from the lattice constant. The relation between ρ_x and ‘a’ is as follows [3.17],

$$\rho_x = \frac{ZM}{Na^3} \quad (3.6)$$

where M is the molecular weight of the corresponding composition, N is the Avogadro's number ($6.023 \times 10^{23} \text{ mole}^{-1}$), 'a' is the lattice parameter and Z is the number of molecules per unit cell, ($Z = 8$ for the spinel cubic structure). The bulk density was calculated considering a cylindrical pellet of mass (m) and volume (V) of the pellets using the relation [3.18]:

$$\rho_B = \frac{m}{V} = \frac{m}{\pi r^2 h} \quad (3.7)$$

where m is the mass of the pellet sample, r is the radius and h is the thickness of the pellet.

3.6.5 Porosity

Porosity is a parameter which is inevitable during the process of sintering of oxide materials. It is noteworthy that the physical and electromagnetic properties are strongly dependent on the porosity of the studied samples. Therefore an accurate idea of percentage of pores in a prepared sample is prerequisite for better understanding of the various properties of the studied samples to correlate the microstructure property relationship of the samples under study. The porosity of a material depends on the shape, size of grains and on the degree of their storing and packing. The difference between the bulk density ρ_B and X-ray density ρ_x gave us the measure of porosity. Percentage of porosity has been calculated using the following relation [3.19]

$$P = \left(1 - \frac{\rho_B}{\rho_x}\right) \times 100\% \quad (3.8)$$

3.6.6 Crystalline Size

The **Scherrer equation** [3.20], in X-ray diffraction and crystallography, is a formula that relates the size of sub-micrometre particles, or crystallites, in a solid to the broadening of a peak in a diffraction pattern. It is named after Paul Scherrer. It is used in the determination of size of particles of crystals in the form of powder.

The Scherrer equation can be written as:

$$D = \frac{0.9\lambda}{\beta \cos\theta} \quad (3.9)$$

Where:

- D is the mean size of the ordered (crystalline) domains, which may be smaller or equal to the grain size;
- λ is the X-ray wavelength;

- β is the line broadening at half the maximum intensity (FWHM), after subtracting the instrumental line broadening, in radians. This quantity is also sometimes denoted as $\Delta(2\theta)$;
- θ is the Bragg angle.

3.6.7 Rietveld Refinement

Rietveld Refinement is a method used to determine detailed information of crystalline materials. In order to get authentic information about crystalline materials, the least square value of the difference between theoretical and experimental peak intensities are supposed to be minimized based on releasing and refining appropriate parameters, as shown below in equation (3.10). In Rietveld analysis, the difference between experimental and theoretical as well as simulated data is minimized which provide the actual refinement of XRD. This minimization is obtained in association with three dependable index parameters which are known as discrepancy factor (R_{wp}), expected value (R_{exp}) and goodness of fit index (χ^2) [3.21-3.22]

$$R_{wp} = \left[\left(\sum_i w_i (I_o - I_c)^2 \right) / \left(\sum_i w_i I_o^2 \right) \right]^{1/2}$$

$$R_{exp} = \left[\left(\sum_i (N - P) \right) / \left(\sum_i w_i I_o^2 \right) \right]^{1/2}$$

$$\chi^2 = [R_{wp} / R_{exp}]^2 \quad (3.10)$$

where I_o and I_c are the experimental and calculated intensities, $w_i = (1/I_o)$ and N are the weight and number of experimental observations and P is the number of fitting parameters. These values are used in refining lattice parameter for both of perovskite and ferrite sites. For composite sample, Rietveld refinement is not only a tough job but also to obtain optimum values with fine fitting between experimental and theoretical data is durable. So in the case of composite, two phase model is used to find out space groups for both of constituent phases. Equation (3.10) is involved to calculate the parameters in Rietveld refinement. Rietveld Refinement directly matches the intensities of all the peaks throughout the test range with the intensities of peaks from the model structures, and it is less sensitive to both model and experimental errors. However, to get more accurate information about crystalline materials, a wide

range 2θ of experimental pattern and good models in database are needed. In addition, the experience of operating the Rietveld programs is quite necessary along with a good chemical knowledge in terms of expected bond distances.

3.7 Field Emission Scanning electron microscopy (FESEM)

The surface morphology and nano structured particle size of the prepared sample has been carried out by field emission scanning electron microscope, FESEM (JEOL JSM 7600F) from Glass & Ceramic Engineering Department of Bangladesh University of Engineering and Technology, Dhaka, Bangladesh. For FESEM measurement, powder sample that sintered at 850°C for 3 hours.



Figure 3.10: Field Emission Scanning Electron Microscope (FESEM).

3.8 Vibrating Sample Magnetometer (VSM)

The principle of VSM is the measurement of the electromotive force induced by magnetic sample when it is vibrates at a constant frequency in the presence of a static and uniform magnetic field. A small part of the (10-50mg) was weighed and made to avoid movements inside the sample holder. Fig.(3.11) shows Vibrating Sample Magnetometer (VSM) of Model EV7 system. The magnetic properties measurement system Model EV7 is a sophisticated analytical instrument configured specially for the study of the magnetic properties of small samples over a broad range of temperature from 103K to 800K and magnetic field from -20KO_e to $+20\text{KO}_e$. Vibrating Sample Magnetometer is a versatile and sensitive method of measuring magnetic

properties developed by S. Foner of MIT in 1956 and is based on the flux change in a coil when the sample is vibrated near it.

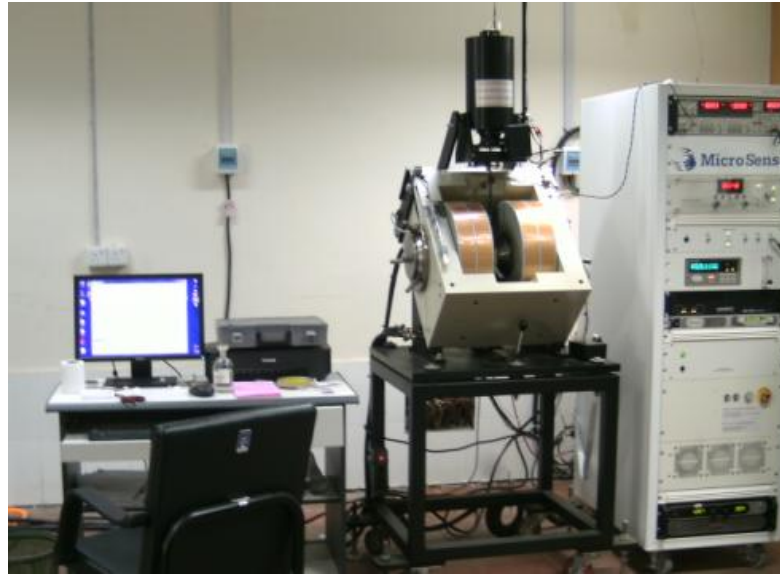


Figure 3.11: Vibrating Sample Magnetometer

The VSM is designed to continuously measure the magnetic properties of materials as a function of temperature and field. In this type of magnetometer, the sample is vibrated up and down in a region surrounded by several pickup coils. The magnetic sample is thus acting as a time-changing magnetic flux, varying magnetic flux is accompanied by an electric field and the field induces a voltage in pickup coils. This alternating voltage signal is processed by a control unit system, in order to increase the signal to noise ratio. The result is a measure of the magnetization of the sample.

3.9 Electrical and dielectric measuring systems

Electrical properties have been studied in terms of measurements of DC-electrical resistivity, and dielectric properties. The electrical resistivity was measured in a temperature range 298-673K by using two probes method, while the dielectric properties measurements were performed at room temperature using an LCR meter bridge (Wayne Kerr LCR 4275) in a frequency range of 100 Hz to 3 MHz.

3.9.1 DC and AC resistivity measurement

Compositional dependence of DC resistivity and frequency dependence of AC resistivity of the samples has been measured using conventional two probe method, using pellet samples of diameter 8.3–8.8 mm and of thickness 1.2–2.5 mm by applying silver electrodes on the surfaces. Samples were prepared by sintering the samples at 1300°C for 6 hours. The samples were polished using metallurgical polishing machine with the help of silicon carbide papers with grit size 600. After that the samples were clean with acetone and then again polished with special velvet type polishing cloth named as alpha gam, for finer polishing using fine alumina powder of grain size 0.05 micron dispersed in a liquid. The powders were of various sizes starting with 1 micron to 0.05 micron. Samples are then cleaned in a ultrasonic cleaner and dried in surface at 150 °C for several hours [3.23].

Then the samples are again cleaned with acetone and silver paste was added to both the sides of the polished pellet samples together with two thin copper wires of 100 micron diameter for conduction. Again the samples are dried at 150 °C to eliminate any absorbed moisture. The DC and AC resistivity were measured as a function of frequency in the range 1 kHz–12 MHz at room temperature by Electrometer Keithley model 6514 and impedance analyzer.

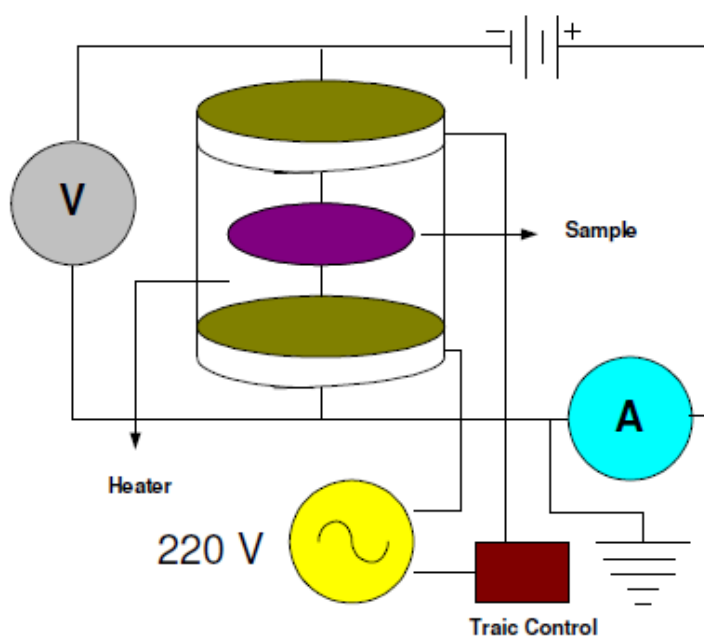


Figure 3.12: Flow sheet diagram of the two-probe resistivity apparatus [3.24].

The main components of this device are given below:

- 1) High voltage power (up to 210 V)
- 2) A heating element
- 3) A thermocouple
- 4) A control TRAIC
- 5) Digital multimeter
- 6) A sample holder equipped with two electrodes

Above mentioned components are assembled as described below (Fig. 3.12). Sample holder equipped with two electrodes which are arranged symmetrically with respect to each other on opposite sides of the sample, was inserted into a small heating oven that was fitted inside a hollow ceramic cylindrical jar. The shape of the sample analyzed in two probe method can be disc like, cylindrical, cube, or parallelepiped. A thermocouple connected with a UT-55 multimeter was capable of measuring the temperature in the range 73 to 1473 K. A triac controller was inserted in series with the heater to heat the sample at a controlled rate. DC-power supply and Source Meter (KEITHLEY 2400) was connected in series with the sample holder. The temperature was noted with a step of 5 K, and the corresponding change of current flowing through a sample is measured by the Source Meter (KEITHLEY 2400) with a given voltage applied across the sample. In the present work DC-electrical resistivity was measured with disk shape pellets of the sample having 13mm diameter and 2mm thickness. The electrical resistance of a material is defined as the ratio between the applied voltage (V) to electrical current (I) flowing through it, given by Ohm's law:

$$R=V/I \quad (3.11)$$

The resistivity of the samples has been calculated by following equation [3.25]:

$$\rho=RA/L \quad (3.12)$$

Where, R is resistance, L is the thickness and A is the cross sectional area of the pellets (of the dimensions mentioned on the previous page).

The activation energy and drift mobility of all the samples were also calculated from DC-electrical resistivity data. The electrical resistivity of the ferrite materials decreases with the increase in temperature obeying the Arrhenius type equation [4.26]:

$$\rho = \rho_o \exp\left(\frac{E_a}{K_B T}\right) \quad (3.13)$$

Where, k_B is the Boltzmann constant, T is temperature (K) and E_a is the activation energy needed for the hopping of an electron from one ion to the other neighboring ion of the same element with the different valence state, which give rise to a conduction in materials. The drift mobility (μ_d) of the doped Mg-ferrite samples was calculated using the relation [3.26]:

$$\mu_d = \frac{1}{ne\rho} \quad (3.14)$$

Where, e is the charge of the electron, the DC-electrical resistivity at given temperature and n is the concentration of charge carriers which can be calculated from the relation:

$$n = \frac{N_A d_b p_{Fe}}{M} \quad (3.15)$$

Where, N_A is the Avogadro's number, d_b the bulk density, M the molecular mass of the sample and p_{Fe} is the number of iron atom in the chemical formula of the samples.

3.9.2 Dielectric properties measuring system

Spinel ferrites are attractive materials with many applications in high frequency microwave devices. Therefore, it is important to study their dielectric behavior at different frequencies. The inductance, capacitance and resistance (LCR) Meter Bridge provide economical, thorough and accurate testing with a basic accuracy of 0.1%, of any dielectric materials at frequencies up to several frequency ranges. It can automatically measure the inductance (L), capacitance (C) and resistance (R) and other parameters such as the quality factor, impedance, AC resistance, conductance and dielectric loss tangent of the subjected materials.

It consists of a power supply (PS) to generate the AC voltage, resistor, and amplifiers. Voltage is applied to the sample (S) through the source resistance 'RS' (B), which varies depending on the measuring range. The current flows through the resistor RR to operational amplifiers (A1 and A2). The amplifier automatically adjusts the voltage gain level, so that an electric current passing through a resistor should be equal to the current flowing through the sample and provides an output signal proportional to that current. The voltage across the sample is measured by a separate signal path with a four wire Kelvin connection. Out of these four wires Kelvin, two wires used to perform the test current and two independent wires for the detection of voltage across the sample. The real and imaginary signals are obtained by multiplying the voltage

and current signals with a reference signal in phase with supply voltage and other shifted 90° from the power supply voltage. These signals are read by a microprocessor (M). This prevents the voltage drop in the current carrying wires to affect the voltage measurement. The LCR meters are controlled by a high speed microcontroller that runs the display, keypad, general purpose interface bus (GPIB), computer interfaces and handler interface. The schematic diagram of LCR meter is shown in Figure 3.13.

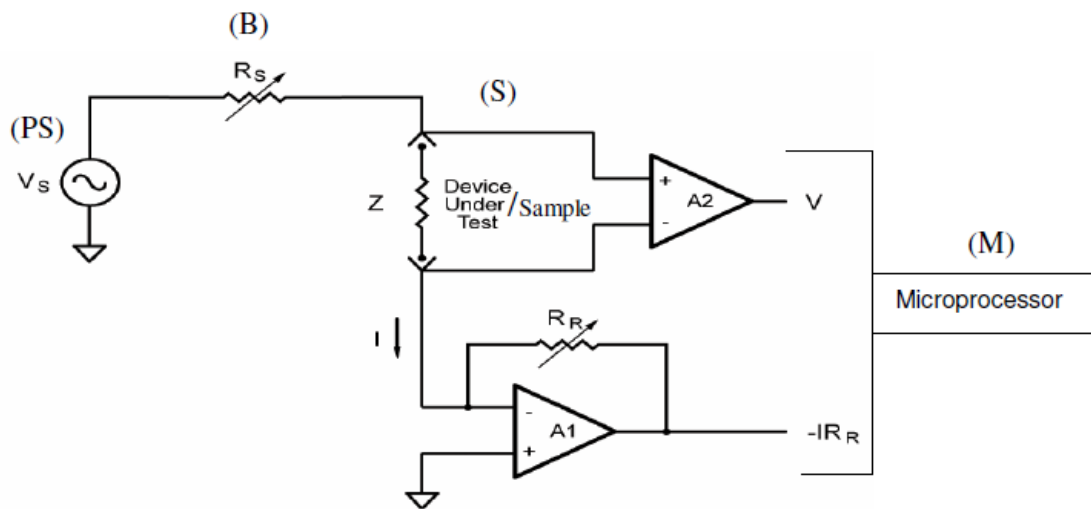


Figure 3.13: Schematic diagram of an LCR meter [3.27].

The dielectric constant (ϵ') and dielectric loss tangent ($\tan\delta$) are calculated from data of inductance, capacitance and resistance. The Dielectric constant is a measure of the degree to which a medium can resist the flow of charge, is calculated as follows:

$$\epsilon' = \frac{CL}{\epsilon_0 A} \quad (3.16)$$

Where, C is the capacitance of the pellet in farad, L the thickness and A the cross sectional area of the pellet and $\epsilon_0 = 8.85 \times 10^{-12} \text{Fm}^{-1}$, the constant of permittivity of free space. The amount of energy loss during each cycle is expressed as the dielectric loss tangent ($\tan\delta$) of dielectric material and its value is directly given by the instrument in the form of D . D is called the dissipation factor and is the real part of the impedance divided by the reactance (the imaginary part of the impedance).

Dielectric measurements were achieved using a HP 4192A impedance gain phase analyzer operating in the frequency range 10 Hz-13 MHz. The capacitance and conductance measurements have been evaluated to obtain the dependence of permittivity (ϵ') and (ϵ''), tangent loss ($\tan \delta$) and ac electrical conductivity (σ_{ac}). The complex permittivity can be written as [3.28-3.29]:

$$\epsilon^* = \epsilon' - i\epsilon'' \quad (3.17)$$

Where (ϵ') and (ϵ'') are the real and imaginary parts of complex permittivity, and i is the imaginary root of -1 . The real part of the complex permittivity, the dielectric constant (ϵ'), at the various frequencies is calculated using the measured capacitance values at the strong accumulation region from the relation [3.28-3.30]:

$$\epsilon' = \frac{C}{C_0} = \frac{C d_i}{\epsilon_0 A} \quad (3.18)$$

Where C is the measured capacitance, C_0 is the capacitance of an empty capacitor, A is the rectifier contact area of the structure in cm^2 , d_i is the interfacial insulator layer thickness and ϵ_0 is the permittivity of free space charge ($\epsilon_0 = 8.85 \times 10^{-14} \text{ F/cm}$). In the strong accumulation region, the maximal capacitance of the structure corresponds to the insulator capacitance

$$(C_{ac} = C_i = \epsilon' \epsilon_0 \frac{A}{d_i}) \quad (3.19)$$

The imaginary part of the complex permittivity, the dielectric loss (ϵ''), at the various frequencies is calculated using the measured conductance values from the relation:

$$\epsilon'' = \frac{S}{\omega C_i} = \frac{S d_i}{\epsilon_0 \omega A} \quad (3.20)$$

Where S is the conductance of the device and ω is the angular frequency. The tangent loss ($\tan \delta$) can be expressed as follows [3.28-3.30]:

$$\tan \delta = \frac{\epsilon''}{\epsilon'} \quad (3.21)$$

The ac electrical conductivity (σ_{ac}) of the dielectric material can be given by the following equation [11]:

$$\sigma_{ac} = \omega C \tan \delta \left(\frac{d_i}{A} \right) = \epsilon'' \omega \epsilon_0 \quad (3.22)$$

3.9.3 Impedance Analyzer

Electrical impedance is the measure of the opposition that a circuit presents to a current when a voltage is applied. In quantitative terms, it is the complex ratio of the voltage to the current in an alternating current (AC) circuit. Impedance extends the

concept of resistance to AC circuits, and possesses both magnitude and phase, unlike resistance, which has only magnitude. When a circuit is driven with direct current (DC), there is no distinction between impedance and resistance; the latter can be thought of as impedance with zero phase angle.

Impedance is defined as the frequency domain ratio of the voltage to the current. In other words, it is the voltage–current ratio for a single complex exponential at a particular frequency ω . In general, impedance will be a complex number, with the same units as resistance, for which the SI unit is the ohm (Ω). For a sinusoidal current or voltage input, the polar form of the complex impedance relates the amplitude and phase of the voltage and current. In particular

- The magnitude of the complex impedance is the ratio of the voltage amplitude to the current amplitude.
- The phase of the complex impedance is the phase shift by which the current lags the voltage.

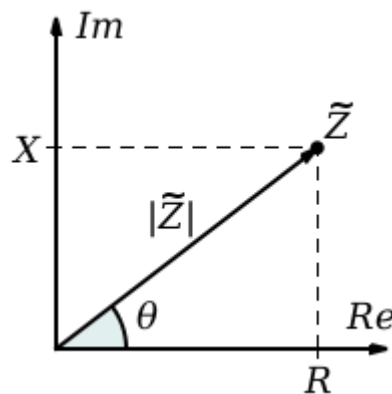


Figure 3.14: The real and imaginary part of impedance with resistance variance

3.10 Theories of Permeability

Permeability is namely defines as the proportional constant between the magnetic field induction B and applied intensity H [3.31-3.32]:

$$B = \mu H \quad (3.23)$$

If a magnetic material is subjected to an AC magnetic field as given below:

$$H = H_0 e^{i\omega t} \quad (3.24)$$

Then it is observed that the magnetic flux density B experiences a delay. The delay is caused due to presence of various losses and is thus expressed as

$$\mathbf{B} = B_0 e^{i(\omega t - \delta)} \quad (3.25)$$

Where δ is the phase angle and marks the delay of B with respect to H. The permeability is then given by

$$\mu = \frac{B}{H} = \frac{B_0 e^{i(\omega t - \delta)}}{H_0 e^{i\omega t}} \quad (3.26)$$

$$= \frac{B_0 e^{-i\delta}}{H_0} = \mu' - i\mu'' \quad (3.27)$$

Where
$$\mu' = \frac{B_0}{H_0} \cos \delta \quad (3.28)$$

$$\mu'' = \frac{B_0}{H_0} \sin \delta \quad (3.29)$$

The real Part μ' of complex permeability μ as expressed in Eqⁿ. (3.26) represent the component of B which is in phase with H, so it corresponds to the normal permeability. If there is no losses, we should have $\mu = \mu'$, The imaging part μ'' corresponds to the part of B which is delayed by phase angle arranging up to 90° from H [3.33-3.43]. The presence of such a component requires a supply of energy to maintain the alternating magnetization regardless of the origin of delay. The ratio of μ'' to μ' gives

$$\frac{\mu''}{\mu'} = \frac{\frac{B_0}{H_0} \sin \delta}{\frac{B_0}{H_0} \cos \delta} = \tan \delta \quad (3.30)$$

This $\tan \delta$ is called the loss Factor or loss tangent. The Q-Factor or quality factor is defined as the reciprocal of this loss factor, i.e

$$Q = \frac{1}{\tan \delta} \quad (3.31)$$

And the relative quality factor = $\mu_i Q$ (3.32)

The behavior of μ' and μ'' versus frequency is called the permeability spectrum. The initial permeability of a ferromagnetic or ferrimagnetic substance is the combined effects of the wall permeability and rotational permeability mechanisms.

RESULTS AND DISCUSSION

4.1 X-ray Diffraction Analysis

The XRD patterns of the composites are shown in Figure 4.1. The composites were annealed at 850°C for two hours to and used in powder diffraction technique. The plot has been illustrated in association with Rietvelt refinement which makes correlation between experimental data with theoretical judgment. The XRD data was collected from Rigacu Miniflex of Bose Institute, Kolkata, India. The Rietvelt refinement was applied to XRD pattern by using Fullprof package [4.1]. From XRD pattern the phase position with its shift, lattice size would be understand and by applying Rietvelt refinement on experimental data it also is able to know the phase fraction, crystal structure, Bragg factor etc. In the prepared multiferroic compositions there has huge possibility to get multiphase for different types of materials. In this research the samples are in general have Rhombohedral and cubic phase because of having Perovskite and ferrite contents. But there has much prospect to get another phase for the distortion of having multiphase which is generating by Rietveld refinement. So XRD pattern gave the exact phase position of the phases inside composites.

4.1.1 The Pure $R3c$ Phase

From Figure 4.1, the pure perovskite BLFO structure is shown for $x = 0$ which clearly represents the distorted rhombohedral phase that belongs to $R3c$ space group. The phase is in hexagonal with rhombohedral structure which exposed by the peak position in $2\theta \sim 32^\circ$. In Figure 4.1, for $x = 0$, an impure phase has been detected which is indicated by * as secondary impurity. Two doubly split peaks of BLFO (104) and (110) at $2\theta \sim 32^\circ$, (006) and (202) at $2\theta \sim 39^\circ$, (116) and (122) at $2\theta \sim 51^\circ$, (018) and (214) $2\theta \sim 56^\circ$ have merged into a single broadening peak which referred the higher structural distortion due to adding lanthanum [4.2]. Merging of two distinguish indexed peaks in a single peak which was investigated as the phase transition from rhombohedral to orthorhombic due to ion doping [4.3 - 4.5]. The addition of La^{3+} endorses the stabilization of perovskite phase [4.6].

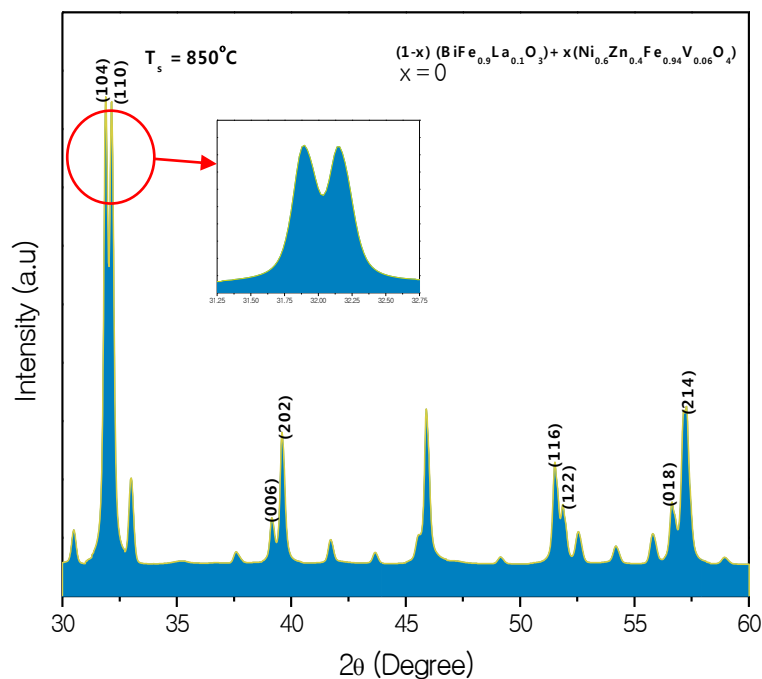


Figure 4.1: BLFO XRD pattern where enlarged scale shows the merging of two indexed peaks in a single peak.

4.1.2 The Distorted Orthorhombic Phase

From Figure 4.2, there has no defined (111) peak seen near $2\theta \sim 27^\circ$, which is taken as the proof of the rhombohedral to orthorhombic structure change [4.7]. The evidence of distorted orthorhombic phase is confirmed by Rietveld refinement given in Table 5.3. The impurity phase is seen in undoped BLFO pattern in Figure 4.2 (indicated by *). The representation of merged two split peaks in a single broadening peak is given in Figure 4.1. Here colored region has specified the split region.

4.1.3 The Pure Cubic Phase

From Figure 4.2, for $x = 1$, it is shown that the highest peak is visible at $2\theta \sim 32^\circ$ which confirms the cubic formation of ferrite phase. There has no extra peak and no peak is distorted which refers the purity of cubic spinel structure. Table 5.1 (b) represented the lattice parameter of cubic spinel phases. The absence of impurity or secondary peak in pure ferrite NZVF content provides homogeneity of the sample for $x = 1$.

4.1.4 Domination of NZVF on BLFO Phase

The shift in BLFO rhombohedral phase by adding cubic spinel structured NZVF is observed from Figure 4.2 and 4.3. The picture clearly revealed that the addition of NZVFO instead of BLFO causes phase transition which confirms by shifting the rhombohedral peaks towards right for $x = 1$ and $x = 2$. It is also seen that the rhombohedral phase peaks are attenuated and shrunk due the addition of NZVF up to $x = 0.7$ and for $x = 1$ it almost diminished. On the other hand the increasing in NZVF content, cubic phase is appeared and the size of FWHM is broadened and larger for $x = 1$. For $x = 3$, the rhombohedral peak again back towards left which may be attributed for more addition of NZVF content.

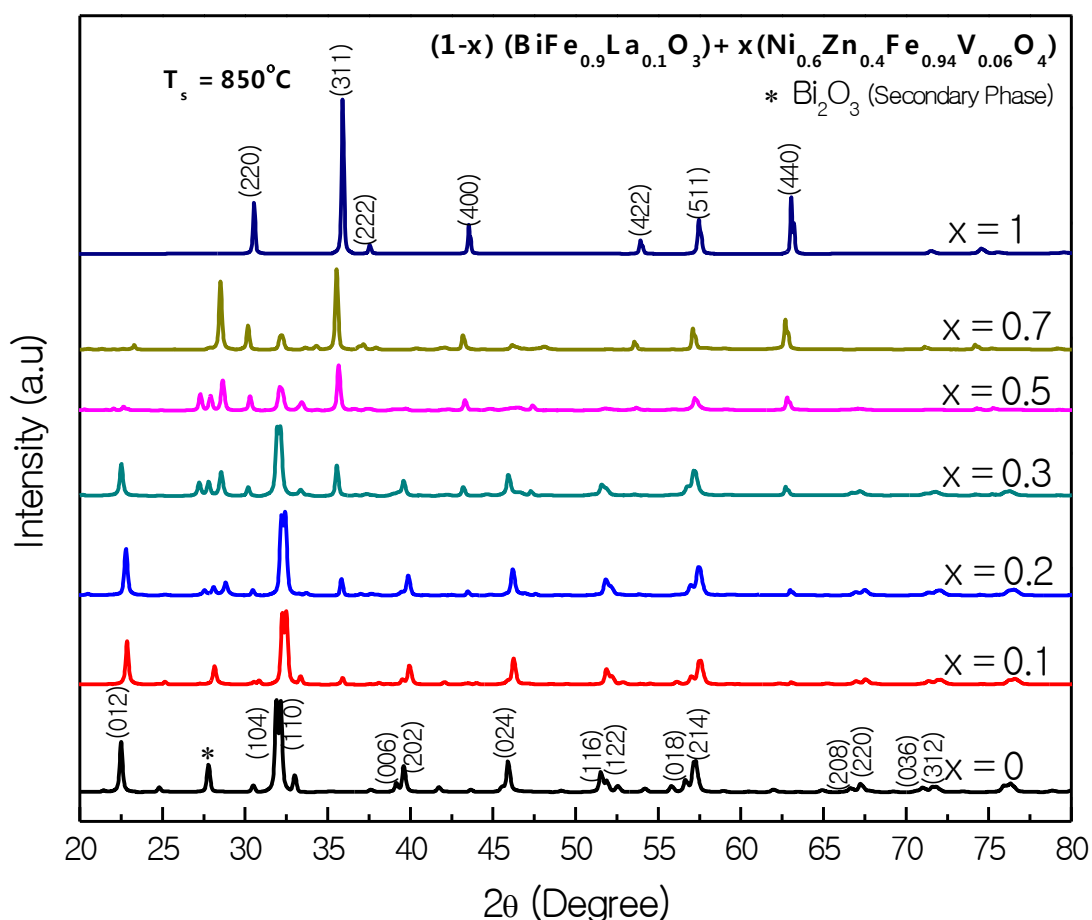


Figure 4.2: X-ray diffraction pattern of $(1-x) \text{BiFe}_{0.9}\text{La}_{0.1}\text{O}_3 + x \text{Ni}_{0.6}\text{Zn}_{0.4}\text{Fe}_{0.94}\text{V}_{0.06}\text{O}_4$ multiferroic composites with x variation at 850°C annealing temperature

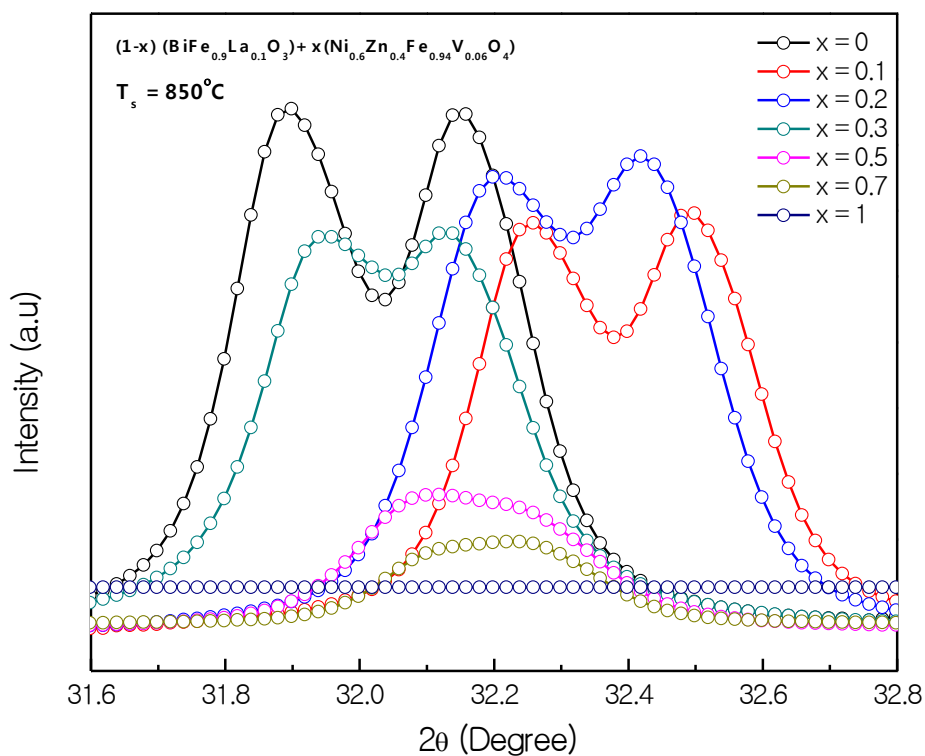


Figure 4.3: Broadening of peaks of XRD pattern of (1-x) BiFe_{0.9}La_{0.1}O₃+ xNi_{0.6}Zn_{0.4}Fe_{0.94}V_{0.06}O₄

4.1.5 Rietveld Refinement of (1-x) BiFe_{0.9}La_{0.1}O₃+xNi_{0.6}Zn_{0.4}Fe_{0.94}V_{0.06}O₄

From Figure 4.4, the Rietveld refinement is presented in association with matching experimental and theoretical data. The black line stands for calculated data and red circle stands for observed data. The BLFO rhombohedral phase (*R3c*), impurity phase as secondary phase Bi₂₅FeO₃₉ (*I23*) and Bi₂Fe₄O₉ (*Pbam*), and cubic phase NZVFO (*Fd-3m*) are denoted by the color code of orange, red, blue and sky blue respectively which are representing each phase belong with the composite structure. From Figure 4.5, the phase fraction (wt%) due to rhombohedral and cubic phase formation in composites are given. The figure clearly disclosed that, the increasing in NZVFO content takes place of BLFO inside the composite which also co-related with the formula of composition (1-x) BiFe_{0.9}La_{0.1}O₃+ xNi_{0.6}Zn_{0.4}Fe_{0.94}V_{0.06}O₄.

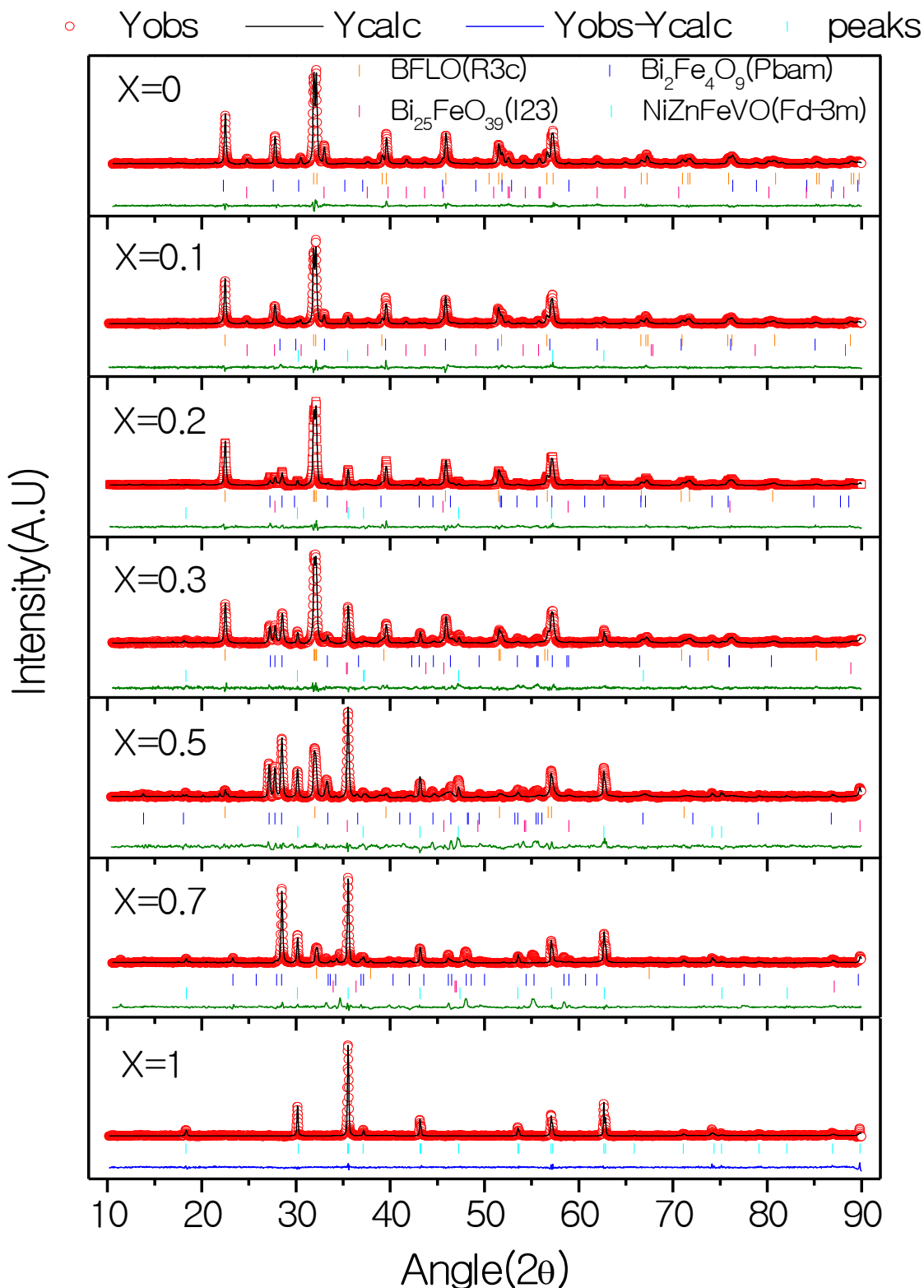


Figure 4.4: Representation of XRD data with Rietvelt Refinement. The red circle, black line, blue and light sky blue line represents the value for observed, calculated data and peaks respectively of $(1-x)\text{BiFe}_{0.9}\text{La}_{0.1}\text{O}_3 + x\text{Ni}_{0.6}\text{Zn}_{0.4}\text{Fe}_{0.94}\text{V}_{0.06}\text{O}_4$

Basically NZVFO contents are substituted instead of BLFO content with the variation in x . So the phase fraction (wt%) of each phases should be co-linear or associated with other. Otherwise, the preparation may be not satisfied the formula. Fortunately, the phase fraction is finely fitted where the decreasing in BLFO content is seen from the Figure 5.5 with increasing NZVFO at same sequence. There has no visible fluctuation in the phase formation which could be formed in the time of sample preparation. The harmony between increasing NZVFO phase and decreasing BLFO phase is confirmed that the preparation technique was good and there had no significant error.

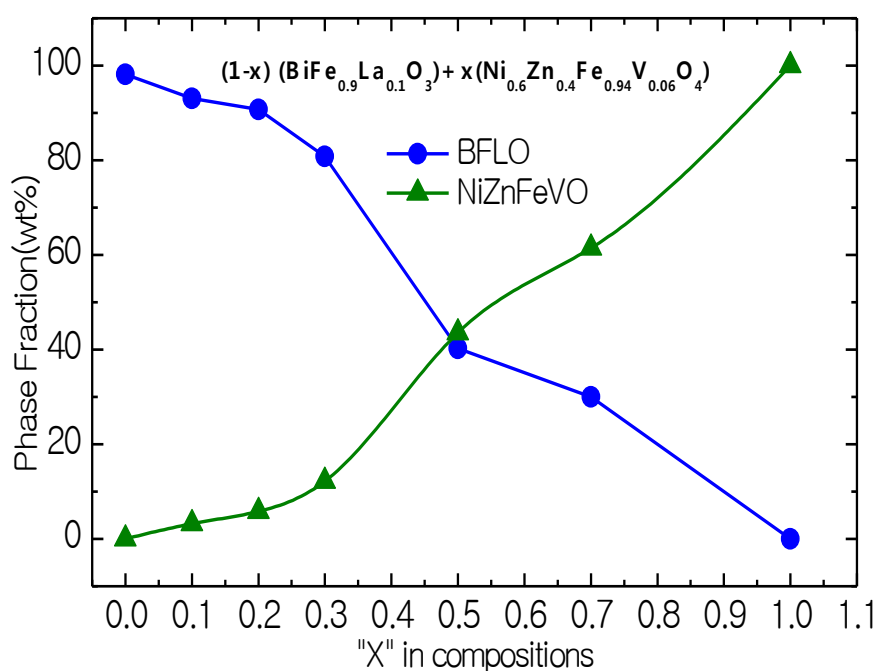


Figure 4.5: Phase fraction for $x=0, 0.1, 0.2, 0.3, 0.5, 0.7, 1$ of $(1-x) \text{BiFe}_{0.9}\text{La}_{0.1}\text{O}_3 + x\text{Ni}_{0.6}\text{Zn}_{0.4}\text{Fe}_{0.94}\text{V}_{0.06}\text{O}_4$

From Rietveld refinement, the lattice parameter, lattice volume, goodness of fitting, residuals for the unweighed pattern and residuals for the weighed pattern of the compositions are calculated for both perovskite and cubic phases. In Table 4.1 (a), the formation of perovskite phase is established for all contents which are carrying BLFO. Except $x = 1$, all other composites with BLFO contents are belonging with $R3c$ space group and rhombohedral phase with hexagonal structure. From the Table, it is seen that, calculated lattice parameter for both of a_{hex} and c_{hex} are decreased with increasing x as NZVFO content. In the preparation formula $(1-x) \text{BiFe}_{0.9}\text{La}_{0.1}\text{O}_3 +$

$x\text{Ni}_{0.6}\text{Zn}_{0.4}\text{Fe}_{0.94}\text{V}_{0.06}\text{O}_4$, it is seen that the NZVFO contents are substituted against BLFO. So the decreasing in BLFO content is responsible for the decreasing both of a_{hex} and c_{hex} . The hexagonal structure has been confirmed from the dissimilarity between a_{hex} and c_{hex} values. The synchronization of decreasing a_{hex} and c_{hex} with decreasing BLFO contents reveals that the perovskite BLFO has hexagonal structure with rhombohedral phase. Due to decrease in a_{hex} and c_{hex} , the lattice volume is shrinking. The ratio between c_{hex} and a_{hex} not uniform which is one of strong evidence of hexagonal structure formation.

Table 4.1. Rietveld refined structural parameters obtained from XRD with χ^2 (Goodness of fit), R_p (residuals for the unweighed pattern) and R_{wp} (residuals for the weighed pattern) of the compositions:

(a) $(1-x)(\text{BiFe}_{0.9}\text{La}_{0.1}\text{O}_3)$:

Parameters	x=0	x=0.1	x=0.2	x=0.3	x=0.5	x=0.7
Space Group	<i>R3c</i>	<i>R3c</i>	<i>R3c</i>	<i>R3c</i>	<i>R3c</i>	<i>R3c</i>
$a_{\text{hex}}(\text{\AA})$	5.5656(1)	5.5727(2)	5.5703(2)	5.5696 (3)	5.5721(7)	5.5736 (9)
$c_{\text{hex}}(\text{\AA})$	13.8000(5)	13.8064(7)	13.7938(8)	13.7750(10)	13.7609(21)	13.5550(36)
$V (\text{\AA}^3)$	370.19(2)	371.32(3)	370.65(3)	370.05(4)	370.01(9)	364.67 (13)
$a_n = a_{\text{hex}}/\sqrt{2}$	3.9354	3.9404	3.9388	3.9383	3.9422	3.9411
$C_n = c_{\text{hex}}/\sqrt{2}$	3.9837	3.9856	3.9819	3.9765	3.9725	3.913
c_n/a_n	1.01227	1.01147	1.01094	1.0097	1.00769	0.99287
χ^2	1.12	1.40	1.79	2.12	1.94	3.58
R_p	15.7	24.2	22.5	25.8	36.9	39.9
R_{wp}	13.7	18.6	18.9	21.5	28.9	33.6

In Table 4.1 (b), the space group, lattice parameter, lattice volume and goodness of fitting for cubic phase are reported. The NZVFO contents were substituted against BLFO contents, so in pure BLFO there has no cubic phase. But from $x = 0.1$ to $x = 1$, the addition of NZVFO establish cubic structure inside the composite where two distinguish phases are belonging at same region except pure BLFO. All space groups are in Fd-3m which makes sure that the phases are in cubic structure. The lengths of three lattice sites are equal and from this phenomenon it can claim that the NZVFO has cubic structure. For cubic structure, the ratio between two lattice sites should be

almost 1. From the table it is seen that the ratio between the lattice parameter c and a is 1 which finalized that the NZVFO is in cubic structure with Fd-3m phase.

(b) $x(\text{Ni}_{0.6}\text{Zn}_{0.4}\text{Fe}_{0.94}\text{V}_{0.06}\text{O}_4)$:

Parameters	x=0.1	x=0.2	x=0.3	x=0.5	x=0.7	x=1
Space Group	Fd-3m	Fd-3m	Fd-3m	Fd-3m	Fd-3m	Fd-3m
$a = b = c$ (Å)	8.3809 (6)	8.3770(4)	8.3752(4)	8.3803 (5)	8.3766(45)	8.3786(3)
V (Å ³)	588.676(8)	587.86(5)	587.48(5)	588.536(6)	587.76 (5)	588.18(4)
c_n/a_n	1	1	1	1	1	1
χ^2	1.40	1.79	2.12	1.94	3.58	1.62
R_p	24.2	22.5	25.8	36.9	39.9	41.1
R_{wp}	18.6	18.9	21.5	28.9	33.6	24.0

Table 4.2 is illustrated with all calculated values obtained from Rietveld refinement. The composites with BLFO content provides pure $R3c$ and secondary impure orthorhombic phases as $\text{Bi}_2\text{Fe}_4\text{O}_9$ and $\text{Bi}_{25}\text{FeO}_{39}$. Due to higher order distortion, there has a pseudo cubic (I23) phase has been appeared. As discussed above, the two split peaks have merged in a single peak where extinction of regular nonexistence at higher doping levels refers a structural change from the rhombohedral structure of BLFO in a pseudo cubic structure to preserve the noncentro symmetry, which may be grown up for awfully minute monoclinic distortions [4.7]. But the absence of (111) peak may be resulted the invisibility of the distortion [4.7].

For $x = 0$, the amount of pure BLFO is 98.11%. This is much satisfactory that BLFO has large domination on phase formation than other secondary phases, so these secondary phases will has no longer affect on other fundamental properties. The substitution of NZVFO contents develops not only cubic phase but also it helps to make stronger the secondary phases inside pervskite BLFO. The higher concentration of NZVFO for $x = 0.1$ to 0.7, establish cubic structure with rhombohedral phase but this makes a structural distortion inside BLFO which is responsible for the higher value of secondary phases.

Goodness of fitting was calculated in association with R_p and R_{wp} factors by using equation (3.10). The parameter for goodness of fitting χ^2 is the main key of understanding the fitness of other parameters.

Table 4.2. Rietveld refined structural parameters and phases fractions (wt%) obtained from XRD with R_{Bragg} (Bragg factor), χ^2 (Goodness of fit), R_f (structure factor), R_p (residuals for the unweighed pattern) and R_{wp} (residuals for the weighed pattern) of the compositions: $(1-x)(\text{BiFe}_{0.9}\text{La}_{0.1}\text{O}_3) + x(\text{Ni}_{0.6}\text{Zn}_{0.4}\text{Fe}_{0.94}\text{V}_{0.06}\text{O}_4)$

Sample	Crystal Structure	Phase percentages (wt%)	Lattice Parameters (Å)	R Factor (%)	χ^2
x=0	<i>BFL</i> R3c (Rhombohedral)	98.11(1)	a= b = 5.5656 (1) c = 13.8000 (5)	$R_p = 15.7, R_{\text{wp}} = 13.7$ $R_B = 3.65, R_f = 3.38$	1.12
	<i>Bi₂Fe₄O₉</i> pbam (Orthorhombic)	0.86(0)	a = 7.9752 (19), b = 10.1904 (12) c = 4.8794 (6)	$R_p = 15.7, R_{\text{wp}} = 13.7$ $R_B = 13.9, R_f = 7.40$	
	<i>Bi₂₅FeO₃₉</i> I23 (Cubic)	1.04(0)	a = b = c = 10.1518 (4)	$R_p = 15.7, R_{\text{wp}} = 13.7$ $R_B = 10.58, R_f = 7.41$	
x=0.1	<i>BFL</i> R3c (Rhombohedral)	93.04(1)	a= b = 5.5727 (2) c = 13.8064 (7)	$R_p = 24.2, R_{\text{wp}} = 18.6$ $R_B = 5.63, R_f = 5.67$	1.40
	<i>Bi₂Fe₄O₉</i> pbam (Orthorhombic)	3.57(0)	a = 7.8767 (52), b = 10.5605 (37) c = 5.1138 (30)	$R_p = 24.2, R_{\text{wp}} = 18.6$ $R_B = 28.9, R_f = 31.6$	
	<i>Bi₂₅FeO₃₉</i> I23 (Cubic)	0.20(0)	a = b = c = 10.1592 (8)	$R_p = 24.2, R_{\text{wp}} = 18.6$ $R_B = 24.3, R_f = 23.4$	
	<i>Ni_{0.6}Zn_{0.4}Fe_{0.94}V_{0.06}O₄</i> Fd-3m (Cubic)	3.20(0)	a = b = c = 8.3809 (6)	$R_p = 24.2, R_{\text{wp}} = 18.6$ $R_B = 18.1, R_f = 21.2$	
x=0.2	<i>BFL</i> R3c (Rhombohedral)	90.74(1)	a= b = 5.5703 (2) c = 13.7938 (8)	$R_p = 22.5, R_{\text{wp}} = 18.9$ $R_B = 4.47, R_f = 4.54$	1.79
	<i>Bi₂Fe₄O₉</i> pbam (Orthorhombic)	3.44(0)	a = 8.1437 (21), b = 10.4743 (30) c = 4.8898 (30)	$R_p = 22.5, R_{\text{wp}} = 18.9$ $R_B = 22.1, R_f = 15.0$	
	<i>Bi₂₅FeO₃₉</i> I23 (Cubic)	0.02(0)	a = b = c = 10.1488 (21)	$R_p = 22.5, R_{\text{wp}} = 18.9$ $R_B = 32.3, R_f = 19$	
	<i>Ni_{0.6}Zn_{0.4}Fe_{0.94}V_{0.06}O₄</i> Fd-3m (Cubic)	5.80(0)	a = b = c = 8.3770 (4)	$R_p = 22.5, R_{\text{wp}} = 18.9$ $R_B = 22.4, R_f = 16.2$	
x=0.3	<i>BFL</i> R3c (Rhombohedral)	80.78(1)	a= b = 5.5696 (3) c = 13.7750 (10)	$R_p = 25.8, R_{\text{wp}} = 21.5$ $R_B = 4.11, R_f = 4.57$	2.12
	<i>Bi₂Fe₄O₉</i> pbam (Orthorhombic)	7.05(0)	a = 8.1228 (17), b = 10.4902 (17) c = 4.9004 (12)	$R_p = 25.8, R_{\text{wp}} = 21.5$ $R_B = 18.0, R_f = 15.8$	
	<i>Bi₂₅FeO₃₉</i> I23 (Cubic)	0.03(0)	a = b = c = 10.1319 (46)	$R_p = 25.8, R_{\text{wp}} = 21.5$ $R_B = 35.7, R_f = 21.4$	
	<i>Ni_{0.6}Zn_{0.4}Fe_{0.94}V_{0.06}O₄</i> Fd-3m (Cubic)	12.14(0)	a = b = c = 8.3752 (4)	$R_p = 25.8, R_{\text{wp}} = 21.5$ $R_B = 14.9, R_f = 10.7$	
x=0.5	<i>BFL</i> R3c (Rhombohedral)	40.22(1)	a= b = 5.5721 (7) c = 13.7609 (21)	$R_p = 36.9, R_{\text{wp}} = 28.9$ $R_B = 11.5, R_f = 13.2$	1.94
	<i>Bi₂Fe₄O₉</i> pbam (Orthorhombic)	16.21(1)	a = 8.1135 (15), b = 10.4991 (16) c = 4.9246 (11)	$R_p = 36.9, R_{\text{wp}} = 28.9$ $R_B = 20.8, R_f = 19.1$	
	<i>Bi₂₅FeO₃₉</i> I23 (Cubic)	0.07(0)	a = b = c = 10.1270 (45)	$R_p = 36.9, R_{\text{wp}} = 28.9$ $R_B = 37.2, R_f = 26.8$	
	<i>Ni_{0.6}Zn_{0.4}Fe_{0.94}V_{0.06}O₄</i> Fd-3m (Cubic)	43.51(1)	a = b = c = 8.3803 (5)	$R_p = 36.9, R_{\text{wp}} = 28.9$ $R_B = 15.7, R_f = 12.0$	
x=0.7	<i>BFL</i> R3c (Rhombohedral)	29.98(1)	a= b = 5.5736 (9) c = 13.5550 (36)	$R_p = 39.9, R_{\text{wp}} = 33.6$ $R_B = 19.5, R_f = 28.6$	3.58
	<i>Bi₂Fe₄O₉</i> pbam (Orthorhombic)	8.52(0)	a = 8.3251 (26), b = 10.1405 (34) c = 4.7470 (16)	$R_p = 39.9, R_{\text{wp}} = 33.6$ $R_B = 32.0, R_f = 23.0$	
	<i>Bi₂₅FeO₃₉</i> I23 (Cubic)	0.03(0)	a = b = c = 9.8764 (62)	$R_p = 39.9, R_{\text{wp}} = 33.6$ $R_B = 39.3, R_f = 40.8$	
	<i>Ni_{0.6}Zn_{0.4}Fe_{0.94}V_{0.06}O₄</i> Fd-3m (Cubic)	61.47(1)	a = b = c = 8.3766 (45)	$R_p = 39.9, R_{\text{wp}} = 33.6$ $R_B = 6.85, R_f = 5.46$	
x=1	<i>Ni_{0.6}Zn_{0.4}Fe_{0.94}V_{0.06}O₄</i> Fd-3m (Cubic)	100(1)	a = b = c = 8.3786(3)	$R_p = 41.1, R_{\text{wp}} = 24.0$ $R_B = 10.27, R_f = 16.3$	1.62

Though the value of χ^2 for $x = 0.7$ is inherently larger than other compositions which may be raised due to high order structural distortion as BLFO contents decreased in it. The composition $x = 0.7$ has least amount of BLFO where maximum space are occupied by NZVFO contents which may be one of major reason of structural distortion.

Pure NZVFO content for $x = 1$ has no structural distortion as other content have. The pseudocubic (I23) phase almost disappear in pure NZVFO content where other contents that are having BLFO provide a minimum value of distorted phase and it gives almost same result with the preparation formula.

4.2.1 Confirmation of Nano Structure

The synthesis mechanisms applied in this research was taken in account to obtain nano particle. Though there has no literature review and background work which may support this synthesis mechanism but the formation of nano particle would be a strong evidence to make sure that the mechanisms is preferable to produce nano particle. Field Emission Scanning Electron Microscopy (FESEM) is used to see the particle size and surface morphology of prepared samples. The powder sample was used in FESEM technique to observe the particle size. The purity of chemical composition which belongs with multiferroic composites having $(1-x) \text{BiFe}_{0.9}\text{La}_{0.1}\text{O}_3 + x\text{Ni}_{0.6}\text{Zn}_{0.4}\text{Fe}_{0.94}\text{V}_{0.06}\text{O}_4$ formula with constituent materials are studied by EDX spectra. The EDX spectrum for $x = 0$, $x = 0.1$ and $x = 0.2$ were also collected from FESEM technique. From the EDX pattern, the compositional contribution of each content on the composites has been calculated. The percentages of bismuth, lanthanum, nickel, zinc, vanadium and iron contents are calculated from EDX pattern.

The micrographs with EDX spectra for $x = 0$, $x = 0.1$ and $x = 0.2$ are given in Figure 5.6. From the figure it is seen that the particles are agglomerated due to the presence of liquid contents like water and acetone which were not eliminated by initial heating temperature 150°C . The prepared samples were heated for 1 hour in 150°C in a micro-oven by which the samples were dried but more temperature was required to remove the aqueous contents. The scale of FESEM micrograph is 100 nm and the micrographs implies that most visible and defined size of particles are in between 20

nm – 30 nm. So these micrographs are one of major attestation to admit that the involved synthesis mechanism is able to produce nano particle.

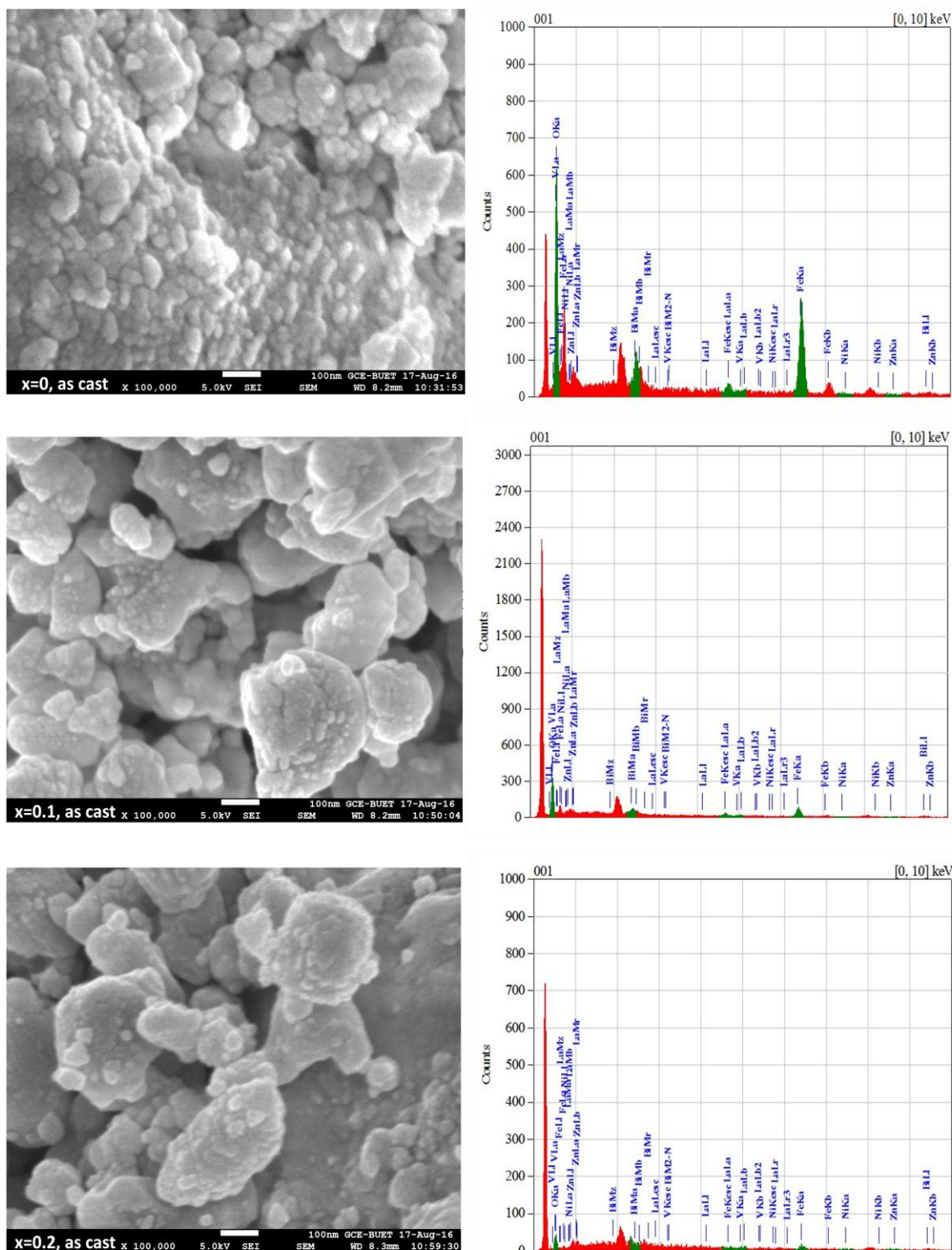


Figure 4.6 FESEM micrographs and EDX spectra of $(1-x)(\text{BiFe}_{0.9}\text{La}_{0.1}\text{O}_3) + x(\text{Ni}_{0.6}\text{Zn}_{0.4}\text{Fe}_{0.94}\text{V}_{0.06}\text{O}_4)$ for $x = 0, 0.1, 0.2$ at 150°C

In the synthesis mechanism, the mechanical effect of hand milling was helpful for homogenous mixture of the materials. Magnetic stirring had dispersed the particles which has important role to reduce the particle size because the adjacent particles were isolated by the rotation and collision with magnetic bars. Long time rotation of magnetic bars didn't give chance to rejoin of the particles which may be treated to shrink the size of the particles. Ultrasonification was a tool to provide further dispersion between the particles and the vibrational effect of ultrasound helps on reducing particle size because the vibration may able to disperse the particles. Finally the centrifugal force of centrifuge had contributed on further dispersion. After the completion centrifugation the materials were heated and then further hand milling for 30 minutes had been applied. So the continuous effect of dispersion and mechanical domination are resulted to reduce particle size in nanoscale.

4.2.2 Study of Microstructure and Morphology with the variation of Annealing Temperature

The surface morphology of BLFO and NZVFO multiferroic composites are illustrated in Figure 4.7 - 4.10. The effect of different annealing temperature on particle size and grain formation has studied by FESEM micrographs. In comparison between pure BLFO and NZVFO it is seen that the grain size of NZVFO is larger than BLFO which may be attributed due the ionic radius of NZVFO and BLFO contents. According to Shannon the ionic radii, the ionic radius of Bi^{3+} , La^{3+} is larger than of Ni^{2+} and Zn^{2+} which are given in Table: 4.3. So theoretically the grain size of pure BLFO should be greater than of NZVFO. But in the case of composite, the substitution of NZVFO on BLFO results physical strain and internal compression due the variation in ionic radius. So with increasing NZVFO, the grain boundary should be constrained which results the reduction of grain size. But in the case of pure NZVFO, the physical strain is removed because of the elimination of BLFO contents and grain size should be increased than of multiferroic composites.

Table 4.3: Shannon ionic radius for the elements used in this research

Contents	Coordination	Ionic Radius (A ^o)
Ni²⁺	IV	0.55
Zn²⁺	IV	0.60
V⁵⁺	VI	0.54
Fe³⁺	VI	0.55
Bi³⁺	VI	1.03
La³⁺	VI	1.032

The variation in grain size between mixture BLFO and NZVFO is seen from the micrographs for $x = 0.2, 0.5$ and 0.7 which are having two phases. The particles are agglomerated for the presence of some aqueous contents which would be eliminated at higher annealing temperature. Literature shows that, the addition of lanthanum at $x = 0.15$, the diameter of particles is reduced to an average diameter of 5 nm in a homogeneous size distribution [4.12] which also true for all the pure BLFO annealed contents of the present work. From Figure 4.7 - 4.10, it is seen that as temperature increases the grain size increased for undoped BLFO contents. The effect of higher annealing temperature increased secondary phases on BLFO content [4.13] which also analogous with XRD results as discussed above. In annealed composites, two different phases are having individual densification rate and thermal expansion coefficient which are responsible for internal stress [4.14]. The grain of each phase wants to closely pack with its constituents which changes the grain morphology. The internal stress and lattice distortion are resulted from that kind of change in grain morphology [4.15]. From Figure 4.7 - 4.10 the grain boundaries and grain distributions are seen. Increasing in annealing temperature provides larger grain boundary.

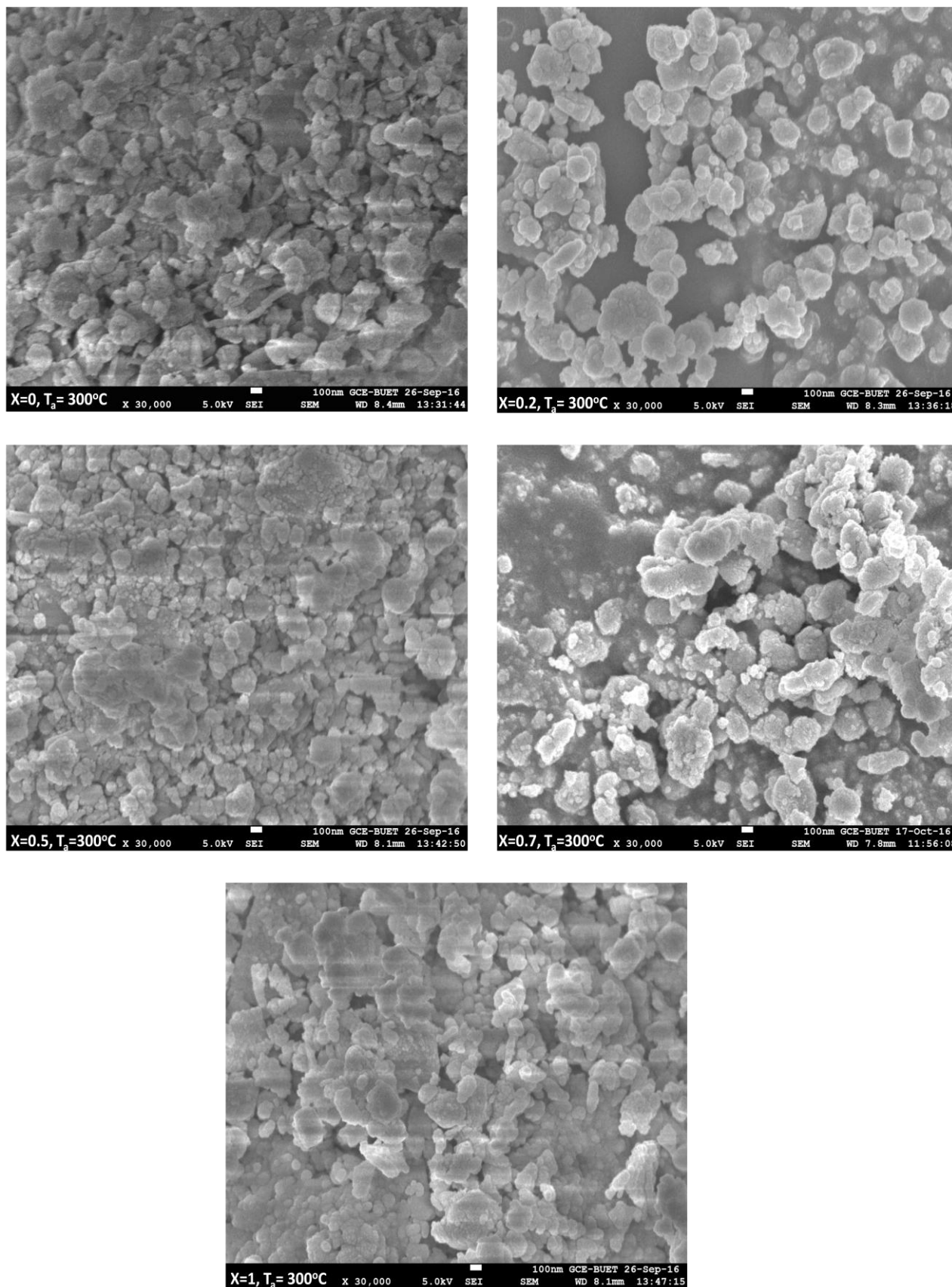


Figure 4.7: FESEM micrographs of $(1-x) \text{BiFe}_{0.9}\text{La}_{0.1}\text{O}_3 + x\text{Ni}_{0.6}\text{Zn}_{0.4}\text{Fe}_{0.94}\text{V}_{0.06}\text{O}_4$ for $x = 0, 0.2, 0.5, 0.7$ and at 300°C annealing temperature

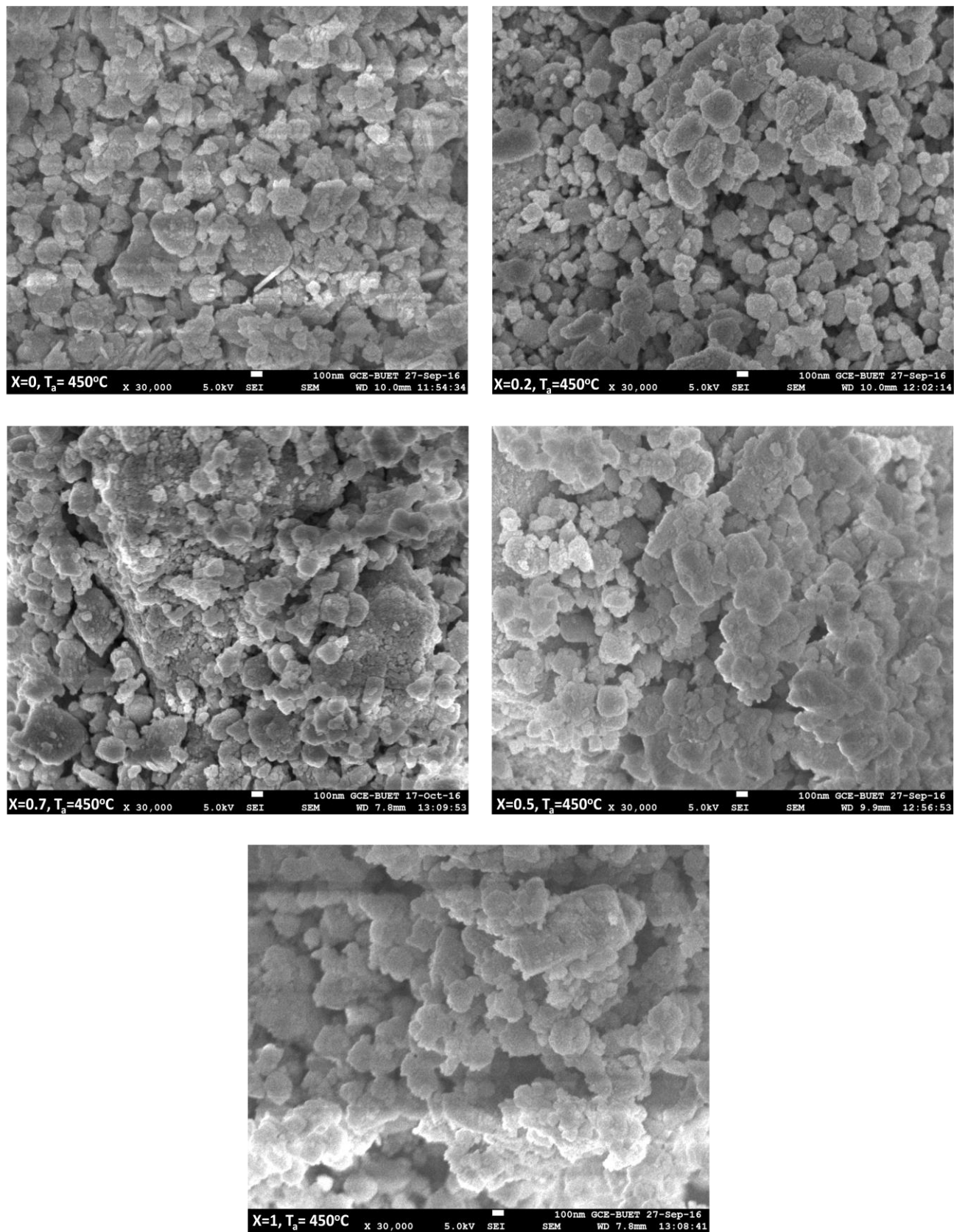


Figure 4.8: FESEM micrographs of $(1-x)\text{BiFe}_{0.9}\text{La}_{0.1}\text{O}_3 + x\text{Ni}_{0.6}\text{Zn}_{0.4}\text{Fe}_{0.94}\text{V}_{0.06}\text{O}_4$ for $x = 0, 0.2, 0.5, 0.7$ and at 450°C annealing temperature

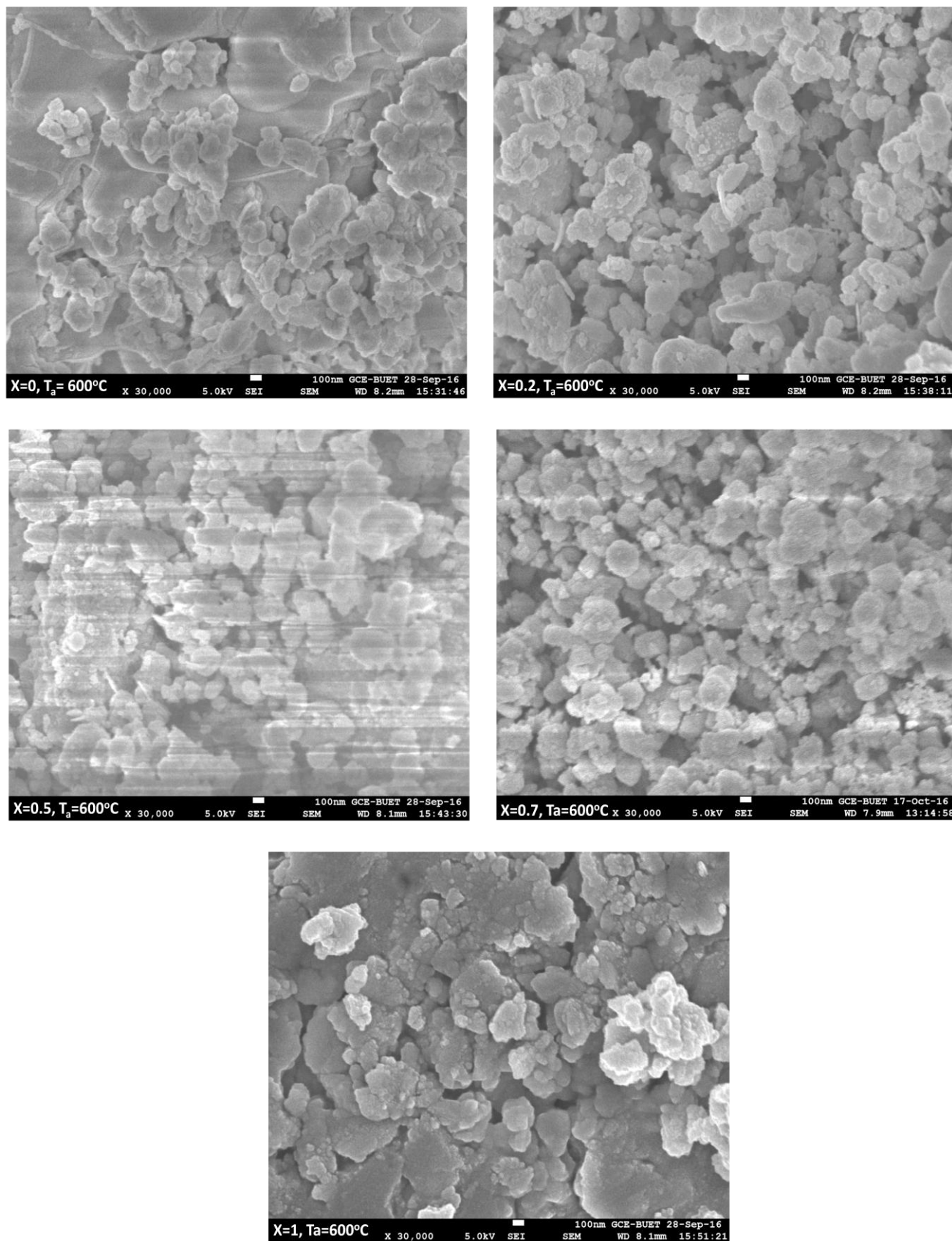


Figure 4.9: FESEM micrographs of $(1-x) \text{BiFe}_{0.9}\text{La}_{0.1}\text{O}_3 + x\text{Ni}_{0.6}\text{Zn}_{0.4}\text{Fe}_{0.94}\text{V}_{0.06}\text{O}_4$ for $x = 0, 0.2, 0.5, 0.7$ and at 600°C annealing temperature

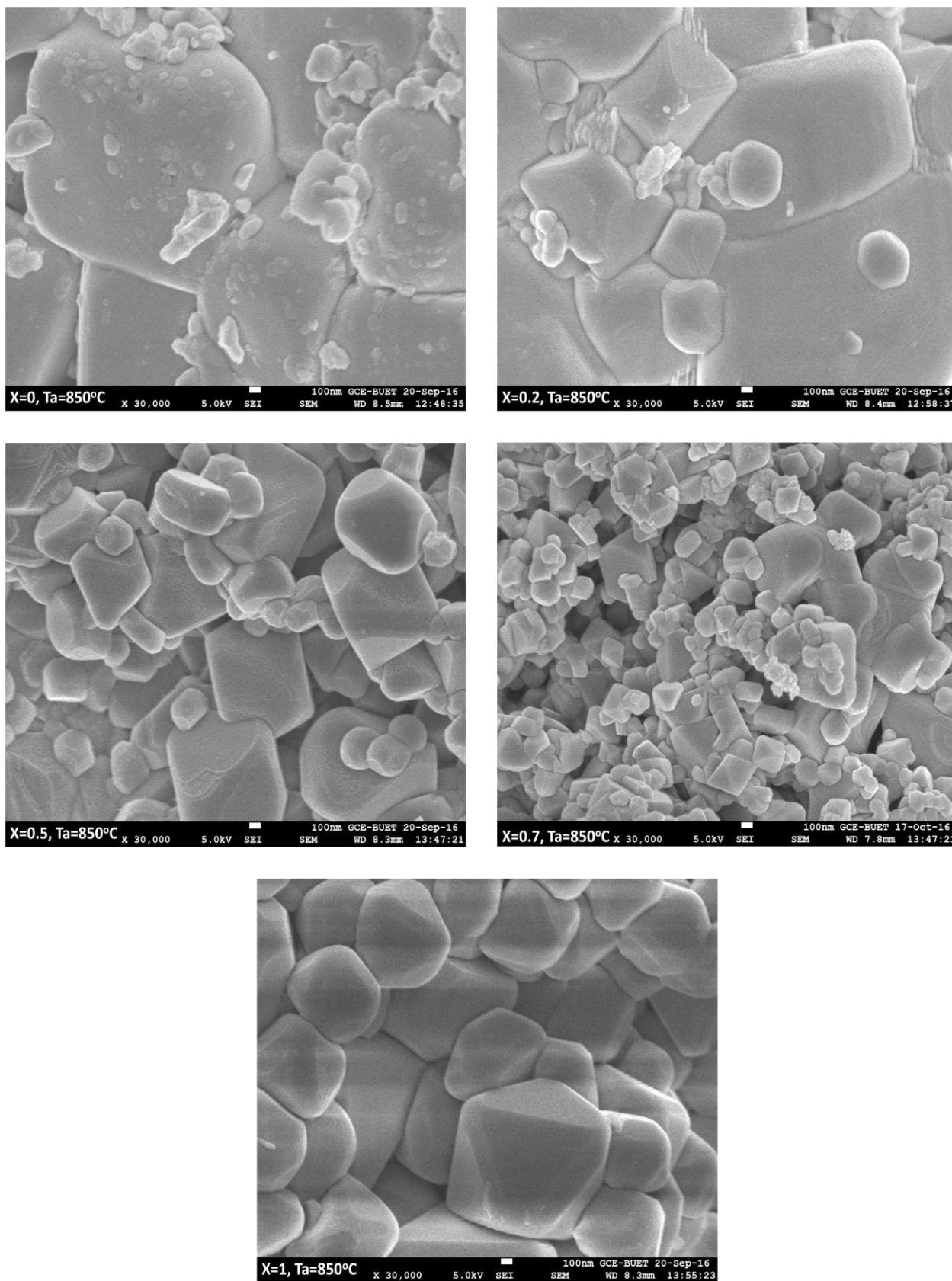


Figure 4.10: FESEM micrographs of $(1-x) \text{BiFe}_{0.9}\text{La}_{0.1}\text{O}_3 + x\text{Ni}_{0.6}\text{Zn}_{0.4}\text{Fe}_{0.94}\text{V}_{0.06}\text{O}_4$ for $x = 0, 0.2, 0.5, 0.7$ and at 850°C annealing temperature

Average grain size is decreased with increasing NZVFO content. The continuous grain growth demonstrating that the distinguish phases are interacted with each other. Though the grain boundaries are compacted and it is more defined at higher annealing temperature but there has some small intra-granular pores. The addition of NZVFO on BLFO results irregular grain shape [4.16] which may be occurred due to the filling of pores of BLFO by NZVFO nano-particles [4.16]. Though the nano-particles are no longer exist in higher temperature. At higher temperature, the NZVFO particles have tried to interconnect with BLFO particles, as a result the pores are merged between two phases.

Table 4.4: Grain size from FESEM micrographs with different annealing temperature of $(1-x) \text{BiFe}_{0.9}\text{La}_{0.1}\text{O}_3 + x\text{Ni}_{0.6}\text{Zn}_{0.4}\text{Fe}_{0.94}\text{V}_{0.06}\text{O}_4$ for $x=0, 0.2, 0.5, 0.7$

Annealing Temperature	Contents	Average Grain Size (nm)
300°C	x = 0	40
	x = 0.2	35
	x = 0.5	28
	x = 0.7	23
	x = 1	31
450°C	x = 0	80
	x = 0.2	71
	x = 0.5	62
	x = 0.7	55
	x = 1	68
600°C	x = 0	260
	x = 0.2	220
	x = 0.5	180
	x = 0.7	165
	x = 1	260
850°C	x = 0	1700
	x = 0.2	800
	x = 0.5	500
	x = 0.7	350
	x = 1	800

Particles are involving in inter-particle mass transportation for that reason the grain boundary is formed and the bimodal diffusion dominates the grain growth. The grain boundary has diffused inside lattice due to this bimodal diffusion [4.17]. The increasing behavior of grain size with increasing annealing temperature is reported in Table 5.3 on the basis of FESEM micrographs. Due to agglomerate condition, to measure the grain size is a tough job, though it is done by linear intercept method. According to linear intercept method the measurement of grain size may not accurate. As annealing temperature increased the sharp grain boundaries are visible. For $T_a = 850^\circ\text{C}$, all grain boundaries can observe easily because there has no agglomeration.

4.3 Measurement of Magnetization

4.3.1 Measurement of Ferromagnetic Effect on Multiferroic Magnetization (1-x) $\text{BiFe}_{0.9}\text{La}_{0.1}\text{O}_3 + x\text{Ni}_{0.6}\text{Zn}_{0.4}\text{Fe}_{0.94}\text{V}_{0.06}\text{O}_4$ Composites

The magnetization curve was taken by using Vibration Sample Magnetometer (VSM) of Atomic Energy Centre, Dhaka. All samples were sintered at 850°C and the VSM data was taken at room temperature where pallet shaped samples were taken in this experiment. To know the ferromagnetic effect on multiferroic composites, the full cycle of magnetization has obtained. In general BLFO shows weak ferromagnetic effect at room temperature [4.6]. Naturally BFO has antiferromagnetic property which posses very few and unusual ferromagnetic behavior [4.18]. The magnetic moments of Fe^{3+} cations linked with ferromagnetically in pseudo cubic (111) planes and antiferromagnetically between adjacent planes, which are bordered by six O^{2-} ions in the ordinary vertex of two adjacent FeO_6 octahedral [4.19]. The weak magnetization of bismuth ferrite (BFO) is caused by antiferromagnetic order along $[001]_h$ direction. The magnetoelectric effect of BFO strongly constrained by a sinusoidal spin structure along $[110]_h$ direction which cancels out the macroscopic magnetization. Addition of rare earth content on BFO improves the magnetism by restraining the spin-cycloid structure and the ferroelectricity improve by enhancing compositional steadiness [4.20 - 4.23].

After adding La^{3+} on BiFeO_3 , new magnetic interactions are developed such as La-La and La-Fe instead of Fe-Fe interaction. Due to this new type of magnetic

interactions, a disturbance has been established and leads a spectacular change in the M-H loops [4.24]. The change in structural property of BLFO from rhombohedral to orthorhombic, results in a modification on the modulated spiral spins [4.25]. The addition of La ion improves ferromagnetic properties of BFO [63_BP]. Literature shows that, the initial attachment of La content ($x = 0.05$) provides weak magnetization as La reduces the Fe^{2+} and oxygen vacancies but further increase in La concentration at ($x = 0.10, 0.15$) improves the magnetization as the spin-modeling structure is gradually censored by La doping [4.26]. Figure 4.11 shows that, the magnetization of BLFO for $x = 0$ is too low which also give in precise form in Figure 5.12. From Figure 4.12 it is seen that the magnetization of BLFO is poor with compared other contents which are having NZVFO. The saturation magnetization of BLFO is 0.13311emu/gm and the coercivity is 238.67 T. On the other hand Ni-Zn content shows a strong ferromagnetic property which is one of major reason to choose it for preparing multiferroic composites.

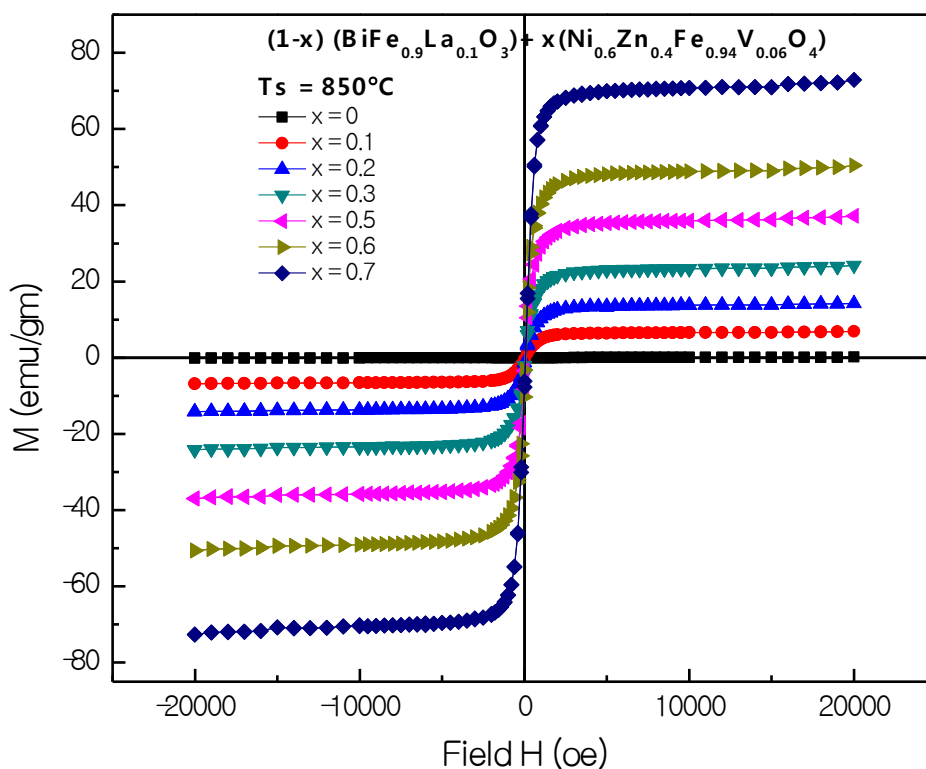


Figure 4.11: Magnetization M-H curve of $(1-x) \text{BiFe}_{0.9}\text{La}_{0.1}\text{O}_3 + x\text{Ni}_{0.6}\text{Zn}_{0.4}\text{Fe}_{0.94}\text{V}_{0.06}\text{O}_4$ at 850°C sintering temperature

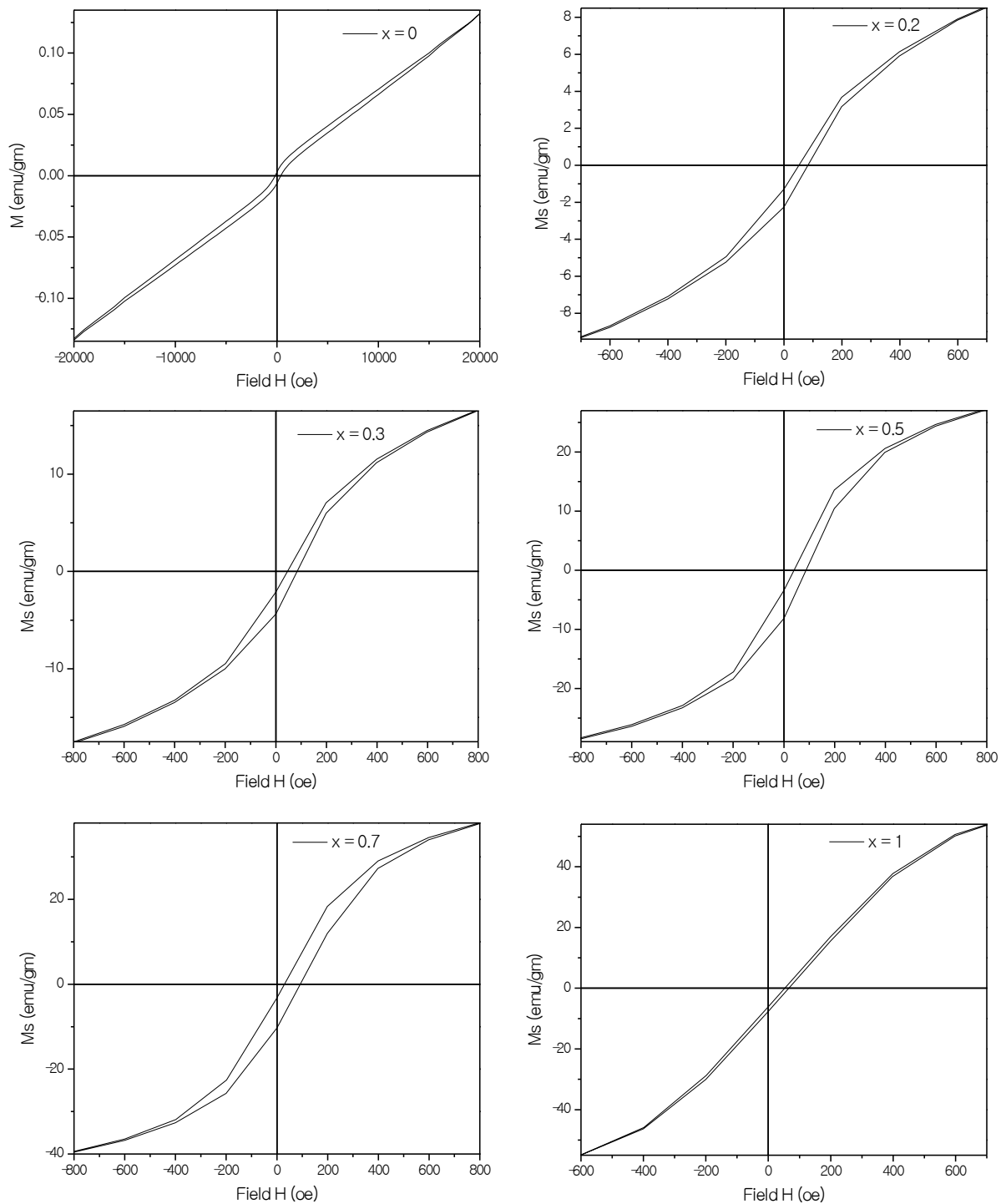


Figure 4.12: Broadening of Magnetization M-H curve of $(1-x) \text{BiFe}_{0.9}\text{La}_{0.1}\text{O}_3 + x\text{Ni}_{0.6}\text{Zn}_{0.4}\text{Fe}_{0.94}\text{V}_{0.06}\text{O}_4$ for $x = 0, 0.2, 0.3, 0.5, 0.7, 1$ at 850°C sintering temperature

Nickel doped zinc has high value of saturation magnetization and high magnetostriction coefficient [4.15]. Nickel zinc has mixed spinel structure (AB_2O_4) and exhibits soft magnetic properties due to unpaired electrons which may align in the presence of applied magnetic field [4.15]. But Ni-Zn has high electrical resistivity. So the combination of ferroelectric and ferromagnetic material can improve the quality of multiferroic. From Figure 4.11, it is seen that the increasing in NZVFO content with BLFO enhances the magnetization of the composites. After substituting little amount of NZVFO with BLFO, the magnetization incredibly increased and further increase in NZVFO contributes on improving the magnetization. The role of increasing magnetization with NZVFO content is clearly illustrated in Figure 4.11.

The hysteresis loop shifted towards right direction with increasing NZVFO content. The shift in hysteresis loop from its origin point is known as exchange bias effect. The exchange-bias effect refers to a shift H_{EB} of the magnetization curve due to antiferromagnetic–ferromagnetic exchange coupling [4.27]. It is maximum for magnetic fields applied along the induced pinning direction and vanishes perpendicular to it, where it contributes to an enhanced total anisotropy field HK_{tot} . Exchange biasing is well established in read-head technology based on anisotropic, giant or tunnel magnetoresistive effects. The introduction of exchange-bias effect has also been suggested for magnetoelectric read-heads [4.28]. However, in contrast to magnetoresistive sensors, where strong pinning of thin ferromagnetic layers with thicknesses in the nanometre range is required, magnetoelectric composites need moderate and precise biasing of magnetostrictive layers holding thicknesses of several micrometers [4.29].

Table 4.5: Saturation Magnetization and coercivity of $(1-x) BiFe_{0.9}La_{0.1}O_3 + xNi_{0.6}Zn_{0.4}Fe_{0.94}V_{0.06}O_4$ for $x = 0, 0.2, 0.3, 0.5, 0.7, 1$ at $850^\circ C$ sintering temperature

Contents x	Saturation Magnetizaion M_s (emu/gm)	Coercivity H_c (Oe)	Anisotropy
0	0.13311	238.67	15.88
0.1	6.85925	38.43	131.80
0.2	14.22353	32.57	231.63
0.3	24.20382	38.46	465.44
0.5	37.12102	47.258	877.13
0.7	50.53846	62.26	1573.26
1	72.77483	13.61	495.23

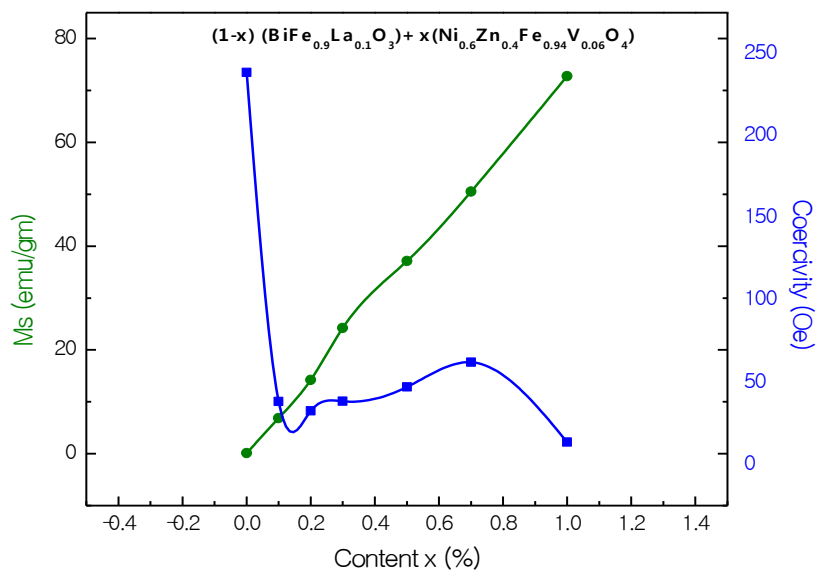


Figure 4.13: Relation between saturation magnetization and coercivity of $(1-x) \text{BiFe}_{0.9}\text{La}_{0.1}\text{O}_3 + x\text{Ni}_{0.6}\text{Zn}_{0.4}\text{Fe}_{0.94}\text{V}_{0.06}\text{O}_4$ for $x = 0, 0.1, 0.2, 0.3, 0.5, 0.7, 1$ at 850°C sintering temperature

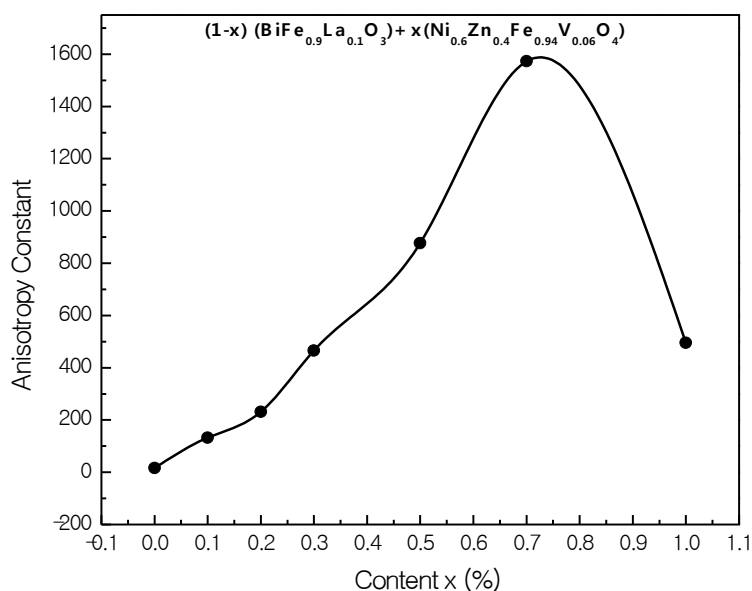


Figure 4.14: Anisotropy constant of $(1-x) \text{BiFe}_{0.9}\text{La}_{0.1}\text{O}_3 + x\text{Ni}_{0.6}\text{Zn}_{0.4}\text{Fe}_{0.94}\text{V}_{0.06}\text{O}_4$ for $x = 0, 0.1, 0.2, 0.3, 0.5, 0.7, 1$ at 850°C sintering temperature

The value saturation magnetization and coercivity for all the prepared samples are given in Table 5.4. According to Brown's relation [4.30] H_c is inversely proportional to M_s , which is given by

$$H_c \geq \frac{2\kappa_1}{\mu' M_s} \quad (4.1)$$

The equation implies that, as saturation magnetization increases then the coercivity is decreased [4.30]. So the Table 4.4 and the M-H curves are agreed with Brown's relation. The variation in anisotropy constant is given in Figure 4.14. The anisotropy constant increases upto $x = 0.7$ and afterthen it decreased.

4.3.2 Temperature Dependence Magnetization

The temperature dependent of magnetization has been determined by Vibration Sample Magnetometer (VSM) from Bose Institute, Kolkata, India. Full cycle heating and cooling technique was applied to determine the temperature dependent magnetization. The temperature dependence magnetization was taken for $x = 0$ and 1 contents at 5 (kOe) applied field. From the Figure 4.15 it is observed that, with increasing temperature the magnetization is decreased.

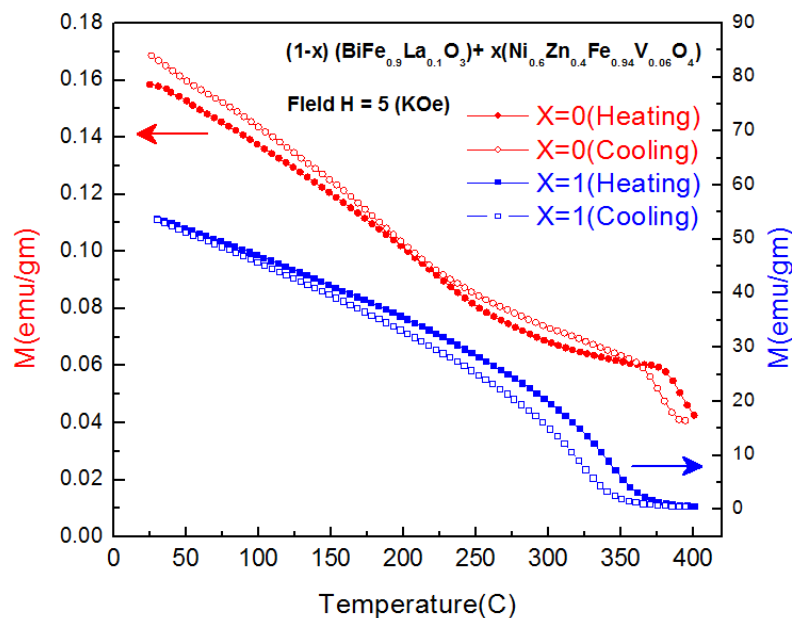


Figure 4.15: Temperature dependent magnetization of $(1-x) \text{BiFe}_{0.9}\text{La}_{0.1}\text{O}_3 + x\text{Ni}_{0.6}\text{Zn}_{0.4}\text{Fe}_{0.94}\text{V}_{0.06}\text{O}_4$ for $x = 0$, and 1

4.4 Study the frequency dependent of Permeability, Complex permeability and loss tangent

The frequency dependent real part of permeability for $(1-x) \text{BiFe}_{0.9}\text{La}_{0.1}\text{O}_3 + x\text{Ni}_{0.6}\text{Zn}_{0.4}\text{Fe}_{0.94}\text{V}_{0.06}\text{O}_4$, where $x = 0, 0.1, 0.2, 0.3, 0.5, 0.7, 1$ at 850°C sintering temperature are given in Figure 5.16. From the figure it is pointed out that the real part of permeability of NZVFO is higher than others contents having BLFO. Typically BLFO is known as ferroelectric material which contribution on magnetic properties is not higher in comparison with NZVFO. The magnetic permeability of polycrystalline ferrite depends on the grain size [4.31]. The increasing in grain size involves increasing in permeability. In this experiment the variation of vanadium content didn't applied because of taking optimum value of NZVFO. In the optimum sample of NZVFO, the grain boundary is dominated due to vanadium content as it has low melting point which dominates the sintering mechanism.

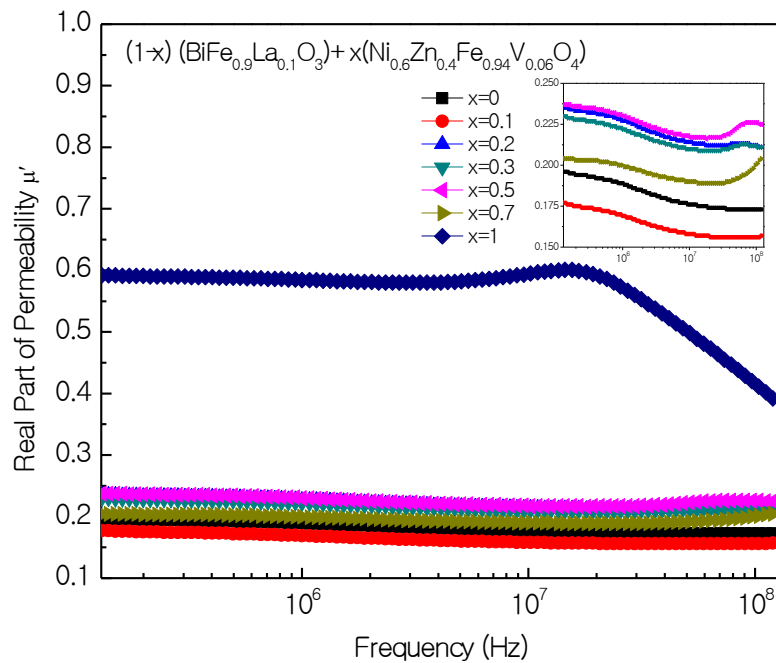


Figure 4.16: Frequency dependent real part of permeability of $(1-x) \text{BiFe}_{0.9}\text{La}_{0.1}\text{O}_3 + x\text{Ni}_{0.6}\text{Zn}_{0.4}\text{Fe}_{0.94}\text{V}_{0.06}\text{O}_4$, where $x = 0, 0.1, 0.2, 0.3, 0.5, 0.7, 1$ at 850°C sintering temperature

From the microstructures of Figure 4.10, the grain size is decreasing with increasing NZVFO content instead of BLFO content which may be occurred due to physical strain but in the case of pure NZVFO content the grain size rearranged. As a

result the permeability has been attributed due the effect of ferromagnetic properties of NZVFO. The addition of V^{5+} ion provides two Fe^{2+} ions to balance the charge which increases the $[Fe^{2+}]/[Fe^{3+}]$ ratio. Increasing in Fe^{2+} ions the permeability [4.31] has increased. For $x = 0.5$, the optimum condition of permeability has been achieved due the equal participation of ferromagnetic and ferroelectric contents in multiferroic composites. The increase in permeability is resulted to increase in magnetic properties [4.32] which also collinear with magnetization discussed in above section. The magnetization of the multiferroic composites it higher for NZVFO that indicates, permeability would be higher for NZVFO. Results confirm that the permeability and magnetization are correlated.

All ferrites materials reveal a ferromagnetic (or spin) resonance frequency at which the permeability drops to a low value and a peak is generated which refers magnetic losses. Snoek's law is a better argument to describe this phenomenon which states that, at lower frequency region the multiplication between initial frequency and ferromagnetic resonance is approximately constant [4.33]. So the higher value of permeability has low cut-off frequency and for practical purpose it is very essential to keep low losses at higher frequencies.

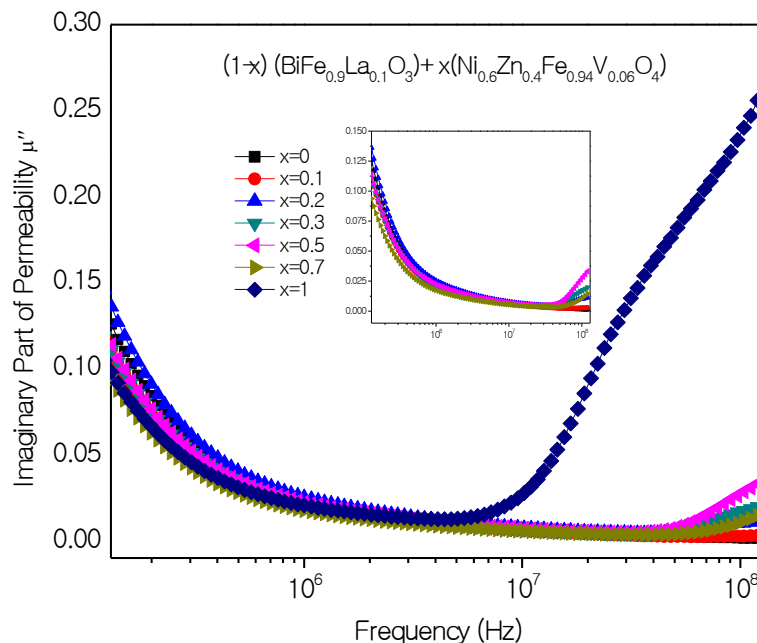


Figure 4.17: Frequency dependent Imaginary Part of Permeability of $(1-x) BiFe_{0.9}La_{0.1}O_3 + xNi_{0.6}Zn_{0.4}Fe_{0.94}V_{0.06}O_4$, where $x = 0, 0.1, 0.2, 0.3, 0.5, 0.7, 1$ at $850^\circ C$ sintering temperature

The frequency dependent imaginary part of permeability of BLFO-NZVFO multiferroic composites is given in Figure 5.17 where the permeability is decreased in higher frequency except for $x = 1$ which is pure NZVFO content. The outstanding stability of permeability happens in the region of higher frequency which is a good deal for industrial application. In the case of pure NZVFO the imaginary permeability is decreased at higher frequencies but after 65 MHz its increases with increasing frequency.

The magnetic loss in higher frequency may be initiated from natural ferromagnetic resonance [4.32]. After adding La content the H_c is increasing due to the amplification of exchange interaction which contributes on improving the anisotropy field intensity and exchange interaction field intensity [4.32]. The addition of La content makes stronger of ferromagnetic resonance which leads a little improvement of magnetization of BLFO.

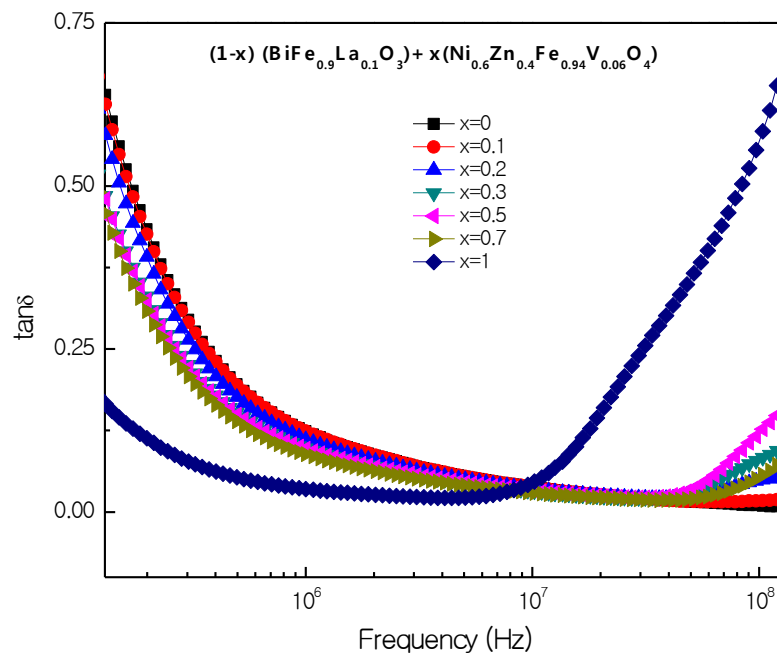


Figure 4.18: Frequency dependent Loss tangent of $(1-x) \text{BiFe}_{0.9}\text{La}_{0.1}\text{O}_3 + x\text{Ni}_{0.6}\text{Zn}_{0.4}\text{Fe}_{0.94}\text{V}_{0.06}\text{O}_4$, where $x = 0, 0.1, 0.2, 0.3, 0.5, 0.7, 1$ at 850°C sintering temperature

By increasing NZVFO content the frequency dependent relative quality factor (RQF) is increased of BLFO-NZVFO multiferroic composites. A resonance peak is formed with adding NZVFO content with BLFO where the peak shifted towards lower frequency. The shifting in permeability and RQF peaks towards the lower

frequency with the addition of NZVFO could be described by Snoek's law [4.34], [4.35]. As mentioned above, according to Snoek's law, the increasing in saturation magnetization leads to decrease in the resonance frequency and vice versa [4.36]. So at the cutoff frequency, the decrease in loss tangent may provide a progressive value of permeability.

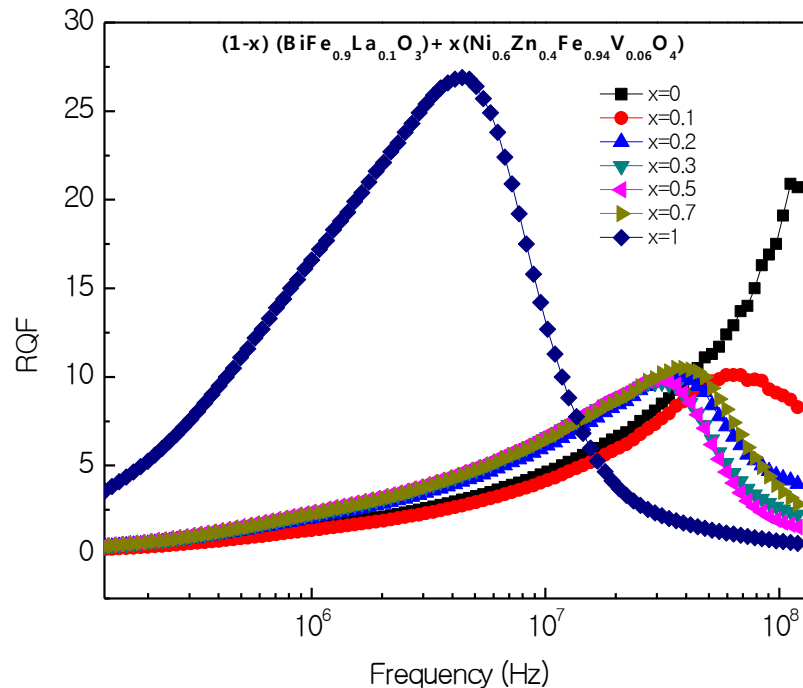


Figure 4.19: Frequency dependent Loss tangent of $(1-x) \text{BiFe}_{0.9}\text{La}_{0.1}\text{O}_3 + x\text{Ni}_{0.6}\text{Zn}_{0.4}\text{Fe}_{0.94}\text{V}_{0.06}\text{O}_4$, where $x = 0, 0.1, 0.2, 0.3, 0.5, 0.7, 1$ at 850°C sintering temperature

4.5 Measurement of Ferroelectric Properties of Multiferroic Composites

Figure 4.20 represents frequency dependent dielectric constant. Measurement of dielectric constant is very important for multiferroic composites. Dielectric constant roles major part on magnetoelectric coupling. Without strong value of ferroelectricity it's not possible to organize magnetoelectric coupling in multiferroic composites. Frequency dependent dielectric constant of pallet samples sintered at 850°C has been taken by Weine Kerr Impedance analyzer of Department of Physics,

Bangladesh University of Engineering and Technology (BUET). In the present work La^{3+} was substituted in B site instead of Fe^{3+} but in many literatures La^{3+} substituted in A site instead of Bi^{3+} . The substitution of La^{3+} on B site may give better treatment of dielectric properties because here La-Fe and La-La charge distribution would be raised as the replacement of Fe-Fe interaction. In some literatures it is mentioned that the 5% addition of La^{3+} leads to decrease in dielectric constant but 10-15% doping of La^{3+} content improves the dielectric properties [4.37]. So due to this reason, in the present work 10% doping of La^{3+} had chosen.

One the other hand, the valence instability of Fe^{3+} ions to Fe^{2+} ions of BiFeO_3 is resulted by the digression from oxygen stoichiometry. In the case of typical sintering process of BiFeO_3 , slow heating rate and long sintering time of higher sintering temperature produces high oxygen vacancy concentration which is proposed by Wang [4.39]. The non-ferroelectricity is resulted by these higher oxygen vacancies [4.40]. In this experiment the sintering temperature was 850°C with $5^\circ\text{C}/\text{min}$ heating rate where the sintering temperature stayed for 3 hours. The sintered samples were cooled in furnace after just shutting down it where had no external effect applied to cool it. So the fluctuation in Fe ions results high conductivity as evidenced by high dielectric constant [4.40].

In Figure 5.20, the dielectric constant of BLFO ($x = 0$) is maximum as with compared pure NZVFO and mixed composites. The combination of Nickel and Zinc generally populated as ferromagnetic material which is not able to provide large value of dielectric constant. In ferrite (AB_2O_4) contents, the dielectric properties can be explained in association with dielectric polarization which is also similar with electrical conduction [4.41]. Hence space charge polarization largely arbitrated by the movement of available free space charge carriers which results the dispersion in real and imaginary dielectric constant and loss tangent of the multiferroic composites [4.41]. This space charge (exist in grain boundaries) relaxation is key tool to describe the decreasing phenomenon of dielectric constant at higher frequencies. Defects dipoles are formed by these space charges and the applied lower frequencies field is can be followed by it. In the case of higher frequencies the need to construct and go through the relaxation but the time of relaxation may not sufficient [4.42]. The dispersion of dielectric constant and loss tangent in lower frequency regime may be

recognized to interfacial polarization (space charge polarization, Maxwell Wagner, long range structural order and defect relaxations) [4.37-4.38].

One the other hand, the valence instability of Fe^{3+} ions to Fe^{2+} ions of BiFeO_3 is resulted by the digression from oxygen stoichiometry. In the case of typical sintering process of BiFeO_3 , slow heating rate and long sintering time of higher sintering temperature produces high oxygen vacancy concentration which is proposed by Wang [4.39]. The non-ferroelectricity is resulted by these higher oxygen vacancies [4.40]. In this experiment the sintering temperature was 850°C with $5^\circ\text{C}/\text{min}$ heating rate where the sintering temperature stayed for 3 hours. The sintered samples were cooled in furnace after just shutting down it where had no external effect applied to cool it. So the fluctuation in Fe ions results high conductivity as evidenced by high dielectric constant [4.40].

In Figure 4.20, the dielectric constant of BLFO ($x = 0$) is maximum as with compared pure NZVFO and mixed composites. The combination of Nickel and Zinc generally populated as ferromagnetic material which is not able to provide large value of dielectric constant. In ferrite (AB_2O_4) contents, the dielectric properties can be explained in association with dielectric polarization which is also similar with electrical conduction [4.41]. Hence space charge polarization largely arbitrated by the movement of available free space charge carriers which results the dispersion in real and imaginary dielectric constant and loss tangent of the multiferroic composites [4.41].

This space charge (exist in grain boundaries) relaxation is key tool to describe the decreasing phenomenon of dielectric constant at higher frequencies. Defects dipoles are formed by these space charges and the applied lower frequencies field is can be followed by it. In the case of higher frequencies the need to construct and go through the relaxation but the time of relaxation may not sufficient [4.42]. The dispersion of dielectric constant and loss tangent in lower frequency regime may be recognized to interfacial polarization (space charge polarization, Maxwell Wagner, long range structural order and defect relaxations) [4.37].

With the help of number of available Fe^{2+} ions in the octahedral site, the dielectric behavior is explicated. The local displacement of electrons resulted by the electronic exchange of $\text{Fe}^{2+} \Leftrightarrow \text{Fe}^{3+}$. The electronic polarization is determined by this local displacement of electrons which also correlated with dielectric constant of ferrite

[4.43 - 4.44]. The addition of vanadium (V^{5+}) ions in octahedral site of NZVFO (B site) contributes on modifying microstructure as it is likely to enter in lattice sites. As the pentavalent ions entered in lattice sites, it changes the valance state of octahedral Fe sites and delivering more Fe^{2+} ions to maintain the charge balance [4.45]. So the addition of vanadium decreases the dielectric constant of Nickel Zinc content [4.46].

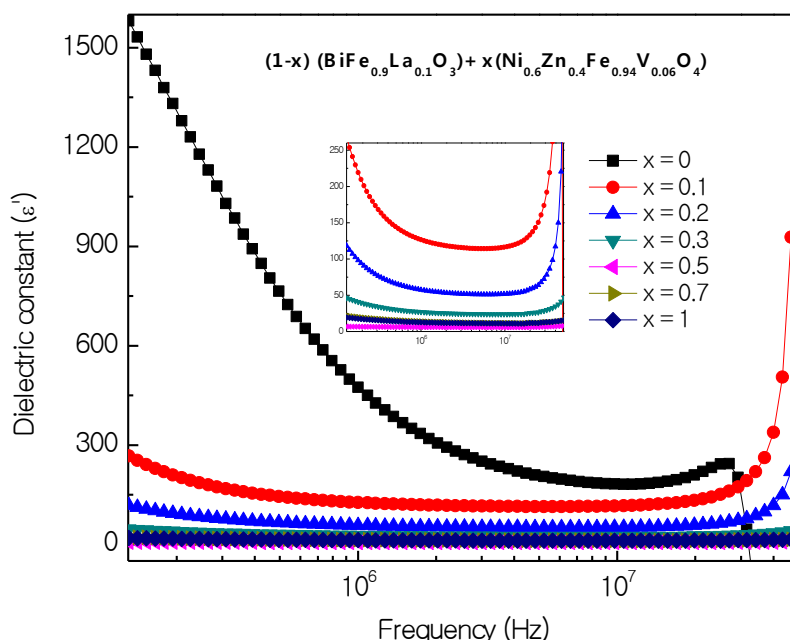


Figure 4.20: Frequency dependent Dielectric Constant of $(1-x) BiFe_{0.9}La_{0.1}O_3 + xNi_{0.6}Zn_{0.4}Fe_{0.94}V_{0.06}O_4$, where $x = 0, 0.1, 0.2, 0.3, 0.5, 0.7, 1$ at $850^\circ C$ sintering temperature

Koop's two layer model and Maxwell-Wagner polarization theory are the successive way to describe the dielectric dispersion. In the case of frequency dependent dielectric constant of ferrite material, Koop's model [4.47] suggests that, the inhomogeneous dielectric structure as discussed by Maxwell [4.48] and Wagner [4.49] is helpful to understand the conducting and insulating grain boundaries. In the arrangement of inhomogeneous dielectric structure, space charge carriers are getting together where this gathering needs a certain time to line up their axes parallel to an alternating electric field. This time deletion involves decreasing in dielectric constant [4.46].

The real part of dielectric constant is decreased at higher value of frequency where low value of frequency gives large dielectric constant. The dielectric constant

follows Debye law of frequency dispersion which states that, dielectric constant remains comparatively constant at high frequencies and increased at low frequency [4.50].

The imaginary part of dielectric constant of $(1-x) \text{BiFe}_{0.9}\text{La}_{0.1}\text{O}_3 + x\text{Ni}_{0.6}\text{Zn}_{0.4}\text{Fe}_{0.94}\text{V}_{0.06}\text{O}_4$ where $x = 0, 0.1, 0.2, 0.3, 0.5, 0.7, 1$ at 850°C sintering temperature are illustrated in Figure 5.20. From the figure it is seen that, the dielectric constant of BLFO is higher than of NZVFO which also collinear with real part of dielectric constant as described above. At the region of 20 kHz, a sudden peak is seen for BLFO which may be attributed due to the distortion in space charge distribution.

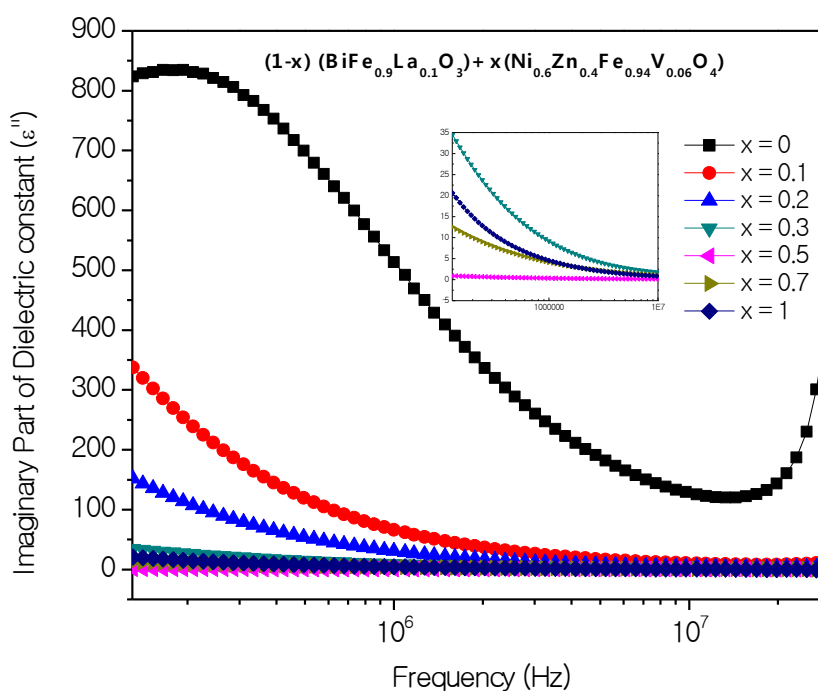


Figure 4.21: Frequency dependent Imaginary Part of Dielectric Constant of $(1-x) \text{BiFe}_{0.9}\text{La}_{0.1}\text{O}_3 + x\text{Ni}_{0.6}\text{Zn}_{0.4}\text{Fe}_{0.94}\text{V}_{0.06}\text{O}_4$, where $x = 0, 0.1, 0.2, 0.3, 0.5, 0.7, 1$ at 850°C sintering temperature

The potential barriers have double ionized oxygen ion vacancies and it provides hopping motion which is responsible for the relaxation peak of loss tangent of BLFO at low frequencies. The dielectric constant decreases as decreased BLFO and increased of NZVFO. BLFO has ferroelectricity so the decrease in BLFO content obviously resulted to decrease in dielectric properties of the composites. As dielectric properties decreased with decreasing BLFO from BLFO-NZVFO multiferroic composites, the loss tangent also decreased. The dispersion at lower frequencies of

loss tangent also is explained by the space charge polarization described above. The dielectric loss tangent of BLFO behaves reversely with NZVFO content. At lower frequency the loss tangent of BLFO tends to increase up to maximum value, which refers the higher loss of ferroelectric properties with the increasing of frequency. At higher frequencies, the dielectric loss tangent of BLFO is decreasing which also true for NZVFO content.

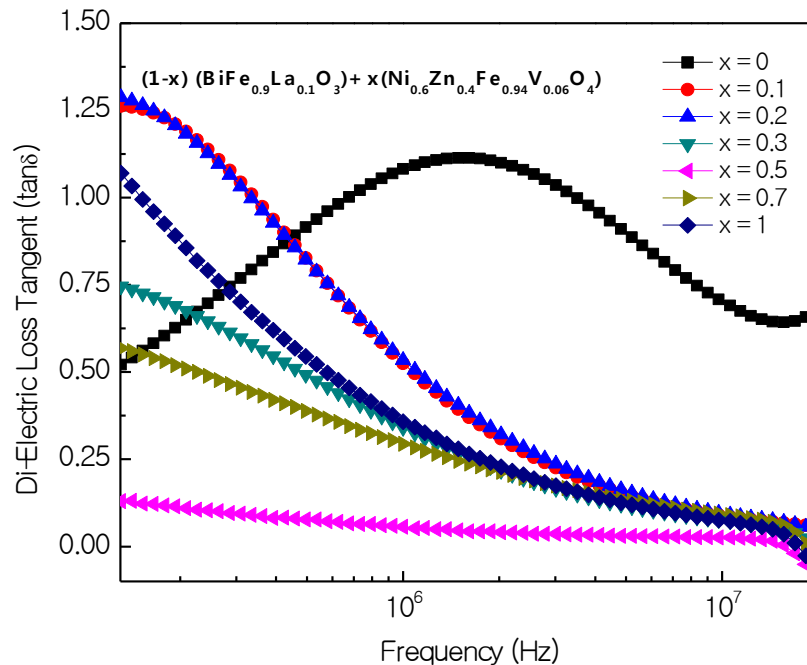


Figure 4.22: Frequency dependent Di-electric Loss tangent of $(1-x) \text{BiFe}_{0.9}\text{La}_{0.1}\text{O}_3 + x\text{Ni}_{0.6}\text{Zn}_{0.4}\text{Fe}_{0.94}\text{V}_{0.06}\text{O}_4$, where $x = 0, 0.1, 0.2, 0.3, 0.5, 0.7, 1$ at 850°C sintering temperature

For $x = 0.1$ and 0.2 , the dielectric loss tangents seems like same which are decreased with increasing NZVFO content. But for $x = 0.5$ where both BLFO and NZVFO are equal in quantity inside the samples, has lowest value of loss tangent. This is also true for both of real and imaginary dielectric constant where the minimum value of these are occurring at 50:50 of BLFO : NZVFO. The mechanism of having lowest value of dielectric constant and loss tangent for 50:50 of BLFO : NZVFO may be characterized for the well chemical balance between two interstitial sites which resulted due to effective locking of maximum number of charge carriers from conduction [4.51].

From Figure 4.23 it is seen that the specific resistivity of the BLFO-NZVFO multiferroic composites is maximum for $x = 1$ which is fully ferromagnetic NZVFO content and lowest for $x = 0$ which stands for pure ferroelectric BLFO content. Interestingly, the value of specific resistivity is optimized for $x = 0.5$ where the ratio between BLFO and NZVFO content is 50:50. As described above it is clearly found that the contribution of conduction and dielectric properties of NZVFO is lower than of BLFO which may be described with the help of resistivity. If resistivity is increasing then the conduction decreased. The resistivity of multiferroic composite has decreased with the increasing frequency.

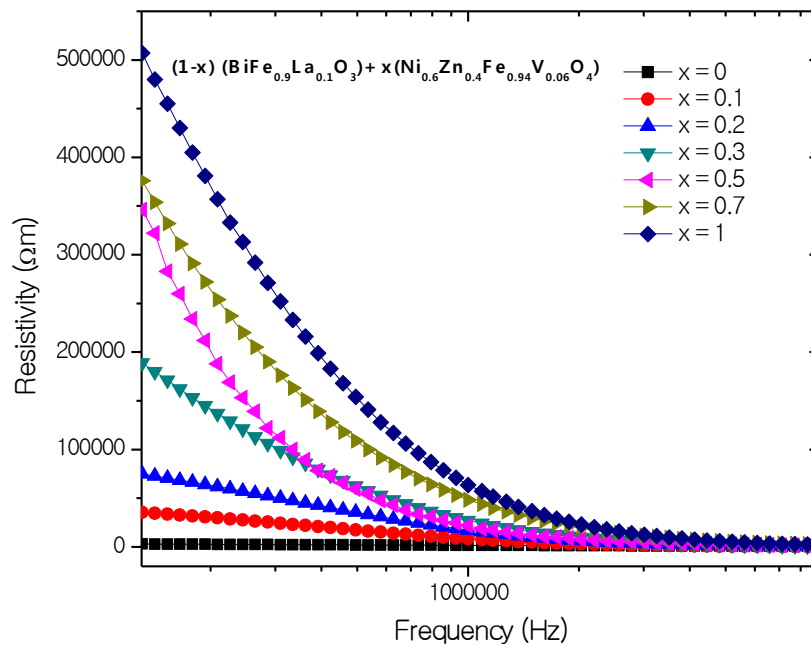


Figure 4.23: Frequency dependent specific resistivity of $(1-x) \text{BiFe}_{0.9}\text{La}_{0.1}\text{O}_3 + x\text{Ni}_{0.6}\text{Zn}_{0.4}\text{Fe}_{0.94}\text{V}_{0.06}\text{O}_4$, where $x = 0, 0.1, 0.2, 0.3, 0.5, 0.7, 1$ at 850°C sintering temperature

The motivation of the thesis was to obtain optimum compositions where both of ferroelectric and ferromagnetic orders contribute on developing successful multiferroic material. From this research, it could be conclude that, it is not possible to provide strong multiferroic parameters by a single ferroic ordered material. In the case of BLFO content, the dielectric properties were improved by adding La content. BLFO shows a good agreement with higher value of dielectric parameters and the resistivity was minimized due to BLFO. On the other hand, the addition of vanadium

content improves the magnetization of Ni-Zn ferrite which also known as a better ferromagnetic material. So the combination of BLFO as ferroelectric content and NZVFO as ferromagnetic content are contributing to form useful multiferroic parameters. But reality is that, all compositions are not good enough to build a super multiferroic material which can apply in different electronics goods.

Table 4.6: The comparison between Permeability, Magnetic Loss Tangent, Dielectric Constant, Dielectric Constant, Resistivity, Dielectric Loss Tangent of $(1-x) \text{BiFe}_{0.9}\text{La}_{0.1}\text{O}_3 + x\text{Ni}_{0.6}\text{Zn}_{0.4}\text{Fe}_{0.94}\text{V}_{0.06}\text{O}_4$, where $x = 0, 0.1, 0.2, 0.3, 0.5, 0.7, 1$ at 850°C sintering temperature

Content x	Permeability	Magnetic Loss Tangent	Dielectric Constant	Resistivity	Dielectric Loss Tangent
0	0.05829	0.00305	3426.78	119215.72	0.30733
0.1	-0.03963	0.00289	2107.50	197886.09	0.17116
0.2	0.04723	0.00277	1160.45	420244.9	0.21657
0.3	0.16822	0.01207	278.49	2.40×10^6	0.30987
0.5	0.15794	14.29844	12.55	5.71×10^7	0.33828
0.7	0.11751	11.80916	97.64	9.02×10^6	0.41231
1	0.48636	0.04027	448.84	2.53×10^6	1.61118

Table 4.6, demonstrated with different values of Permeability, Magnetic Loss Tangent, Dielectric Constant, Dielectric Constant, Resistivity, Dielectric Loss Tangent of $(1-x) \text{BiFe}_{0.9}\text{La}_{0.1}\text{O}_3 + x\text{Ni}_{0.6}\text{Zn}_{0.4}\text{Fe}_{0.94}\text{V}_{0.06}\text{O}_4$, where $x = 0, 0.1, 0.2, 0.3, 0.5, 0.7, 1$ at 850°C sintering temperature for 1KHz frequency. From Figure 4.24 and 4.25, the optimum samples with respect to ferroelectric and ferromagnetic properties can be obtained. It is observed that, for $x = 20$ to 30 , both of permeability and dielectric constant are almost optimized. This is also true for the losses of dielectric and permeability.

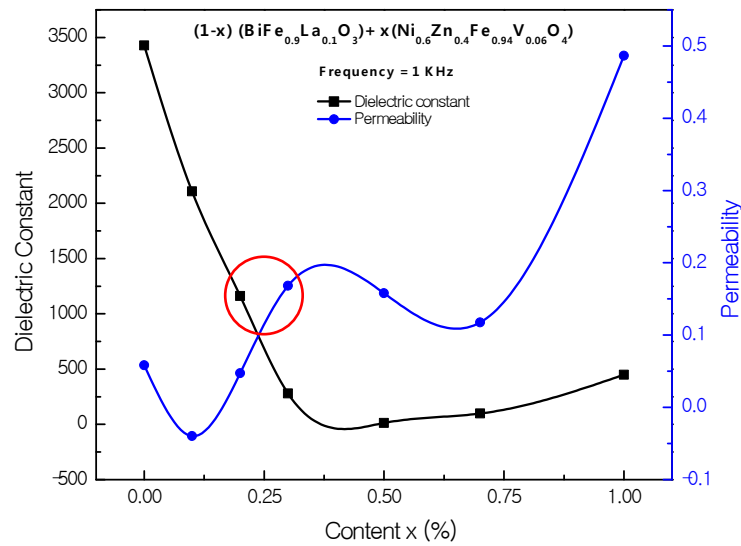


Figure 4.24: Comparison between Dielectric constant and Magnetic permeability of $(1-x) \text{BiFe}_{0.9}\text{La}_{0.1}\text{O}_3 + x\text{Ni}_{0.6}\text{Zn}_{0.4}\text{Fe}_{0.94}\text{V}_{0.06}\text{O}_4$, where $x = 0, 0.1, 0.2, 0.3, 0.5, 0.7, 1$ at 850°C sintering temperature

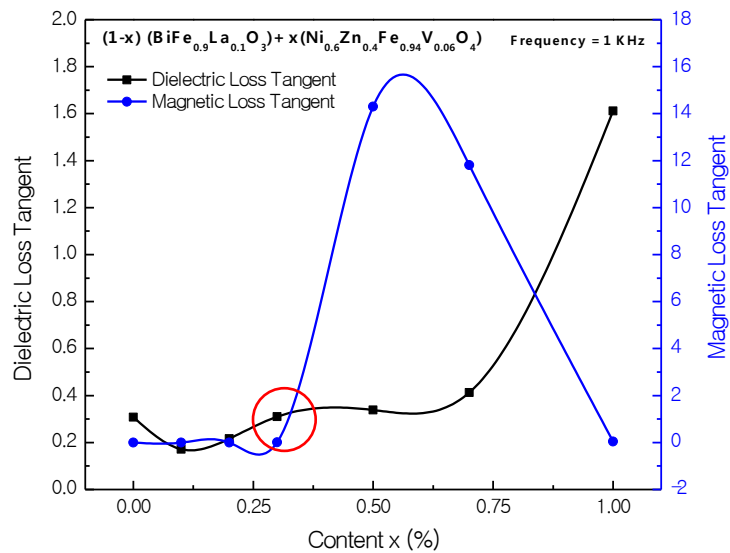


Figure 4.25: Comparison between Dielectric loss tangent and Magnetic loss tangent of $(1-x) \text{BiFe}_{0.9}\text{La}_{0.1}\text{O}_3 + x\text{Ni}_{0.6}\text{Zn}_{0.4}\text{Fe}_{0.94}\text{V}_{0.06}\text{O}_4$, where $x = 0, 0.1, 0.2, 0.3, 0.5, 0.7, 1$ at 850°C sintering temperature

CONCLUSIONS

5.1 Conclusions

The multiferroic composites $(1-x) \text{BiFe}_{0.9}\text{La}_{0.1}\text{O}_3 + x (\text{Ni}_{0.6}\text{Zn}_{0.4}\text{Fe}_{0.94}\text{V}_{0.06}\text{O}_4)$ where $x = 0, 0.1, 0.2, 0.3, 0.5, 0.7, 1$ are successfully made by the combination of solid state reaction method and mechanical techniques including magnetic stirring, ultrasonification and centrifugation. The powder samples were annealed at 300°C, 450°C, 600°C and 850°C and pallet and ring shaped samples were sintered at 850°C. Powdered samples had used in XRD and FESEM experiments, pallet were used for dielectric measurement and ring were used for permeability and magnetization measurements.

- i. The phase transition provided the distortion between rhombohedral to orthorhombic phase which has been detected for $\text{BiFe}_{0.9}\text{La}_{0.1}\text{O}_3$ (BLFO) content and cubic phase for $\text{Ni}_{0.6}\text{Zn}_{0.4}\text{Fe}_{0.94}\text{V}_{0.06}\text{O}_4$ (NZVFO) content. With increasing NZVFO content, the distortion being minimized. Lattice parameters for both perovskite and ferrite site were decreased. The pervskite and ferrite site formation also confirmed from a/c ratio.
- ii. The confirmation of nano size particles has driven by FESEM photographs where the particles average size in between 20 ~ 30 nm. The proportion of each content inside composites was found in EDX patterns which referred that the prepared samples contain exact amount of contents.
- iii. Different annealing temperatures were applied to understand the effect of heat treatment on particle size distribution and crystallization. From FESEM micrographs the effect of increasing temperature has been observed. The grain size is increased with increasing annealing temperature. At any fixed annealing temperature the grain size is of pure BLFO is larger than pure NZVFO and other mixed composites. After adding NZVFO, the average grain sizes were which may be attributed due to the variation of ionic radius of constituents.
- iv. The magnetization measurement was carried out by VSM. Magnetization is lower for BLFO content and with increasing NZVFO content, the magnetization improves. Saturation magnetization was maximum for pure NZVFO content but coercivity was minimum for it. The anisotropy constant was increased with increasing NZVFO content and became maximum for $x = 0.7$.

- v. The temperature dependent magnetization refers Curie temperature for pure perovskite and ferrite content where the increasing in temperature caused to decrease in magnetization but when the temperature was cooled then the magnetization increased which provided full cycle of hysteresis loop.
- vi. The frequency dependent permeability was increased with increasing NZVFO content whereas magnetic losses in association with loss tangent decreased.
- vii. The frequency dependent imaginary permeability and loss tangent decreased for both NZVFO and BLFO content but in the case of pure NZVFO content, the imaginary permeability and loss tangent increased at higher frequency.
- viii. The frequency dependent relative quality factor was increased but at higher frequency it decreases.
- ix. Frequency dependent dielectric constant was greater for pure BLFO content but after substituting NZVFO content, the dielectric constant decreased which was lowest for pure NZVFO content. On the other hand, the resistivity was increased with increasing NZVFO content.
- x. The addition of NZVFO causes to decrease in dielectric loss tangent. For pure BLFO, the dielectric loss was larger than other. For $x = 0.5$, the dielectric loss was minimum.
- xi. The magnetization was better for $x = 0.3 - 0.5$ and permeability and dielectric properties were provided almost similar characteristics for $x = 0.2$ to 0.3 . Both magnetic and electric losses were same in scale also for $x = 0.2$ to 0.3 . So according to these results, it can easily conclude the optimum multiferroic parameters can get from the compositions of $x \sim 0.2$ to 0.3 .

5.2 Scope for Future Work

In Bangladesh, the research of multiferroic materials is not popular due the lack of scientific interest deficiency in modern devices which are required to synthesize better multiferroic composites for different application. In recent years, government and people are talking on emerging digital Bangladesh but without contributing on hardware development it is quite impossible to reach the milestone by only improving software industry. There has no visible attempt on generating hardware development not only from industrial view but also from research activities. MRAM, magnetic memory, spintronics devices and many other electronics

applications are now made of multiferroic composite. So this research should be elaborated to understand our possibility in hardware development. The following experiment and activities would be obtained as future work as the extension of this research.

- i. The characteristics in crystallization formation will be achieved by DSC thermal analysis.
- ii. Band gap understanding is a crucial requirement for multiferroic composites measurement because of having different materials which would be taken by UV-vis spectroscopy.
- iii. The bond length and bonding mechanism would be carried out by FTIR spectroscopy.
- iv. To understand the multiferroic properties of prepared sample it is required to understand the ferroelectric properties by P-E loop.
- v. Temperature dependent magnetization and dielectric properties will be carried out to understand the effect of temperature on multiferroic parameters.
- vi. To observe the nano size, TEM analysis is required.

References

Chapter I

- [1.1] Verrma A., Goel T.C., Mendiratta R.G., Gupta R.G.; “High – Resistivity Ni – Zn Ferrites by the citrate Precursor Method”, J. Magn. Magn. Mater., 192, 271-276, 1999.
- [1.2] Nakamura J., Miyamoto T., Yamada Y.; “Complex Permeability Spectra of Polycrystalline Li – Zn Ferrite and Application of EM – Eave Absorber”; J. Magn. Magn. Mater., 256, 340 – 347, 2003.
- [1.3] Laksman A., Rao K.H, Mendiratta R. G.; “Magnetic Properties of In⁵⁺ and Cr³⁺ Substituted Mg – Mn Ferrites”, J. Magn. Magn. Mater., 250, 92 -97, 2002.
- [1.4] Khan Z. H., Sikder S. S., Hakim M. A., Saha D. K. and Noor S.; “Structural and Magnetic Properties of Cu Substitute Ni - Cu – Zn Ferrites”, Journal of Engineering Science, 02, 81 – 85, 2011.
- [1.5] Rezlescu N., Rezlescu L., Popa P. D., Rezlescu L.; “Influence of Additives on the Properties of a Ni – Zn Ferrite with Low Curie Point” J. Magn. Magn. Mater.; 215 – 216, 2000.
- [1.6] Abdeen A. M.; “Electrical Conduction in Ni – Zn Ferrites”, J. Magn. Magn. Mater., 185, 199, 1998.
- [1.7] Khan Z. H., Mahbubur R. M., Sikder S. S, Hakim M. A. and Saha D. K.; “Complex Permeability of Fe Deficient Ni – Zn – Zn Ferrites” J. of Alloys & Com., 548, 208 – 215, 2013.
- [1.8] HSU J. Y., Ko W. S. and Chen C. J.; “The Effect of V₂O₅ on the Sintering of Ni – Cu – Zn Ferrites”, IEEE Trans. Magn., 31, 3994, 1995.
- [1.9] Rahul C. Kambale, Song K. M. Hur N.; “Dielectric and Magnetolectric Properties of BaTiO₃ – CoMn_{0.2}Fe_{0.18}O₄ Particulate (0 – 3) Multiferroic Composites”, Current App. Phy., 13, 582 – 566, 2013.
- [1.10] Wang Y., Xu G., Ren Z., Wei X.,Weng W., Du P., Shen G., Han G.; Low temperature polymer assisted hydrothermal synthesis of bismuth ferrite nanoparticles, Ceram Int. 34, 1569–1571, 2008
- [1.11] W.M. Zhu, Z.G. Ye; Effects of chemical modification on the electrical properties of $0.67\text{BiFeO}_3-0.33\text{PbTiO}_3$ ferroelectric ceramics, Ceram. Int.30, 1435–1442, 2004

- [1.12] S.D. Bader and S.S.P. Parkin; Spintronics, Annual Review of Condensed Matter Physics, 71-88, 2010
- [1.13] G. E. Moore, "Cramming more components onto integrated circuits" Electronics, 38, 1965.
- [1.14] Moore G. E. "Progress in digital integrated electronics" in Electronic Devices Meeting, 1975 International, 21, 11-13,1975
- [1.15] Mathias W., Magnetization control in multiferroic heterostructures, Diploma thesis, Technical University of Munich, Munich, 2007
- [1.16] Ramesh R. & Nicola A. Spaldin, Multiferroics: progress and prospects in thin films, Nature Materials 6, 21 – 29, 2007
- [1.17] Yang C. H., Kan D., Takeuchi I., Nagarajan V. and Seidel J; Doping BiFeO₃: approaches and enhanced functionality, Phys. Chem. Chem. Phys., 14, 15953–15962, 2012,
- [1.18] Colonel Wm., T. McLyman; Transformer and Inductor Design Handbook, Third Edition, Marcel Dekker, Inc, New York, 2004
- [1.19] Kim N. G., Koo Y. S. and Jung J. H.; "Dielectric and Magnetic Properties of BaTiO₃ – CoMn_{0.2}Fe_{1.8}O₄, J. M. M. 2006
- [1.20] Chaudhuri A., Mandal K., Enhancement of ferromagnetic and dielectric properties of lanthanum doped bismuth ferrite nanostructures, Materials Research Bulletin 47, 1057–1061, 2012
- [1.21] Du Y, Cheng Z.X., Shahbazi M., Collings E.W., Dou S.X., Wang X.L.; Enhancement of ferromagnetic and dielectric properties of lanthanum doped bismuth ferrite nanostructures, J. of Alloys and Com., 490, 637–641, 2010
- [1.22] Chu Y. H., Zhan Q., Yang C.-H., Cruz M. P., Martin L. W., Zhao T., Yu P., Ramesh R., Joseph P. T., Lin I. N., Tian W., and Schlom D. G.; Low voltage performance of epitaxial BiFeO₃ films on Si substrates through lanthanum substitution, Applied Physics Letters 92, 102909, 2008
- [1.23] Li S., Lin Y.H., Zhang B.P., Wang Y., Nan C.W., J. Phys. Chem. C 114 (7) 2903-2908, 2010.
- [1.24] Ponzoni C., Rosa R., Cannio M., Buscaglia V., Finocchio E., Nanni P., Leonelli C., J. Eur. Cer. Soc. 33 (7), 1325e1333, 2013

- [1.25] J. Deng, S. Banerjee, S.K. Mohapatra, Y.R. Smith, M. Misra, J. Fundam. Renew. Energy Appl. 1 ,1e1,(2011)
- [1.26] F.G. Garcia, C.S. Riccardi, A.Z. Simoes, J. Alloys Compd. 501, 25 ~ e29, 2010
- [1.27] S.T. Zhang, Y. Zhang, M.H. Lu, C.L. Du, Y.F. Chen, Z.-G. Liu, Y.Y. Zhu, N.B. Ming, X.Q. Pan, Appl. Phys. Lett. 88, 2006.
- [1.28] G.L. Yuan, O.S. Wing, J. Appl. Phys. 100, 2006
- [1.29] S.K. Singh, H. Ishiwara, Jpn. J. Appl. Phys. 45, 2006
- [1.30] Ponzoni, C., Cannio, M., Boccaccini, D., Bahl, C. R. H., Agersted, K., & Leonelli, C. (2015). Ultrafast microwave hydrothermal synthesis and characterization of $\text{Bi}_{1-x}\text{La}_x\text{FeO}_3$ micronized particles. *Mat. Chem. and Phy.*, 162, 69-75, 2015.
- [1.31] Sen K., Singh K., Gautam A., Singh M., Dispersion studies of La substitution on dielectric and ferroelectric properties of multiferroic BiFeO_3 ceramic, *Cer. Intern.* 38, 243–249, 2012
- [1.32] Chen Z., Li Y., Wu Y., Hydrothermal synthesis and mechanism and property study of La-doped BiFeO_3 crystallites, *J Mater Sci: Mater Electron* 23, 2012
- [1.33] Chu Y.-H. et al., *Nano Lett.* 9, 1726, 2009.
- [1.34] Streiffer S. K. et al., *J. Appl. Phys.* 83, 2742, 1998.
- [1.35] Rao B. P., Rao K. H., Sankaranarayana G., Paduraru A., Caltun O. F., Influence Of V_2O_5 Additions On The Resistivity And Dielectric Properties Of Nickel-Zinc Ferrites
- [1.36] B. Dhanalakshmi, et al., Impedance spectroscopy and dielectric properties of multiferroic $\text{BiFeO}_3/\text{Bi}_{0.95}\text{Mn}_{0.05}\text{FeO}_3\text{-Ni}_{0.5}\text{Zn}_{0.5}\text{Fe}_2\text{O}_4$ composites, *Cer. Inter.*, 2015
- [1.37] B. Dhanalakshmi et al. *J. of M. and M. M.* 404 119–125, 2016
- [1.38] L. Bin, W. Chunqing and D. Guangbin, Synthesis of multiferroic $\text{Bi}_{0.9}\text{La}_{0.1}\text{Fe}_{0.95}\text{Mn}_{0.05}\text{O}_3\text{-Ba}_{0.7}\text{Sr}_{0.3}\text{TiO}_3\text{-Ni}_{0.8}\text{Zn}_{0.2}\text{Fe}_2\text{O}_4$ nanotubes with one closed end using a template-assisted sol–gel process

Chapter 2

- [2.1] Kumarasiri, D. Akila, "Effects of transition metal doping on multiferroic ordering in $\text{Ni}_3\text{V}_2\text{O}_8$ and FeVO_4 ", Wayne State, University Dissertations. Paper 572, 2012.

- [2.2] Auciello O., Scott J. F., and Ramesh R., *Phy. Today*, 51, 22–27, 1998.
- [2.3] Busch-Vishniac I. J., *Physics Today*, 51, 28, 1998.
- [2.4] Hill N. A., “Why are there so few magnetic ferroelectrics?” *Journal of Physical Chemistry B*, Vol. 104, 2000.
- [2.5] Prellier W., Singh M. P., Murugavel P., *J. Phys.-Condens. Mat.* 2005.
- [2.6] Cheong S. W., Mostovoy M., *Nat. Mater.* 6, 13, 2007.
- [2.7] Khomskii D., *Physics*, 2, 20, 2009
- [2.8] Wang K. F., Liu J. M., Ren Z. F., *Adv. Phys.* 58, 321, 2009.
- [2.9] Tokura Y., Seki S., *Adv. Mater.* 22, 1554, 2010.
- [2.10] Nan C. W., Bichurin M. I., Dong S. X., Viehland D., Srinivasan G., *J. Appl. Phys.* 103, 03 1101, 2008.
- [2.11] Srinivasan G., *Annu. Rev. Mater. Res.* 40, 153, 2010
- [2.12] Wang J et al, *Science* 299, 2003.
- [2.13] N A Hill, *J. Phys. Chem. B* 104 6694, 2000
- [2.14] Ravindran P., Vidya R., Kjekshus A., Fjellvåg H .and Eriksson O. *Phys. Rev. B* 74 224412, 2006.
- [2.15] Teague J R, Gerson R and James W J, *Solid State Commun.* 1970.
- [2.16] Kubel F and Schmid H, *Acta Crystallogr. B* 46, 1990.
- [2.17] Zhang X Y, Lai C W, Zhao X, Wang D Y and Dai J Y, *Appl. Phys. Lett.* 87, 2005
- [2.18] Wu J and Wang J, *J. Appl. Phys.* 106, 2009
- [2.19] Wang Y, *J. Appl. Phys.* 109, 2011
- [2.20] Hill N. A., *J. Phys. Chem. B*, 104, 2000.
- [2.21] Wang J., Neaton J. B., Zheng H., Nagarajan V., Ogale S. B., Liu B., Viehland D., Vaithyanathan V., Schlom D. G., Waghmare U. V., Spaldin N. A., Rabe K. M., Wuttig M., Ramesh R., *Science*, 299, 2003.
- [2.22] Lottermoser T., Lonkai T., Amann U., Hohlwein D., Ihringer J., M. Fiebig , *Nature*, 430, 541, 2004.
- [2.23] Catalan G., Scott J. F., *Adv. Mater.* 21, 2009.
- [2.24] Eerenstein W., Mathur N. D., Scott J. F., *Nature*, 442, 759, 2006.
- [2.25] Van J., *Philips Res. Rep.*, 27, 28, 1972.
- [2.26] Nan C. W., *Phys. Rev. B*, 50, 6082, 1994.

- [2.27] Nan C. W., Li M., Huang J. H., Phys. Rev. B, 63, 2001.
- [2.28] Ryu J. H., Priya S., Carazo A. V., Uchino K., Kim H. E., J. Am. Ceram. Soc., 84, 2001.
- [2.29] Dong S. X., Cheng J. R., Li J. F., Viehland D., Appl. Phys. Lett. 83, 2003.
- [2.30] Jiang Q. H., Shen Z. J., Zhou J. P., Shi Z., Nan C. W., J. Eur. Ceram. Soc., 27, 279, 2007.
- [2.31] Agrawal S., Cheng J. P., Guo R. Y., Bhalla A. S., Islam R. A., Priya S., Mater. Lett. 63, 2009.
- [2.32] Martin C.R., Nanomaterials: a membrane-based synthetic approach, Science 266, 1994.
- [2.33] Teague J. R., Gerson R. and James W.J., Sol. Stat. Commun. 8 1073, 1970.
- [2.34] Fischer P. and Polomska M., J. Phys. C: Sol. Stat. Vol. 13, 1931, 1980.
- [2.35] J. Wang et al., Science 299, 1719, 2003.
- [2.36] Park T.-J., Papaefthymiou G. C., Viescas A. J., Moodenbaugh A. R., Wong S. S., Nano Lett. 7, 766, 2006.
- [2.37] Gao F., Yuan Y., Wang K. F., Chen X. Y., Chen F., Liu J.-M., Ren Z. F., Appl.Phys. Lett. 89, 2006.
- [2.38] Mazumder R., Ghosh S., Mondal P., Bhattacharya D., Dasgupta S., Das N., Sen A., Tyagi A. K., Sivakumar M., Takami T., Ikuta H., J. Appl. Phys. 2006.
- [2.39] Richardson J. T., Milligan W. O., Phys. Rev. 102, 1956.
- [2.40] Levy M. R., Crystal Structure and Defect Property Predictions in Ceramic Materials, University of London, 2005
- [2.41] Burfoot J. C., Ferroelectrics - An Introduction to the Physical Principles, 1st ed. D. Van Nostrand Company LTD., London, 1967.
- [2.42] Smolenskii G., Isupov V., Agranovskaya A., and Krainik N., Sov. Phys. Solid State 2, 2651, 1961.
- [2.43] Kiselev S. V., Ozerov R. P., and Zhdanov G. S., Nauk D.A., SSSR, Sov. Phys. Dokl. 7, 742, 1962.
- [2.44] Speranskaya E. J., Skorikov V. M., Kode E. Y., Terektova V. A., Bull. Acad.Sci. U. S. S. R. 5, 873, 1965.

- [2.45] Morozov M. I., Lomanova N. A., Gusarov V. V., Russ. J. Gen. Chem. 2003,73, 1680.
- [2.46] Palai R., Katiyar R. S., Schmid H., Tissot P., Clark S. J., Robertson J., Redfern S. A. T., Catalan G., Scott J. F., Phys. Rev. B, 77, 2008.
- [2.47] Valant M., Axelsson A.-K., Alford N., Chem. Mater. 2007, 19, 5431.
- [2.48] Krainik N. N., Khuchua N. P., Zhdanova V. V., Evseev V. A., Sov. Phys. Solid State, 8, 654, 1966.
- [2.49] Schmid H.: private communication, 2006.
- [2.50] Lebeugle D., Ph.D. Thesis, Saclay Institute of Matter and Radiation, 2007.
- [2.51] Bea H., Bibes M., Barthe A., Bouzehouane K., Jacquet E., Khodan A., Contour J.-P., Appl. Phys. Lett. 87, 2005.
- [2.52] Lou X. J., Yang C. X., Tang T. A., Lin Y. Y., Zhang M., Scott J. F., Appl. Phys. Lett. 90, 2007.
- [2.53] Landau L. D. and Lifshitz E. M., Statistical Physics, Vol. 5 of Course of theoretical physics, 2nd ed. (Pergamon Press, London, 1959).
- [2.54] Landau L. D. and Lifshitz E. M., Statistical Physics, Vol. 5 of Course of theoretical physics, 2nd ed., Pergamon Press, London, 1959.
- [2.55] R. C. Smith, M. J. Dapino, and S. Seelecke, Journal of Applied Physics 93, 458, 2003.
- [2.56] Smith R. C., Seelecke S., Ounaies Z., and Smith J., Journal of Intelligent Material Systems and Structures 14, 719, 2003.
- [2.57] Massad J. E., Smith R. C., and Carman G. P., in Smart Structures and Materials: Modeling, Signal Processing and Control, edited by R. C. Smith, SPIE, San Diego, No. 1, pp. 13-23. 2003.
- [2.58] Khomskii D., Physics 2, 20, 2009.
- [2.59] Lines M.E. and Glass A.M., Principles and Applications of Ferroelectrics and Related Materials, Oxford University Press, 1977.
- [2.60] Hippel, A.V. and R.G. Breckenridge, High dielectric constant ceramics. Ind. Eng. Chem. 38(11): p. 1097-1109, 1946.
- [2.61] Sawaguchi, E., Ferroelectricity versus Antiferroelectricity in the Solid Solutions of PbZrO_3 and PbTiO_3 . J. Phys. Soc. Jpn., 8: p. 615-629, 1953.

- [2.62] Shirane, G. and A. Takeda, Phase Transitions in Solid Solutions of PbZrO_3 and PbTiO_3 (I) Small Concentrations of PbTiO_3 . *J. Phys. Soc. Jpn.*, 7: p. 5-11, 1952.
- [2.63] Nassau, K., Levinstein H.J., and Loiacono G.M., Ferroelectric Lithium Niobate. 1. Growth, Domain Structure, Dislocations and Etching. *J. Phys. Chem. Solids*, 27: p. 983-988, 1966.
- [2.64] Nassau, K., Levinstein H.J., and Loiacono G.M., Ferroelectric Lithium Niobate. 2. Preparation of Single Domain Crystals. *J. Phys. Chem. Solids*, 27: p. 989-996, 1966.
- [2.65] Abrahams, S.C., Reddy J.M., and Bernstein J.L., Ferroelectric Lithium Niobate. 3. Single Crystal X-ray Diffraction Study at 24°C . *J. Phys. Chem. Solids*, 27: p. 997-1012, 1966.
- [2.66] Abrahams, S.C., Hamilton W.C., and Reddy J.M., Ferroelectric Lithium Niobate. 4. Single Crystal Neutron Diffraction Study at 24°C . *J. Phys. Chem. Solids*, 27: p. 1013-1018. 46, 1966.
- [2.67] Abrahams, S.C., Levinstein H.J., and J.M. Reddy, Ferroelectric Lithium Niobate. 5. Polycrystal X-ray Diffraction Study between 24°C and 1200°C . *J. Phys. Chem. Solids*, 1966.
- [2.68] Wudl, F. and Thompson J.D., Buckminsterfullerene C_{60} and Organic Ferromagnetism *J. Phys. Chem. Solids*, 53(11): p. 1449-1455, 1992.
- [2.69] Adams, D.M. *Inorganic Solids*, John Willey, London, pp. 68, 1974.
- [2.70] Sanpo, Noppakun, *Solution Precursor Plasma Spray System*, ISBN-9783319070247
- [2.71] Sickafus, K.E.; Wills, J. J. *Am. Ceram. Soc.*, 82, 3279-3281., 1999.
Alex Goldman, *Modern Ferrite Technology*, Van Nostrand Reinhold, New York,
- [2.72] p-71, 1990.
- [2.73] Craik, D.J. *Magnetic Oxide, Part 1*, John Wiley & Sons, Bristol, ch. 9, part-2, 1975.
- [2.74] Verway, E.J.W.; Heilmann, E.L. *J. Chem. Phys.* 15, 174-180, 1947.
- [2.75] Romeign, F.C. *Philips Res. Rep.* 8, 304-342, 1953.
- [2.76] Chikazumi, S., *Physics of ferromagnetism*. 2nd Edition ed., Oxford: Oxford University Press, 2009.

- [2.77] Wudl, F. and Thompson J.D., Buckminsterfullerene C₆₀ and Organic Ferromagnetism *J. Phys. Chem. Solids*, 53(11): p. 1449-1455, 1992.
- [2.78] William D. Callister, The University of Utah; *Materials Science and Engineering* 6th ed., Wiley 2003.
- [2.79] Loidl, A., Loehneysen H.V., and Kalvius G.M., Multiferroics. *Journal of Physics: Condensed Matter*, 20(43): p. 430301, 2008.
- [2.80] Martin, L.W. and Ramesh R., Multiferroic and magnetoelectric heterostructures. *Acta Materialia*, 60(6-7): p. 2449-2470, 2012.
- [2.81] Scott, J.K., Multiferroic memories. *Nature materials*, 6: p. 256-257, 2007.
- [2.82] Spaldin N. A. and Fiebig M., *Science* 309, 391, 2005.
- [2.83] Kimura T., Goto T., Shintani H., Ishizaka K., Arima T., And Tokura Y., *Nature* 426, 55, 2003.
- [2.84] Hur N., Park S., Sharma P. A., Ahn J. S. Guha., S., And Cheong S.-W., *Nature* 429, 392, 2004.

Chapter 3

- [3.1] Dong, Y. and Feng, S.S., Methoxy poly (ethylene glycol)-poly (lactide) (MPEG-PLA) nanoparticles for controlled delivery of anticancer drugs. *Biomaterials*, 25(14), pp.2843-2849, 2004.
- [3.2] Rakesh, L., et al. "Computer-aided applications of nanoscale smart materials for biomedical applications." - *Future Medicine*: 719-739, 2008.
- [3.3] Larson, Daniel R., et al. "Water-soluble quantum dots for multiphoton fluorescence imaging in vivo." *Science* 300.5624: 1434-1436, 2003.
- [3.4] Lee, S., Choi, S. S., Li, S. A., & Eastman, J. A. Measuring thermal conductivity of fluids containing oxide nanoparticles. *Journal of Heat transfer*, 121(2), 280-289, 1999.
- [3.5] Dietz, R. Ellen and B. Raula, *Safety standards and infection control for dental hygienists*. Albany, NY: Delmar Thomson Learning. p. 129, 2002.
- [3.6] Garrett, Reginald H.; Grisham, Charles M. *Biochemistry* (5th ed.). Belmont, CA: Brooks/Cole, Cengage Learning. p. 111. 2013.

- [3.7] http://www.ehow.com/how_5018706_convert-centrifuge-rpm-rcf-_g_force_.html
- [3.8] Ballou, David P.; Benore, Marilee; Ninfa, Alexander J.. Fundamental laboratory approaches for biochemistry and biotechnology. (2nd ed.). Hoboken, N.J.: Wiley. p. 43. 2008.
- [3.9] Yue Z., Zhou J., Li L., Wang X., Gui Z., Materials Science and Engineering: B, – Elsevier, 2001.
- [3.10] Joong S., Sintering: Densification, Grain Growth and Microstructure
- [3.11] Rahaman M. N., Ceramic Processing and Sintering,
- [3.12] Liao J.Y., Lei B.X., Chen H.Y., Kuang D.B., Energy & Environmental , pubs.rsc.org, 2012.
- [3.13] Cullity B. D., Elements of x-ray diffraction
- [3.14] Richard J. D. Tilley , Understanding Solids: The Science of Materials
- [3.15] Kittel C., Introduction to Solid State Physics, 7th edition, John Wiley and sons, Inc., Singapore, 1996.
- [3.17] V. B. Kawade, G. K. Bichile, KM Jadhav - Materials Letters, - Elsevier, 2000.
- [3.18] Nam J. H., Hur W. G., Oh J. H., Journal of applied physics, 1997.
- [3.19] Igarashi H., Okazaki K, Journal of the American Ceramic, - Wiley Online Library, 1977
- [3.20] Burton A. W., Ong K, Rea T, Chan I. Y., Microporous and Mesoporous, - Elsevier, 2009.
- [3.21] Kumar L., Kar M., Effect of La³⁺ substitution on the structural and magnetocrystalline anisotropy of nanocrystalline cobalt ferrite (CoFe_{2-x}La_xO₄), Ceramics International 38, 4771–4782, 2012.
- [3.22] Ghatak S., Sinha M., Meikap A.K., Pradhan S.K., Anomalous electrical transport properties of nonstoichiometric nickel ferrite below room temperature, Materials Research Bulletin 46, 1055–1064, 2011.
- [3.23] Iqbal, M.J.; Ashiq, M.N.; Gomez, P.H. J. Magn. Mater., 320, 881-886, 2008.
- [3.24] Kojima, H. Ferromagnetic Materials: A Handbook on the Properties of Magnetically Ordered Substances, North-Holland, Amsterdam, pp. 318, 1982.
- [3.25] Iqbal, M.J.; Farooq, S. Mater. Res. Bull., 44, 2050-2055, 2009.

- [3.26] Iqbal, M.J.; Ahmad, Z.; Meydan, T.; Nlebedim, I.C. *Mater. Res. Bull.*, 47, 344-351, 2012.
- [3.27] Kao, K.C. *Dielectric Phenomena in Solids*, Elsevier Academic Press, California, pp. 51, 2004.
- [3.28] Hana Naceur, Adel Megriche and Mohamed El Maaoui, *NACEUR et al., Orient. J. Chem.*, Vol. 29(3), 937-944, 2013.
- [3.29] Smyth C.P.: *Acta Cryst.* 9:838, 1956.
- [3.30] Afandiyeva I.M., Dökme I., Altındal, Bülbül M.M., Tatarolu and A.,: *Microelectron. Eng.* 85: 247, 2008.
- [3.31] Velenzuela R., *Magnetic Ceramics*, Cambridge University Press, Cambridge (1994)
- [3.32] Hadfield D., *permanent Magnets and Magnetism*, Jhon Wiley and Sons , Inc ;New York, 1962.
- [3.33] Cullity B.D., *Introduction to Magnetic Materials*, Addison-Wiseley Publishing Company, Inc, California, 1972.
- [3.34] Chikazumi S., *Physics of Magnetism*,Jhon Wiley & Sons, Inc, NewYork, 1966.

Chapter 4

- [4.1] Rodriguez J., Carvajal Laboratory, FULLPROF, a Rietveld and Pattern Matching and Analysis Programs Version Laboratoire Leon Brillouin, CEA-CNRS, France, 2010.
- [4.2] G.S. Lotey, N.K. Verma, Phase-dependent multiferroism in Dy-doped BiFeO₃ nanowires Superlattices and Microstructures 53, 184–194, 2013.
- [4.3] Cheng Z X, Li A H, Wang X L, Dou S X, Ozawa K, Kimura H, Zhang S J and ShROUT T R, *J. Appl. Phys.* 103, 2008.
- [4.4] Bras G Le, Colson D, Forget A, Genand-Riondet N, Tourbot R and Bonville P, *Phys. Rev. B* 80, 2009.
- [4.5] Ianculescu A, Prihor F, Postolache P, Mitoseriu L, Dragan N and Crisan D, *Ferroelectrics* 391, 67–75, 2009

- [4.6] T.T. Carvalho, Room temperature structure and multiferroic properties in $\text{Bi}_{0.7}\text{La}_{0.3}\text{FeO}_3$ ceramics, *Journal of Alloys and Compounds* 554, 97–103, 2013.
- [4.7] Pradhan S K and Roul B K, *J. Phys. Chem. Solids* 72 1180–7, 2011.
- [4.8] V. R. Singh, A. Garg, D. C. Agrawal, Structural changes in chemical solution deposited lanthanum doped bismuth ferrite thin films, *Applied Physics Letters* 92, 2008.
- [4.9] Lawrence Kumar, Manoranjan Kar, Effect of La^{3+} substitution on the structural and magnetocrystalline anisotropy of nanocrystalline cobalt ferrite ($\text{CoFe}_{2-x}\text{La}_x\text{O}_4$), *Ceramics International* 38, 4771–4782, 2012.
- [4.10] Kavita Verma, Ashwini Kumar, Dinesh Varshney, Dielectric relaxation behavior of $\text{A}_x\text{Co}_{1-x}\text{Fe}_2\text{O}_4$ ($\text{A}=\text{Zn}, \text{Mg}$) mixed ferrites, *Journal of Alloys and Compounds* 526, 91–97, 2012.
- [4.11] R. Mukherjee, T. Sahu, S. Sen, P. Sahu, Structural and microstructural evolution due to increasing Co substitution in $\text{Ni}_{1-x}\text{Co}_x\text{Fe}_2\text{O}_4$: an X-ray diffraction study using the Rietveld method, *Materials Chemistry and Physics* 128, 365–370, 2011.
- [4.12] P. Pahuja, Synthesis and characterization of $\text{Ni}_{0.8}\text{Co}_{0.2}\text{Fe}_2\text{O}_4\text{--Ba}_{0.95}\text{Sr}_{0.05}\text{TiO}_3$ multiferroic composites, *Ceramics International* 39, 9435–9445, 2013.
- [4.13] T.T. Carvalho, P.B. Tavares, *Mater. Lett.* 62, 3984, 2008.
- [4.14] Bai Y, Xu F, Qiao L, Zhou J, Li L, The static and hyperfrequency magnetic properties of a ferromagnetic–ferroelectric composite. *J Magn Magn Mater* 321:148–151, 2009.
- [4.15] N. Adhlakha K. L. Yadav, Structural, dielectric, magnetic, and optical properties of $\text{Ni}_{0.75}\text{Zn}_{0.25}\text{Fe}_2\text{O}_4\text{--BiFeO}_3$ composites, *J Mater Sci.*, 49:4423–4438, 2014.
- [4.16] P. Pahuja, R. Sharma, C. Prakash, R.P. Tandon, Synthesis and characterization of $\text{Ni}_{0.8}\text{Co}_{0.2}\text{Fe}_2\text{O}_4\text{--Ba}_{0.95}\text{Sr}_{0.05}\text{TiO}_3$ multiferroic composites, *Ceramics International* 39, 9435–9445, 2013.
- [4.17] T.K. Gupta, R.L. Coble, *J. Am. Ceram. Soc.* 51, 521-525, 1968.
- [4.18] O.F. Calton, L. Spinu, Al. Stancu, L.D Thung, W. Zhou, Study of the microstructure & permeability spectra of Ni-Cu-Zn ferrites, *J. Magn. Magn. Matter.* 160, 242-245, 2002.
- [4.19] Suresh, P.; Babu, P. D.; Srinath, S. *J. Appl. Phys.*, 115, 2014.

- [4.20] B. Ruetter, et al., Phys. Rev. B 69, 2004.
- [4.21] C. Ederer and N. A. Spaldin, Phys. Rev. B 71, 2005.
- [4.22] Palkar VR, Kundaliya DC, Malik SK. J. Appl. Phys. 93, 4337, 2003.
- [4.23] Palkar VR, Pinto R. Pramana, J. Phys. 58, 1003, 2002.
- [4.24] M. Kaur, K. L. Yadav, P. Uniyal, Investigations on multiferroic, optical and photocatalytic properties of lanthanum doped bismuth ferrite nanoparticles, Adv. Mater. Lett., 6(10), 895-901, 2015.
- [4.25] V.S. Pokatilov, V.V. Pokatilov, A.S. Sigov, Phys. Solid State 51, 552, 2009.
- [4.26] Z. Zhang, H. Liu, Y. Lin, Y. Wei, C. W. Nan, and X. Deng, Influence of La Doping on Magnetic and Optical Properties of Bismuth Ferrite Nanofibers, Hindawi Publishing Corporation, Journal of Nanomaterials, p. 5, 2012.
- [4.27] Meiklejohn, W. & Bean, C. New magnetic anisotropy. *Phys. Rev.* 105, 904–913, 1957.
- [4.28] Vopsaroiu, M., Blackburn, J. & Cain, M. G. A new magnetic recording read head technology based on the magneto-electric effect. *J. Phys. D* 40, 5027–5033, 2007.
- [4.29] Greve, H., Woltermann, E., Quenzer, H-J., Wagner, B. & Quandt, E. Giant magnetoelectric coefficients in (Fe₉₀Co₁₀)₇₈Si₁₂B₁₀-AlN thin film composites. *Appl. Phys. Lett.* 96, 182501, 2010.
- [4.30] Coey, JMD: Rare Earth Permanent Magnetism, 1st edn. Wiley, New York, 1996
- [4.31] O. Mirzaee, M.A. Golozar, A. Shafyei, Influence of V₂O₅ as an effective dopant on the microstructure development and magnetic properties of Ni_{0.64}Zn_{0.36}Fe₂O₄ soft ferrites, Materials Characterization 59, 638–641, 2008.
- [4.32] Li, Y., Cao, M-S., Wang, D-W, High-efficiency and dynamic stable electromagnetic wave attenuation for La doped bismuth ferrite at elevated temperature and gigahertz frequency. RSC Advances, 5 (94), 2015.
- [4.33] J. Q. Huang, P. Y. Du, L. X. Hong, Y. L. Dong, and M. C. Hong, Adv. Mater. Weinheim, Ger. **19**, 437, 2007.
- [4.34] M. A. Laughton, D. F. Warne, Electrical Engineer's Reference Book, Newnes, Elsevier Science, 2003.
- [4.35] J. L. Snoek, Physica Amsterdam 14, 207 1948.
- [4.36] H. Zhang, S. Wing Or and H. L. Wa Chan, Multiferroic properties of Ni_{0.5}Zn_{0.5}Fe₂O₄ – Pb(Zr_{0.53}Ti_{0.47})O₃ cer. Com., J. of App. Phy. 104, 104109, 2008.

- [4.37] S.R. Das, R.N. Choudhary, P. Bhattacharya, R.S. Katiyar, P. Dutta, A. Manivannan, M.S. Sheehra, *J. Appl. Phys.* 101, 2007.
- [4.38] P. Maksymovych, J. Seidel, Y. H. Chu, P. P. Wu, A. P. Baddorf, L. Q. Chen, S. V. Kalinin, and R. Ramesh, *Nano Lett.* 11(5), 1906, 2011.
- [4.39] Y. P. Wang, L. Zhou, M. F. Zhang, X. Y. Chen, J. M. Liu, and Z. G. Liu, “Room-Temperature Saturated Ferroelectric Polarization in BiFeO₃ Ceramics Synthesized by Rapid Liquid Phase Sintering,” *Appl. Phys. Lett.*, 84 [10] 1731–3, 2004.
- [4.40] Q. Hui Jiang and C. W. Nan, Synthesis and Properties of Multiferroic La-Modified BiFeO₃ Ceramics, *J. Am. Ceram. Soc.*, 89 [7] 2123–2127, 2006.
- [4.41] L.I. Rabinkin, Z.I. Novikova, *Ferrites*, Minsk 146, 1960.
- [4.42] A. Chaudhuri, K. Mandal, Enhancement of ferromagnetic and dielectric properties of lanthanum doped bismuth ferrite nanostructures, *Materials Research Bulletin* 47, 1057–1061, 2012.
- [4.43] K. Iwauchi, *Jpn. J. Appl. Phys.* 10, 1520, 1971.
- [4.44] L. I. Rabinkin, Z. I. Novikova, in “*Ferrites*” Minsk, p.146, 1960.
- [4.45] G. C. Jain, B. K. Das, R. B. Tripathi, R. Narayan, *IEEE Trans. Magn.* 18, 776, 1982.
- [4.46] B. Parvatheeswara Rao, K. H. Rao, G. Sankaranarayana, A. Paduraru, O. F. Caltun, Influence Of V₂O₅ Additions On The Resistivity And Dielectric Properties Of Nickel-Zinc Ferrites, *Journal of Optoelectronics and Advanced Materials* Vol. 7, No. 2, p. 697 – 700, 2005.
- [4.47] C. G. Koops, *Phys. Rev* 83, 121, 1951.
- [4.48] J. C. Maxwell, *A Treatise on Electricity and Magnetism*, Clarendon Press, Oxford p. 328. 1982.
- [4.49] K. W. Wagner, *Ann. Physik* 40, 817, 1913.
- [4.50] A.K. Pradhan, K. Zhang, D. Hunter, J.B. Dasdon, G.B. Loutts, *J. Appl. Phys.* 97, 2005.
- [4.51] B. Dhanalakshmi, K. Pratap, B. Parvatheeswara Rao, P.S.V. Subba Rao, Diffuse Dielectric Anomalies in (x).Bi_{0.95}Mn_{0.05}FeO₃–(1-x).Ni_{0.5}Zn_{0.5}Fe₂O₄ multiferroic composites, *Journal of Magnetism and Magnetic Materials* 404, 119–125, 2016.